



# DISSERTATION

## Thema

### Determination of the Hydrogen Ground-State Hyperfine Splitting in a Beam and Perspectives for Antihydrogen

Ausgeführt zum Zwecke der Erlangung des akademischen Grades eines  
Doktors der technischen Wissenschaften, unter der Leitung von

Hon.-Prof. Dipl.-Phys. Dr. Eberhard Widmann  
am Stefan-Meyer-Institut für subatomare Physik,  
der Österreichischen Akademie der Wissenschaften

Eingereicht an der Technischen Universität Wien,  
Fakultät für Physik

von

Mag. rer. nat. Martin Diermaier  
Matrikelnummer 0405327  
Leystraße 165/3/20, 1020 Wien

---

Ort, Datum

---

Unterschrift (M. Diermaier)



# Kurzfassung

Der Vergleich von Teilchen und Antiteilchen Systemen um die  $\mathcal{CPT}$  Symmetrie zu testen ist heutzutage von intrinsischer Interesse für die Teilchenphysik. Ein interessantes System ist der Vergleich der Grundzustands-Hyperfeinstruktur von Wasserstoff mit Antiwasserstoff bei der Abwesenheit eines Magnetfeldes. Die ASACUSA Kollaboration strebt danach diesen  $\mathcal{CPT}$  Test mit einem Rabi Spektrometer Aufbau durchzuführen.

Diese Arbeit beschreibt den Spektrometer Aufbau, welche bei den Antiwasserstoff Experimenten verwendet werden wird. Die einzelnen Komponenten wurden getestet und der gesamte Aufbau wurde mit atomaren Wasserstoff charakterisiert.

Die wichtigsten Teile dieses Experiments waren eine atomare Wasserstoffquelle, ein kryogenisches Arrangement um den Strahl zu kühlen, ein Strahl-Modulator, zwei polarisierende Sextupolmagnete, eine Mikrowellenkavität, welche die Spinzustände invertiert, einen supraleitenden Sextupolmagneten als Analysemagnet und ein Massenspektrometer.

Ein zweiter sehr wichtiger Teil dieser Arbeit bestand darin die  $\sigma_1$ -Übergänge, welche eine der für diese Kavität möglichen messbaren Übergänge sind, zu analysieren. Wie gezeigt werden wird war es uns möglich mit dieser Strahllinie den besten Wert für die Hyperfeinaufspaltung von atomaren Wasserstoff in einem Rabi-Experiment zu messen. Der gewonnene Wert für eine Frequenz  $\nu_0$  ist  $1\,420\,405\,748.9 \pm 3.3^{\text{stat}} \pm 2.5^{\text{sys}}$  Hz. Die Frequenz ist in Übereinstimmung mit dem Wert von Masermessungen und ist mehr als eine Größenordnung besser als vorhergehende Rabi-Experimente aus den 1950ern. Dieses Resultat zeigt, dass mit Antiwasserstoff eine ähnliche Genauigkeit erreicht werden kann, vorausgesetzt, dass ein Strahl mit vergleichbaren Eigenschaften bereit steht.

# Abstract

Today comparisons of matter and antimatter systems to perform  $\mathcal{CPT}$  tests are of intrinsic interest to the particle physics community. One interesting system is the comparison of the ground state hyperfine structure of hydrogen and antihydrogen at zero magnetic field. The ASACUSA collaboration aims to perform this  $\mathcal{CPT}$  test with a Rabi-type spectrometer beam line.

This work describes the spectrometer beam line which will be used for the antihydrogen experiments. The individual components were tested and the whole setup was characterised with atomic hydrogen. The most important sections in these experiments were an atomic hydrogen source, a cryogenic arrangement for beam cooling, a beam modulating chopper system, two polarising sextupole magnets to select a quantum state doublet, a microwave cavity to drive spin flips, a superconducting sextupole magnet as analysing magnet and a mass spectrometer as detector.

A second essential part in this work was the analysis of the  $\sigma_1$ -transitions, one of the possible transitions that can be measured with our spin flip cavity. As will be shown we were able to measure and evaluate the best value ever for the hyperfine structure of atomic hydrogen in a Rabi like experiment with this beam line. The obtained quantity has a frequency of  $\nu_0 = 1\,420\,405\,748.9 \pm 3.3^{\text{stat}} \pm 2.5^{\text{sys}} \text{ Hz}$ . This value is in agreement with the value of maser measurements and is more than one order of magnitude better than previous Rabi experiments performed in the 1950s. This result shows that similar accuracies could be achieved with antihydrogen provided a beam with similar properties becomes available.

# **Danksagung**

Ich würde gerne folgenden Menschen für die Unterstützung während meiner Dissertation danken:

Meinen Eltern, Kathrin, Martin Simon, Chloé Malbrunot, Clemens Sauerzopf, Bernadette Kolbinger, Oswald Massiczek, Eberhard Widmann, Johann Zmeskal, Johann Marton, Paul Bühler



# Contents

<b>1</b>	<b>Introduction</b>	<b>1</b>
1.1	Motivation . . . . .	1
1.2	Theory . . . . .	2
1.2.1	$\mathcal{CPT}$ Symmetry . . . . .	2
1.2.2	Standard Model Extension . . . . .	6
1.2.3	Hyperfine structure . . . . .	6
1.3	Experimental principle . . . . .	10
1.3.1	Rabi experiment . . . . .	10
1.3.2	Antihydrogen experimental setup overview . . . . .	11
1.3.3	Hydrogen setup overview . . . . .	13
<b>2</b>	<b>Hydrogen beam development and characterisation</b>	<b>16</b>
2.1	Hydrogen source . . . . .	18
2.2	Mass spectrometer . . . . .	19
2.3	QMS tuning . . . . .	21
2.3.1	Emission current . . . . .	23
2.3.2	Electron energy . . . . .	23
2.3.3	Extraction . . . . .	23
2.3.4	Ion energy . . . . .	23
2.3.5	Pole bias . . . . .	25
2.3.6	$m/q$ scan . . . . .	25
2.3.7	SCEM saturation effect . . . . .	27
2.4	Background suppression . . . . .	27
2.4.1	Chopper . . . . .	27
2.5	Beam cooling . . . . .	28
2.6	Time of flight . . . . .	30
2.7	Polarisation . . . . .	31
2.8	Modified fitting function . . . . .	32

<b>3 Hyperfine spectrometer apparatus</b>	<b>35</b>
3.1 Cavity	35
3.1.1 Description of the cavity and the RF system	38
3.1.2 Magnetic shielding	41
3.1.3 Static magnetic field	41
3.2 Superconducting sextupole magnet	43
<b>4 Analysis of the resonance spectra</b>	<b>51</b>
4.1 Fitting function	51
4.2 Total count rate vs. lock-in amplifier signal	53
4.3 Power scan and $\pi$ -pulse	55
4.4 Power vs. frequency maps	56
4.5 Polarisation	60
<b>5 Results and discussion</b>	<b>65</b>
5.1 General considerations	65
5.2 $\nu_0$ determination by usage of $\sigma_1$ and $\pi_1$ transitions in the earth's magnetic field	66
5.3 Extrapolation to zero magnetic field with $\sigma_1$ transitions	68
5.3.1 Settings of the $\sigma_1$ measurement sets	69
5.3.2 DAQ procedure	72
5.3.3 Flowchart of the analysis	74
5.3.4 Power and $B_{\text{osc}}$ (flowchart step 2)	74
5.3.5 Velocity and Velocity spread (step 4)	79
5.3.6 Drift correction and count rate memory shift (step 6)	80
5.3.7 Comparison and checks (step C)	87
5.3.8 Extended fitting function for larger beam diameter	88
5.3.9 Extrapolation to zero magnetic field (step 8)	93
5.4 Evaluation of potential systematic errors (step 9)	96
5.4.1 Current stability	96
5.4.2 Transition fitting function parameters	97
5.4.3 Grouping of parameters	108
5.5 Combined zero field hyperfine splitting (step 10)	113

<b>6 Summary &amp; outlook</b>	<b>117</b>
6.1 Summary . . . . .	117
6.2 Outlook . . . . .	118

<b>Appendices</b>	<b>i</b>
-------------------	----------

<b>Bibliography</b>	<b>xxvii</b>
---------------------	--------------



# 1 Introduction

## 1.1 Motivation

One of the most important fundamentals in particle physics is the discrete  $\mathcal{CPT}$  symmetry [1]. This symmetry states that for particles and antiparticles their properties are exactly the same (such as e.g. lifetime, mass) or exactly opposite (e.g. charge or magnetic moment).

According to the Standard Model of particle physics the same amount of matter and antimatter should have been produced after the big bang, and annihilating again. Therefore, no matter would have been left in the universe. Since apparently some matter has survived, the main question is how such a discrepancy can be explained [2]. One idea that might explain this discrepancy is a violation of the  $\mathcal{CPT}$  symmetry [3, 4].

The ASACUSA collaboration (Atomic Spectroscopy And Collisions Using Slow Antiprotons) aims to measure the hyperfine structure of the antihydrogen atom to perform an experimental test of the  $\mathcal{CPT}$  symmetry [5–8]. The experimental efforts for this goal are taking place at the Antiproton Decelerator facility (AD) in CERN. The principal method how the hyperfine splitting will be measured is a classical Rabi-type spectroscopy beam line. The Stefan Meyer Institute, which is one of the contributing collaborators within ASACUSA, took care of realising the spectrometer part of the experiment. The spectrometer basically consists of a microwave cavity to drive spin flips, a superconducting sextupole magnet, and an antihydrogen detector.

Since antihydrogen atoms are scarce, a characterisation of the spectrometer is essential to be able to do antihydrogen hyperfine measurements in reasonable time frames. The main goal of this thesis is to design and construct a beam line with similar properties as for antihydrogen, the measurement of the hyperfine splitting of atomic hydrogen by using the spectrometer part of the antihydrogen experiment, and the characterisation of the spectrometer components. An outcome of these measurements is that with one of the possible quantum state transitions, the so called  $\sigma_1$  transition, the best in beam value for the ground state hyperfine splitting at zero magnetic field was obtained.

In this work chapter 1.2 focuses on the explanation of the theoretical background for the antihydrogen measurements, chapter 2 mainly discusses the hydrogen beam development and the characterisation of the initial beam parameters, chapter 3 shows the fully assembled apparatus and describes the spectrometer instruments, chapter 4 concentrates on the analysis of the recorded data. The most important part in this work is chapter 5, which focuses on the results and the discussion of the recorded data. In the final part, chapter 6 gives a short overview and an outlook of this work.

## 1.2 Theory

### 1.2.1 $\mathcal{CPT}$ Symmetry

A  $\mathcal{CPT}$  transformation is the direct product of three individual transformations,  $\mathcal{C}$  - charge conjugation,  $\mathcal{P}$  - parity, and  $\mathcal{T}$  - time reversal.

In  $\mathcal{CPT}$  the  $\mathcal{C}$  stands for charge transformation from particle into the corresponding antiparticle.  $\mathcal{P}$ , parity, transforms the laws of physics like  $(t, x, y, z) \rightarrow (t, -x, -y, -z)$ . One can imagine parity conservation as stating that a mirror image of an experiment will produce the same results. Parity is known to be violated in weak interactions, as was proposed by Lee and Yang [9] and experimentally shown by Wu [10].  $\mathcal{T}$ , the time reversal symmetry reverses the direction of time  $(t, x, y, z) \rightarrow (-t, x, y, z)$ .

After the establishment of parity violation, physicists thought the combined transformation of  $\mathcal{CP}$  would be invariant. Cronin and Fitch showed, with Kaons, that  $\mathcal{CP}$  is also violated in weak interactions [11, 12]. Although  $\mathcal{P}$  and  $\mathcal{CP}$  violations have been observed the  $\mathcal{CPT}$  symmetry is expected to be preserved. Figure 1.1 shows an illustrative drawing of the  $\mathcal{CPT}$  symmetry. Since the  $\mathcal{CPT}$  theorem states that particles and antiparticles have the same properties, therefore, after the big bang both species should have been produced in equal amounts, annihilating again and leaving no matter. However,  $\mathcal{CP}$  violation, as being one of the Sakharov criteria, can partly describe a baryon asymmetry, but no significant number of annihilations have been observed in the universe which indicates that there are no antimatter galaxies [2]. Moreover, string theory does not necessarily conserve  $\mathcal{CPT}$  [13, 14]. These circumstances lead to the question of whether or not  $\mathcal{CPT}$  is violated [15]. If  $\mathcal{CPT}$  was broken it would imply that the Lorentz invariance is violated [16].

To date there is no experiment showing a violation of  $\mathcal{CPT}$ . Many of the experiments have been performed at high energies with high accuracy (see Particle Data Group [17]) but a violation could potentially be seen when reaching sufficient precision. Figure 1.2

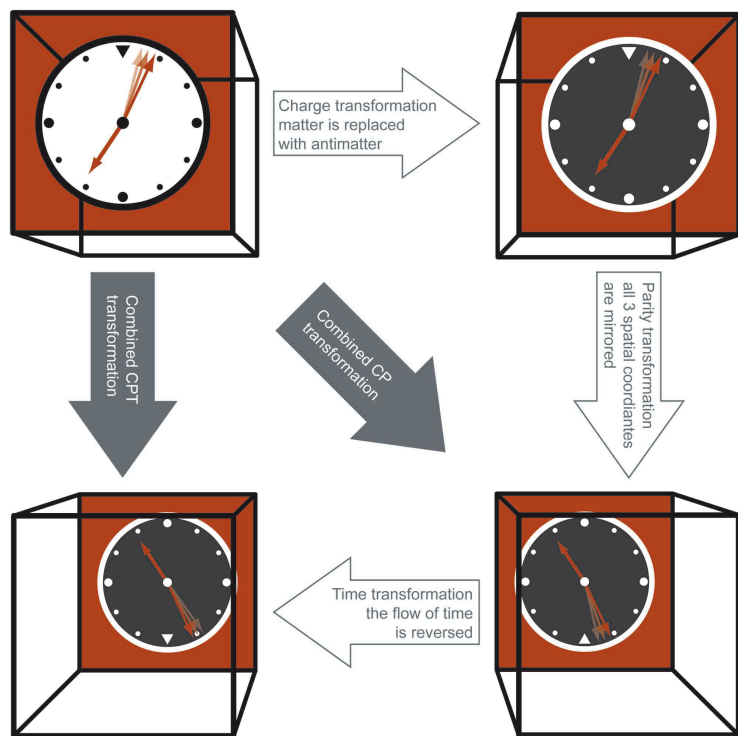


**Figure 1.1:** Symbolic illustration of the  $\mathcal{CPT}$  transformation. The top arrow pointing in the right direction replaces the particle with its antiparticle. A  $\mathcal{C}$  transformation is achieved by a further transformation involving the parity operator. The time transformation yields the fundamental  $\mathcal{CPT}$  symmetry (arrow pointing bottom left).

shows  $\mathcal{CPT}$  tests for different experimental systems [17]. The top  $\mathcal{CPT}$  test is a mass comparison in the leptonic sector with electron - positron [18], the second test shows the neutron - antineutron mass comparison in a bubble chamber [19, 20], the third test shows the proton - antiproton charge to mass ratio [21], and the fourth shows the  $K^0 - \bar{K}^0$  mass difference [22]. Below, these tests are shown for atomic transitions in hydrogen (1s-2s, hyperfine transition) and the precision of the measurements for hydrogen alone.

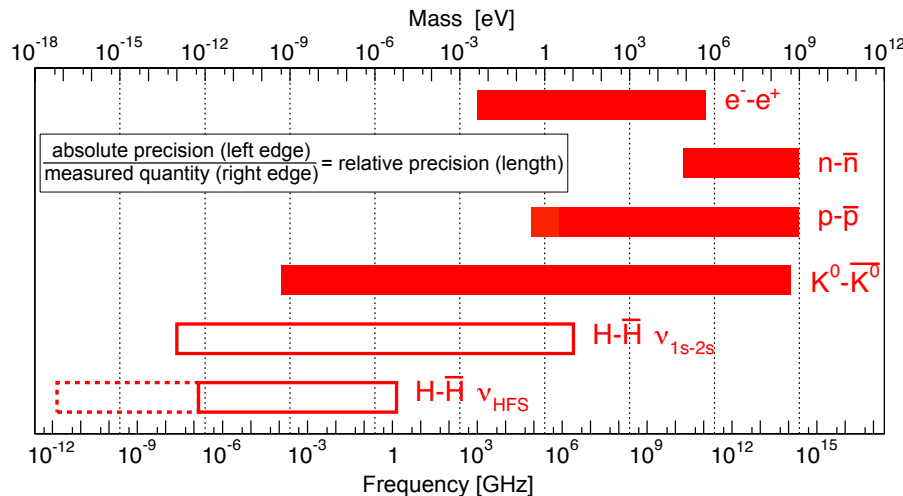


**Figure 1.2:** Filled bars: mass determination; open bars: frequency measurement of atomic energy level differences. The top four bars show comparison of various  $\mathcal{CPT}$  tests. The top x axis shows the mass in  $\text{eV}/c^2$ , the bottom x axis shows the corresponding energy converted into a frequency (GHz). The right end of the red bars shows the absolute value for the measured quantities and the length of the bars shows the relative precision. The relative precision in the kaon system achieved the outstanding level of  $6 \times 10^{-19}$ , however even with a smaller relative precision, the antihydrogen measurements have the potential to extend the  $\mathcal{CPT}$  tests to higher absolute precision [8].

The physical properties of atomic hydrogen are some of the most precisely measured values in physics. Some quantities such as the 1s-2s transition [23] or the hyperfine transition [24–26], are known with high accuracy and high precision. Figure 1.3 shows these transitions for hydrogen. Experiments are performed to compare hydrogen with antihydrogen, its atomic antimatter pendant. The comparison of both atoms could test the  $\mathcal{CPT}$  theorem with high sensitivity and extend the theorem to even lower energy scales. The ASACUSA collaboration aims to measure the ground state hyperfine splitting of antihydrogen ( $\bar{H}$ ) and test  $\mathcal{CPT}$  symmetry at the AD facility in CERN [7].

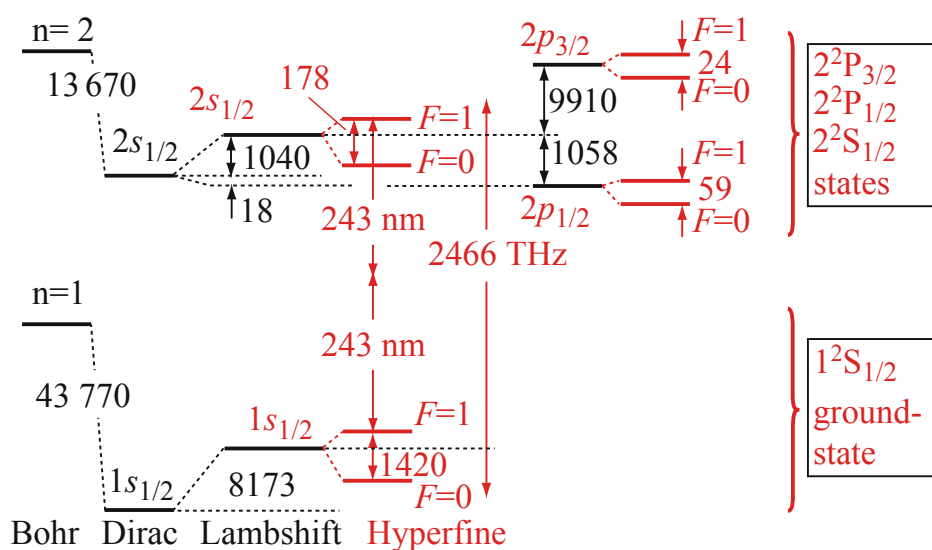


**Figure 1.3:**  $n=1$  and  $n=2$  states for atomic hydrogen (not to scale). The numbers show the energy splitting and are given in MHz. Beside the hyperfine structure with a frequency of 1420 MHz, the  $1s$ - $2s$  transition can also be seen, which is a two photon transition. ( $2 \times 243$  nm) (adapted from [27]).

### 1.2.2 Standard Model Extension

A framework which could describe  $\mathcal{CP}\mathcal{T}$  violation in hydrogen and antihydrogen is the so called minimal standard model extension (SME). In this model V.A. Kostelecký and his group add  $\mathcal{CP}\mathcal{T}$  and Lorentz invariance violating terms with corresponding coefficients

$$\begin{aligned}\Delta E^H(m_J, m_I) = & a_0^e + a_0^p - c_{00}^e m_e - c_{00}^p m_p \\ & + (-b_3^e + d_{30}^e m_e + H_{12}^e) m_J / |m_J| \\ & + (-b_3^p + d_{30}^p m_p + H_{12}^p) m_I / |m_I|\end{aligned}\quad (1.1)$$

to the quantum field theory Lagrangian [28], which would modify the atomic level energies. In equation 1.1  $m_J$  and  $m_I$  are the spin quantum numbers for proton (antiproton) and electron (positron),  $m_p$  the proton (antiproton) mass,  $m_e$  the electron (positron) mass.  $a$ ,  $d$  and  $H$  change their sign in the case of antihydrogen which could cause a different frequency for the hyperfine splitting. A possible consequence in the hyperfine structure can be seen in figure 1.4. Since the parameters  $a$  and  $b$  have the dimension of an energy, it follows that for a test of  $\mathcal{CP}\mathcal{T}$ , in the ground state hyperfine splitting the absolute precision is decisive rather than the relative precision. For instance,  $\mathcal{CP}\mathcal{T}$  has been tested to a relative precision of  $10^{-19}$  by mass comparison of the neutral kaons. On the contrary, the hyperfine structure transition is only  $5.9 \mu\text{eV}$  and a measurement in antihydrogen to a relative precision of  $10^{-4}$  can yield a  $\mathcal{CP}\mathcal{T}$  test of the same absolute sensitivity as the kaon experiment. However, within the SME the  $(F, M) = (1, 0)$  state would remain unaffected leading to no change in the  $\sigma_1$  transition. Therefore, the  $\pi_1$  transition would be preferential for testing the SME.

Apart from the so far used "minimal SME" a non minimal SME is available. The main difference between those two is that for the minimal SME operators have mass dimension  $d \leq 4$ , whereas in the the non minimal SME  $d$  can be greater than 4 which yields a noncommutative quantum field theory [29].

### 1.2.3 Hyperfine structure

The hyperfine structure in the spectrum of atomic systems arises from the interaction of the magnetic moments of the nucleus with the bound electrons. The total angular momentum of hydrogen/antihydrogen  $\vec{F}$  is a coupling of the electron/positron angular momentum  $\vec{J}$  and the angular momentum of the proton/antiproton  $\vec{I}$ :  $\vec{F} = \vec{J} + \vec{I}$ . The 1s ground state splits up into a singlet state where  $F = 0 \Rightarrow (F, M) = (0, 0)$  ( $M$  being the projection

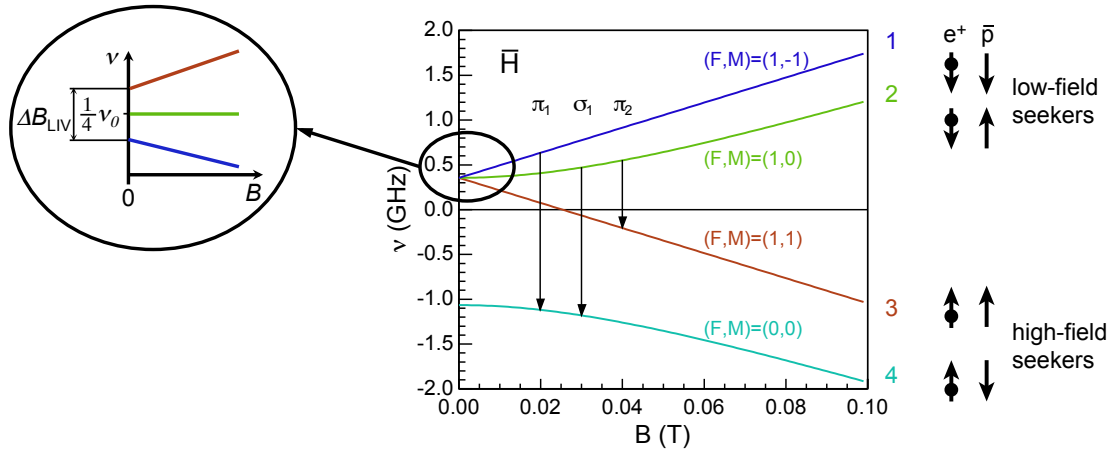


**Figure 1.4:** Breit Rabi diagram for antihydrogen. If  $\mathcal{CPT}$  symmetry is violated in the hyperfine structure, a consequence of this could be, according to the Kostelecký group, observed at zero magnetic field. Also shown in the graph: a transition from one state to the other can be driven with an oscillating magnetic field (microwaves). The different states are called  $\sigma_1$ ,  $\pi_1$ , and  $\pi_2$  transition (graph adapted from [6]).

of  $\vec{F}$  onto the magnetic field axis) and a triplet state where  $F = 1$  and  $M = -1, 0, 1 \Rightarrow (F, M) = (1, -1), (1, 0), (1, 1)$  (see figure 1.5 for an illustration). These states also have different energies at zero external magnetic field. The energy difference, also known as the ground state hyperfine splitting, is directly proportional to the magnetic moments of electron (positron) and proton (antiproton).

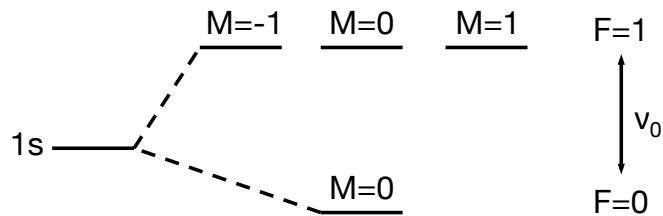


**Figure 1.5:** The  $1s$  state splits up into a singlet state with  $F = 0$  and a triplet state with  $F = 1$  and  $M = -1, 0, 1$

The hyperfine coupling is given by the Fermi contact interaction.

$$\nu_0 = \frac{16}{3} \left( \frac{M_p}{M_p + m_e} \right)^3 \frac{m_e \mu_p}{M_p \mu_N} \alpha^2 c R_\infty (1 + \delta) \quad (1.2)$$

Here  $\hbar = c = 1$ , with  $M_p$  the proton mass,  $m_e$  the electron mass,  $\mu_p$  the proton spin magnetic moment,  $\mu_N$  the nuclear magneton and  $R_\infty$  the Rydberg constant.  $\delta$  are mainly

**Table 1.1:** States of (anti) hydrogen ordered according to their behaviour when exposed to magnetic field gradients. Note that the states (1,1) and (1,-1) are swapped for hydrogen and antihydrogen.

	hydrogen (F,M)	antihydrogen (F,M)
HFS states	(0,0), (1,-1)	(0,0), (1,1)
LFS states	(1,0), (1,1)	(1,0), (1,-1)

higher order QED corrections and non-relativistic magnetic size correction (Zemach correction) [30–33].

Experimentally first beam techniques for a measurement of hyperfine transitions were established in the 1930s [34]. In the 1950s the best in beam measurements resulted in a relative precision of  $3.5 \times 10^{-8}$  [35, 36]. Later, when the maser was invented, a relative precision to better than one part in  $10^{-12}$  could be achieved for  $\nu_0$ . The value in the absence of a magnetic field has been determined as [24, 26]:

$$\nu_0 = 1\,420\,405\,751.768 \pm 0.002 \text{ Hz} \quad (1.3)$$

The precision of a maser, however, cannot be transferred one to one to antihydrogen since in a maser hydrogen is captured in a box with teflon walls. If antihydrogen were to hit the teflon walls, it would immediately annihilate.

In the presence of a magnetic field the energy levels split up due to the Zeeman effect. They can be classified according to their behaviour in an inhomogeneous magnetic field with the Stern Gerlach effect. For hydrogen, two states,  $(F, M) = (1, -1)$  and  $(0, 0)$ , move towards higher magnetic fields, whereas the two states  $(F, M) = (1, 1)$  and  $(1, 0)$  move towards lower magnetic fields. Therefore, these states are often called high-field seeker (HFS) and low-field seeker (LFS), respectively. It has to be noted that due to the opposite charge of the constituent particles of antihydrogen the high field and low field seeking states are switched as shown in table 1.1 [7].

The classification of the states is illustrated in a Breit Rabi diagram (figure 1.6) which shows the energy of the hyperfine states depending on the magnetic field.

The Breit Rabi diagram shows the energy shifts of the four states caused by the interactions of the spins and an external magnetic field. The four states are defined by the Rabi formulas of atomic hydrogen [27, 38, 39]:

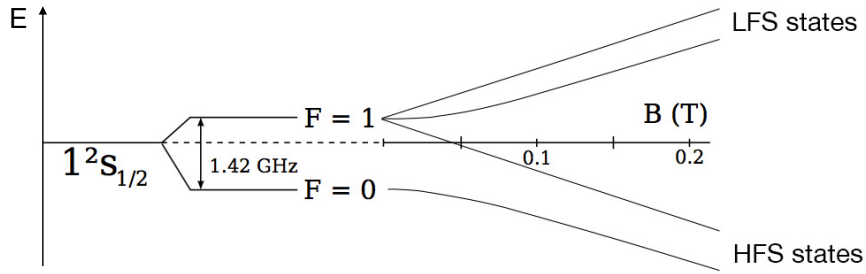


**Figure 1.6:** Breit Rabi diagram of hyperfine structure of atomic hydrogen. The states split up in the presence of the magnetic field. The states can be pooled into two different subgroups due to their behaviour in an inhomogeneous magnetic field according to the Stern-Gerlach effect. The low field seeking states (LFS states) tend to move to lower magnetic fields, whereas the high field seeking states (HFS states) move to higher magnetic fields (graph taken from [37]).

$$E_{(1,1)} = \frac{1}{4}E_0 + \frac{1}{2}(g_J + g_I)\mu_B B \quad (1.4)$$

$$E_{(1,0)} = -\frac{1}{4}E_0 + \frac{1}{2}E_0\sqrt{1+x^2} \quad (1.5)$$

$$E_{(1,-1)} = \frac{1}{4}E_0 - \frac{1}{2}(g_J + g_I)\mu_B B \quad (1.6)$$

$$E_{(0,0)} = -\frac{1}{4}E_0 - \frac{1}{2}E_0\sqrt{1+x^2} \quad (1.7)$$

with  $E_{(F,M)}$  being the energy of state  $(F, M)$  relative to the spin averaged energy,  $E_0 = h\nu_0$  the energy splitting in absence of a magnetic field and  $\nu_0$  transition frequency at zero magnetic field,  $B$  the external magnetic field,  $g_J = 2.0023193043622(15)$  [40] the Landé factor of the coupled spin angular momentum ( $g_I$  equals  $|g_e|$  for  $J = 1/2$ ),

$$g_I = g_p m_e / m_p \quad (1.8)$$

with  $g_p = 5.585694713(46)$  the proton  $g$ -factor,  $m_e = 9.10938291(40) \times 10^{-31}$  kg the electron mass,  $m_p = 1.672621777(74) \times 10^{-27}$  kg the proton mass [40].  $x = B/B_0$  where

$$B_0 = \frac{2\pi\nu_0}{(g_J - g_I)\mu_B} \quad (1.9)$$

and  $\mu_B = 5.7883817555(79) \times 10^{-5}$  eV T<sup>-1</sup> [40] the Bohr magneton. A detailed derivation of the Rabi formulas is presented in the section Zeeman splitting in Bethe-Salpeter's "Quantum Mechanics of One- and Two-Electron Atoms" [41].

Two transitions are of special relevance for the present thesis. The transition from  $E_{(1,0)}$  to  $E_{(0,0)}$ , which is also called the  $\sigma_1$  transition, results in a magnetic field dependent frequency of

$$\nu_{\sigma 1} = (E_{(1,0)} - E_{(0,0)})/h = \left( E_0 \sqrt{1 + x^2} \right) / h \quad (1.10)$$

whereas for the so called  $\pi_1$  transition from  $E_{(1,1)}$  to  $E_{(0,0)}$  a frequency of

$$\nu_{\pi 1} = (E_{(1,1)} - E_{(0,0)})/h = \left( \frac{1}{2}E_0 - \frac{1}{2}(g_J + g_I)\mu_B B + \frac{1}{2}E_0 \sqrt{1 + x^2} \right) / h \quad (1.11)$$

is obtained.

## 1.3 Experimental principle

### 1.3.1 Rabi experiment

Isidor Isaac Rabi (together with S. Millman, P. Kusch and J.R. Zacharias) invented the magnetic resonance technique in the 1930s [34], which is also referred to as the Rabi technique. He was awarded the 1944 Nobel prize for his invention, which is a powerful tool for the study of the magnetic properties of atomic nuclei. Figure 1.7 illustrates the technique.

For the case of hydrogen an atomic beam is formed. The beam is being spin polarised in an inhomogeneous magnetic field due to the Stern Gerlach effect (A magnet). During this step the high field seekers search their way towards higher magnetic fields and consequently cannot pass a slit S, whereas low field seekers will pass. Radio frequency waves radiate into region C, which induce a spin flip from one atomic state to another. In the second magnet (B magnet) another inhomogeneous field is present which selects the spin component once more. If the radio frequency field was set to the hyperfine frequency, low field seekers perform a transition to high field seeking states. Magnet B will sort out these states which results in a drop in counting rate at the detector D [42].

A phenomenological explanation for the spin flips was given by Ramsey in his Nobel prize lectures [43]. Consider a hydrogen atom in a static magnetic field  $B_{\text{stat}}$ . With a classical approach the nucleus of the atom will precess with the Larmor frequency  $\nu_0$  and angular frequency  $\omega_0$  around the magnetic field due to the torque on the nuclear angular momentum  $J$  (see figure 1.8). In addition, consider an oscillating magnetic field  $B_{\text{osc}}$

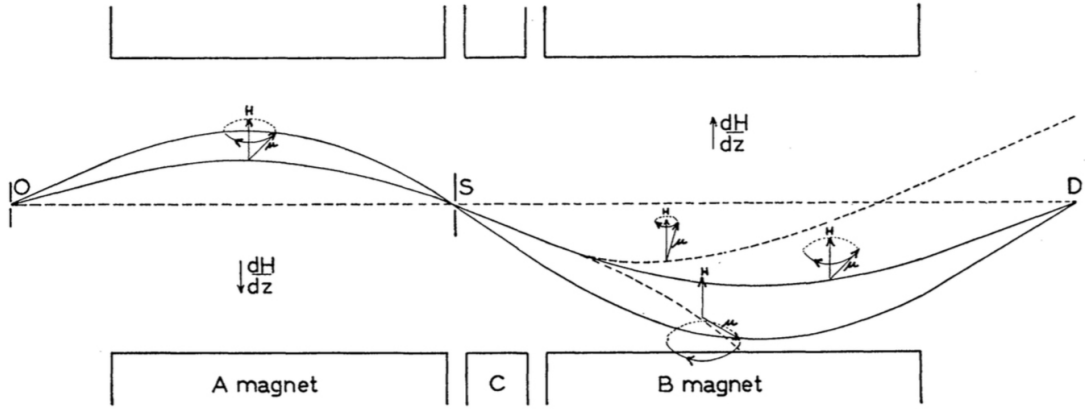


**Figure 1.7:** Original illustration of the Rabi setup (here used to measure the magnetic moments of Li and F). The atoms exit an oven, and are then spin selected in an inhomogeneous magnetic field (shows as A magnet) due to the Stern-Gerlach effect. LFS states will pass a slit into the C region where a radio frequency field is used to induce spin flips and drive LFS states into HFS states. In the second magnet (B magnet) - the analysing magnet - HFS states are sorted out and LFS states pass towards detector. If the frequency was tuned to induce spin flips a drop in counting rate should be visible in the detector D (taken from [34]).

perpendicular to the static magnetic field with angular frequency  $\omega$ . If  $B_{\text{osc}}$  is perpendicular to the  $B_{\text{stat}} - J$  plane it will stay perpendicular as long as  $\omega = \omega_0$ .

$$\omega_0 = 2\pi\nu_0 = \frac{\mu B_{\text{stat}}}{\hbar I} \quad (1.12)$$

Due to the additional magnetic field the nucleus will once more start precessing by changing the angle  $\phi$  with respect to  $\vec{B}_{\text{stat}}$ . Therefore, the nucleus will change orientation, and periodically perform spin flips. If  $\omega \neq \omega_0$ ,  $B_{\text{osc}}$  will not stay perpendicular to  $J$ ,  $\phi$  will increase for a short time and then decrease again. Therefore, on average no net change will appear [43].

### 1.3.2 Antihydrogen experimental setup overview

Within ASACUSA the Stefan Meyer Institute has designed and built a spectrometer beam line for the measurement of the hyperfine structure of antihydrogen. The  $\bar{H}$  atoms can be produced by mixing its constituent particles in a trap. The antiparticle to the proton is the antiproton  $\bar{p}$ . At CERN antiprotons are produced by impinging 26 GeV/c protons on an iridium target.  $\bar{p}s$  with a momentum of 3.5 GeV/c are injected into the AD by a magnetic

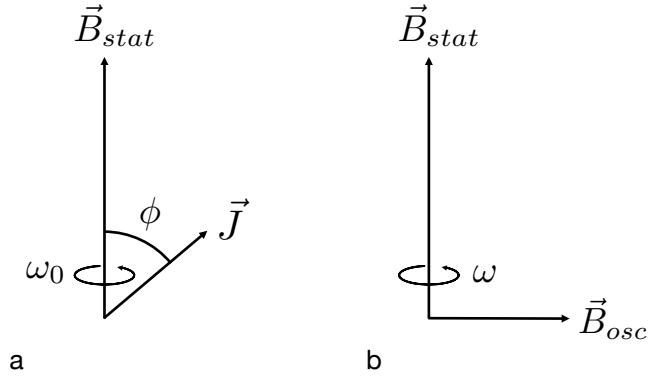


**Figure 1.8:** a) precession of the nuclear magnetic moment  $J$  around the static magnetic field  $\vec{B}_{\text{stat}}$ . b) magnetic field  $\vec{B}_{\text{osc}}$  rotating around the static magnetic field  $\vec{B}_{\text{stat}}$  (Illustrations inspired by [43])

horn [44, 45]. In order to provide  $\bar{p}$  for low energy experiments they need to be decelerated. CERN is the only facility in the world, where slow  $\bar{p}$  are available.

Slowing the particles down is done at the Antiproton Decelerator (AD). Here the momentum and beam emittances are reduced (momentum from 3.5 GeV/c to 100 MeV/c). When the  $\bar{p}$  are injected into the experimental zone they have a momentum of 100 MeV/c [46]. In the ASACUSA experimental zone further deceleration takes place in an RFQD [47] (radio frequency quadrupole decelerator) where the energy is reduced from 5.3 MeV to 115 keV. Before the antiprotons are finally caught in a penning trap (Musashi trap [48]) they pass a thin mylar foil (two foils with  $90 \mu\text{g cm}^{-2}$ ) which further decelerates them. In contrast to other groups at the AD, the RFQD enables ASACUSA to catch 5-50 times more antiprotons per AD-cycle (typically 100 seconds long [49]). The  $\bar{p}$  are electron-cooled and radially compressed by a rotating electric field in the Musashi trap [48].

In parallel the second constituent of antihydrogen, the positron ( $e^+$ ) is delivered by a radioactive source via  $\beta^+$  decay ( $^{22}\text{Na}$  activity 0.6 GBq). The  $e^+$  are moderated in neon ice and thermalised in a buffer gas filled ( $\text{N}_2/\text{CF}_4$ ) MRE (multi ring electrode) trap [50, 51]. Subsequently, both of the constituents are transferred to the mixing trap (CUSP trap), where the antihydrogen atom is formed/created [52].

In the CUSP trap strong magnetic field gradients are generated by an anti Helmholtz configuration as can be seen in figure 1.9. Neutral particles escape and form a beam of antihydrogen atoms. The main advantage of the cusp trap is that slow LFS states are focused and additionally the magnetic field strength decreases rapidly, so that the beam reaches a “field free region” close to the trap [53, 54]. When exiting the CUSP, the beam

should be partially spin polarised (according to simulations the ratio HFS/LFS is 30/70) which spares an additional polarising Stern Gerlach magnet [55].

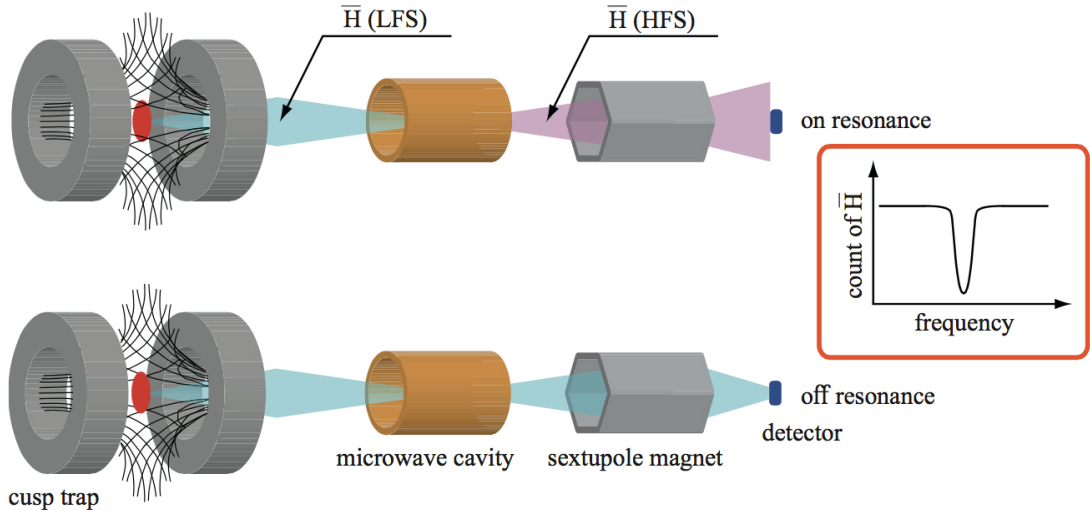


**Figure 1.9:** Rabi like setup for the antihydrogen experiment. The antiprotons and positrons are confined in an anti-Helmholtz coil (cusp trap), where the two non-neutral plasmas are mixed to form antihydrogen. The neutral atoms can exit the cusp trap already with a spin polarisation. In the microwave cavity (if tuned to the right frequency) the LFS states are converted into HFS states (top picture). In the sextupole magnet, which acts on HFS as a defocusing (on LFS as a focusing) element, the beam is spin-analysed resulting in a drop in counting rate at the detector as indicated in the red box. The lower diagram shows the result of the microwave cavity not being tuned to the resonance frequency. Here the LFS states stay LFS states and consequently the sextupole magnet acts as a lens and the baseline counting rate is detected (taken from [7]).

The atoms move on through a microwave resonator (cavity) where a standing wave of oscillating magnetic field flips the spins (see again the Breit Rabi graph 1.4). The analysing magnet is a superconducting sextupole magnet which has the advantage that it focuses low field seekers, whilst defocusing high field seekers, analogously to a convex lens and concave lens, respectively. Depending now on the initial spin state, the beam is focused or defocused. If the spin has been flipped, a drop in counting rate will be observed at the detector [7, 56].

### 1.3.3 Hydrogen setup overview

The limited availability of antiprotons at CERN, and low production rates of antihydrogen itself, hinder a precise characterisation of the two main components of the spectrometer beam line - the superconducting sextupole magnet and the spin flip cavity. Therefore, a

hydrogen beam experiment was designed and constructed for comprehensive tests of the instruments. Figure 1.10 shows a schematic drawing of the hydrogen beam line individual components.

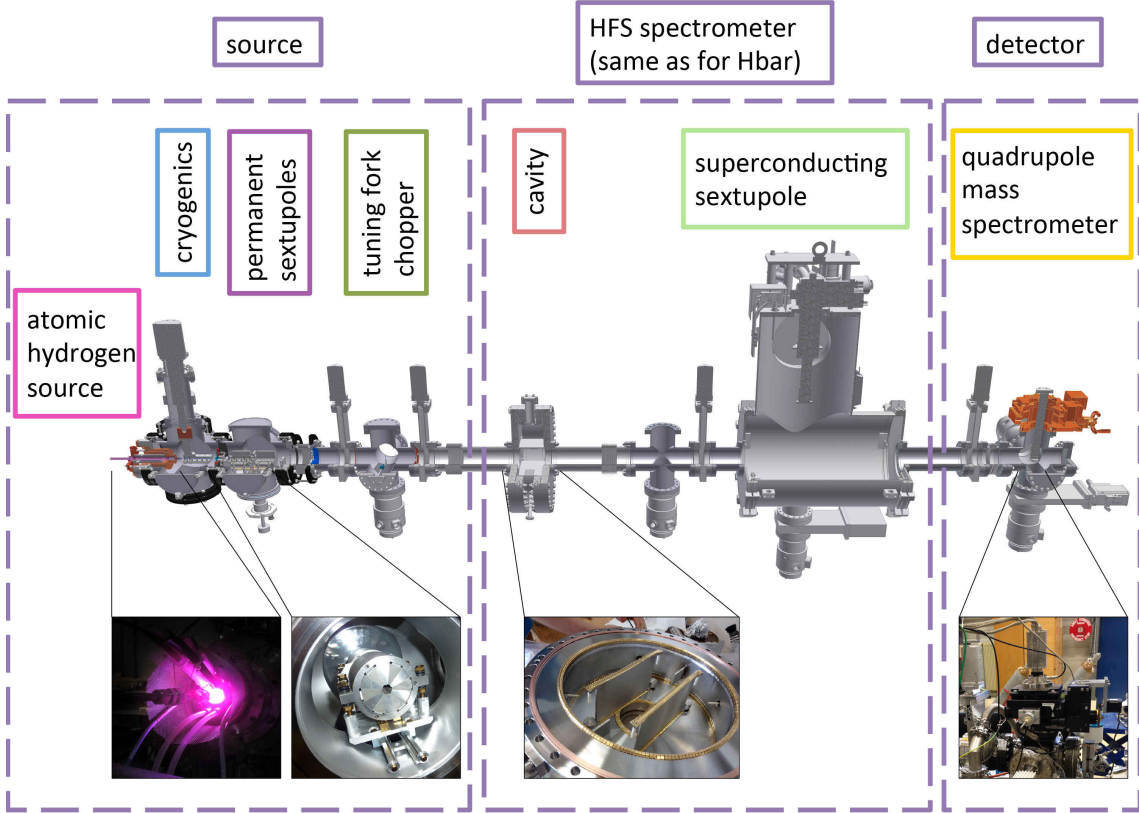


**Figure 1.10:** Technical drawing of the hydrogen beam line. The microwave cavity and superconducting sextupole magnet are the same as being used in the antihydrogen experiment. In the microwave plasma source, atomic hydrogen is produced by splitting molecular hydrogen (pink picture). A set of permanent sextupole magnets perform the initial spin selection, which is taken care of by the magnetic field of the cusp trap in the antihydrogen experiment. Next the microwave cavity performs the spin flips. In the following step the superconducting sextupole magnet is used to analyse the beam. Finally, the beam is detected with a mass spectrometer.

The main difference compared to the antihydrogen experiment is a plasma source to provide atomic hydrogen. The particles are cooled to a desired temperature regime with the help of a PTFE tubing led through the coldfinger of the coldhead of a cryocooler. In contrast to the partly spin polarising features of the cusp trap, hydrogen leaves the plasma source unpolarised. Thus, a set of permanent sextupole magnets polarises the beam by sorting out high field seekers. Since background signals from residual gases are an issue, the experiment is performed in AC mode rather than DC mode. Accordingly, a tuning

fork chopper modulates the beam. After this step the aforementioned spin flip cavity induces hyperfine transitions and the superconducting sextupole magnet analyses the beam. Finally, a mass spectrometer is detecting the beam by using phase sensitive techniques in conjunction with the chopper.

## 2 Hydrogen beam development and characterisation

The initial ideas of the design needs for a hydrogen beam line have already been described in reference [57]. Before establishing the performance of the spin flip cavity and the superconducting sextupole magnet according to the specifications, the hydrogen source and detector have been operated in a stand-alone configuration for a more direct characterisation of the source parameters. The individual sections of this configuration and their purposes are listed below and described in detail in this chapter. (see also figure 2.1):

- **hydrogen source** to provide atomic hydrogen,
- **coldhead** - for cooling the beam and hence reducing the velocity of the H atoms,
- a set of **permanent sextupole magnets** for an initial polarisation of the hydrogen atoms,
- **tuning fork chopper** for a modulation of the beam to allow for TOF measurements,
- **quadrupole mass spectrometer (QMS)** for ionisation and detection of protons ( $H^+$ ), while suppressing ions of other masses.

These components have been tested individually before being integrated step by step into the stand-alone setup. As depicted in Fig. 2.1. the beam traverses the four chambers, which are separated by apertures for differential pumping. The pressure improves from typically  $10^{-5}$  mbar in the source chamber to  $10^{-10}$  mbar in the detection chamber. Every chamber was pumped with a turbo molecular pump and the last chamber was additionally pumped with a getter pump. In the last chamber a QMS is measuring the beam locked in to the reference signal of the chopper (lock-in amplifier).

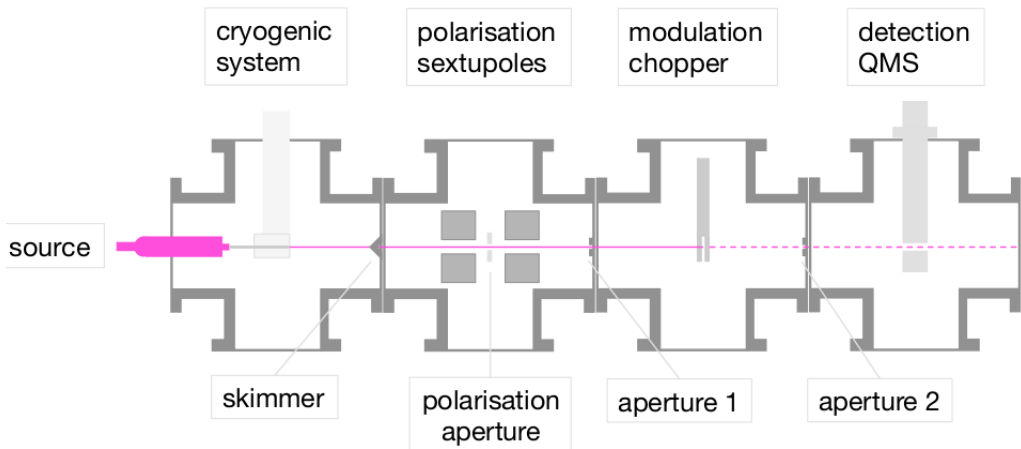


**Figure 2.1:** Sketch of the stand-alone setup consisting of the hydrogen source and detector only. A skimmer and two apertures realised a differential pumping vacuum system. Hydrogen is moving through a PTFE tubing connected to a cryogenic system where the beam temperature can be increased or reduced. In the next step a set of two permanent sextupoles polarises the beam. The magnets also cut out a certain velocity component of the beam, a polarisation aperture stops the high field seeking states. After this step the beam is being modulated with a tuning fork chopper to allow for time of flight measurements and background suppression. Finally, a QMS which is tuned to the proton's mass-to-charge ratio, efficiently counts ionised atomic hydrogen (protons) using a SCEM (single channel electron multiplier).

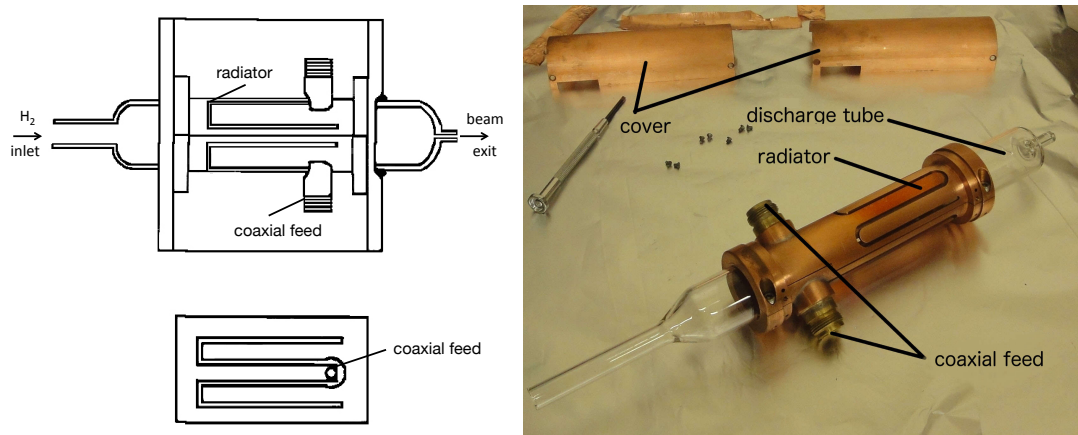


**Figure 2.2:** Left: design of the discharge tube (sketch taken from reference [58]). Right: photograph for illustration of the plasma source. Microwaves are introduced via two N-type coaxial connectors, the slotted line antennas radiate into the glass tube and form a  $TE_{00}$  mode. In operation molecular hydrogen is introduced at the inlet, and the plasma is ignited with a spark. At the right side the atoms can exit into the vacuum system.

## 2.1 Hydrogen source

Providing an atomic hydrogen beam of sufficient intensity requires the dissociation of  $H_2$ . Our source closely follows the design and operation principles of the setup by McCullough et al. [58–60]. Microwaves with a frequency of 2.45 GHz were coupled to a cylindrical pyrex glass tube through twin slotted Lisitano type radiators to maintain a plasma. The source provided an electric field configuration with a  $TE_{00}$  mode. The diameter of the slotted radiator was independent of the frequency. During operation molecular hydrogen was introduced at one end and cracked. At the other end atomic hydrogen exited through a small orifice into a vacuum system with a flux around 0.2 sccm<sup>1</sup> (corresponding to an atom beam density of  $4 \times 10^{13}$  atoms  $cm^{-3}$ ). Figure 2.2 shows the design and a photo of the discharge tube.

A Packard 9100 hydrogen generator provided ultra pure hydrogen gas via electrolysis of deionised water. This design was important to run the hydrogen source for months without the need of cleaning.  $H_2$  was introduced into the H-source with an electronically controllable Brooks SLA5850 flow meter. A Sairem solid state microwave generator with a maximum power of 200 W tuneable in frequency between 2.43-2.47 GHz produced the microwaves that were fed with two N-type connectors and coaxial cables into the pyrex tube. The plasma was started with a spark gun. Typical microwave power for ignition were 30 W with a  $H_2$  flow rate of 0.6 sccm. When running the power was set to 60 W to have stable plasma conditions. Since the microwave generator could be tuned in frequency, settings were established where the reflected power was reduced to a minimum around 0-4 W during hydrogen-plasma operation. Figure 2.3 (left) shows a picture of the plasma with hydrogen, (right) shows the visible spectrum of the plasma as seen through a hand spectrometer. The three strongest lines are the visible transitions of the Balmer series ( $n > 2 \rightarrow n = 2$ ). The picture shows clear indications that atomic hydrogen is formed.

Figure 2.4 presents the cracking efficiency for the plasma source at typical operation pressures. McCullough et al. defined the cracking efficiency as:

$$D = (H_2^{off} - H_2^{on})/H_2^{off} \quad (2.1)$$

with  $D$  the dissociation fraction,  $H_2^{off}$  the  $m/q = 2$  (mass to charge ratio) amount of molecular hydrogen when the plasma was not turned on, and  $H_2^{on}$  the the  $m/q = 2$  amount of molecular hydrogen when the plasma was ignited.

---

<sup>1</sup>1 sccm =  $4.5 \times 10^{17}$  atoms/second [61]

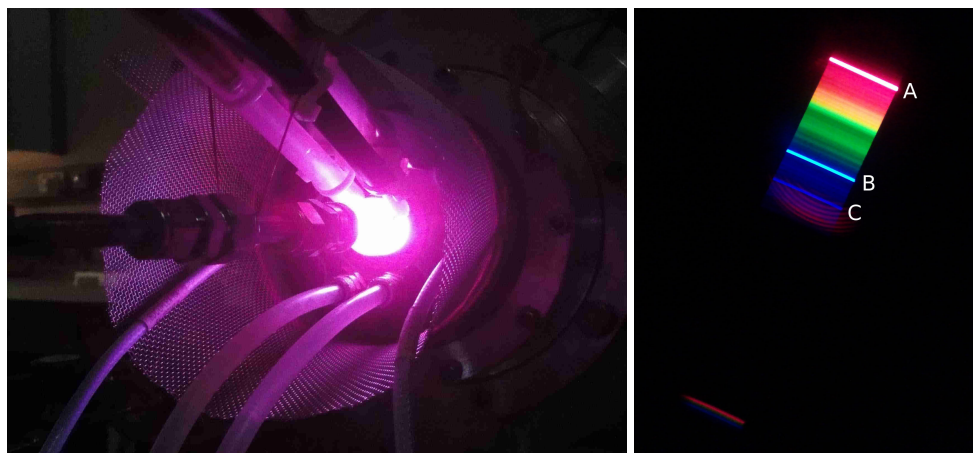


**Figure 2.3:** Left: photo of the plasma during operation. Right: picture taken with hand spectrometer. Balmer series: A: H- $\alpha$  spectral line (n: 3  $\rightarrow$  2), B: H- $\beta$  spectral line (n: 4  $\rightarrow$  2), C: H- $\gamma$  spectral line (n: 5  $\rightarrow$  2)

For the 0.6 sccm H<sub>2</sub> gas flow up to 75 % cracking efficiency were measured (see figure 2.4). Since in the literature a cracking efficiency of 90 % for the case of atomic hydrogen was reported some discrepancy is present. One explanation for the difference will be discussed in section 2.3.7. There a saturation effect for higher count rates (1 million counts/sec) was observed. This effect was present for molecular hydrogen measurements. To overcome these problems it was necessary to change the resolution of the QMS which increased the DAQ time or resulted in reduced statistics.

## 2.2 Mass spectrometer

One requirement on the detection system was the capability of discriminating the beam signal against huge background signals from residual gases. For this purpose a quadrupole mass spectrometer in conjunction with a tuning fork chopper for beam modulation were installed as a sensitive lock-in amplification (LIA) scheme [62].

A MKS - Microvision 2 100 D residual gas analyser in cross beam configuration served as a QMS. In this context cross beam configuration means that the QMS was mounted perpendicular to the beam axis. Beam atoms as well as residual gas were ionised through electron impact ionisation. The QMS was tuned to exclusively guide ions with charge-to-mass ratio of the species of interest to the detector. The SCEM (single channel electron multiplier), operated at high voltages to enable measurements of single particles, amplified the signals of the ions of interest. As an alternative to the SCEM a faraday cup was

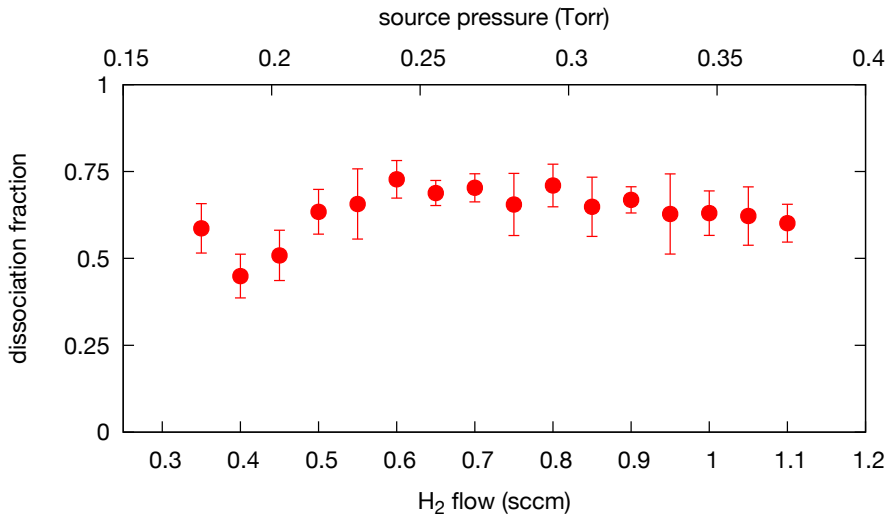


**Figure 2.4:** Characterisation of the plasma tube. The dissociation fraction (cracking efficiency) vs. molecular hydrogen flow or source pressure, respectively (second x axis).

available. The voltage was supplied externally with a CAEN - N1471A HV NIM module (typically 2300 - 2500 V). The pulses from the SCEM were fed out from the mass detector into an amplifier (LeCroy - LRS 333). The signal was magnified by 20 dB. A CAEN mod. 84 NIM discriminator converted the signals into digital pulses, which were again converted by a LeCroy 688AL from NIM to TTL. The TTL pulses were transferred into the counter of a National Instruments PCIe-6361 X-series multi function data acquisition card. Afterwards the signals were stored on the personal computer (see figure 2.5 for a typical single particle pulse and the digitisation diagram).

The lock-in amplifier which was used to discriminate the signal from the background was purely software based. The phase information of the tuning fork chopper (see section 2.4.1) was obtained by feeding the monitor signal of the chopper driver to a sampling voltage input of the NI x-series ADC module. The software separated the modulated content of the count rate from the background rate [62]. The main background signal left in the identified beam rate for  $m/q = 1$  came from a modulated molecular hydrogen component. The beam contained H<sub>2</sub> due to the fact that the atomic hydrogen source had a cracking efficiency smaller than one. H<sub>2</sub> had a certain probability to form protons at the ionisation housing of the QMS ( $e^- + H_2 \rightarrow p + H + e^- + e^-$ ) and therefore added a wrongly identified component to the lock-in amplified signal. The cross section for this process is smaller than for  $e^- + H_2 \rightarrow H_2^+ + e^- + e^-$ . Also compared to atomic hydrogen

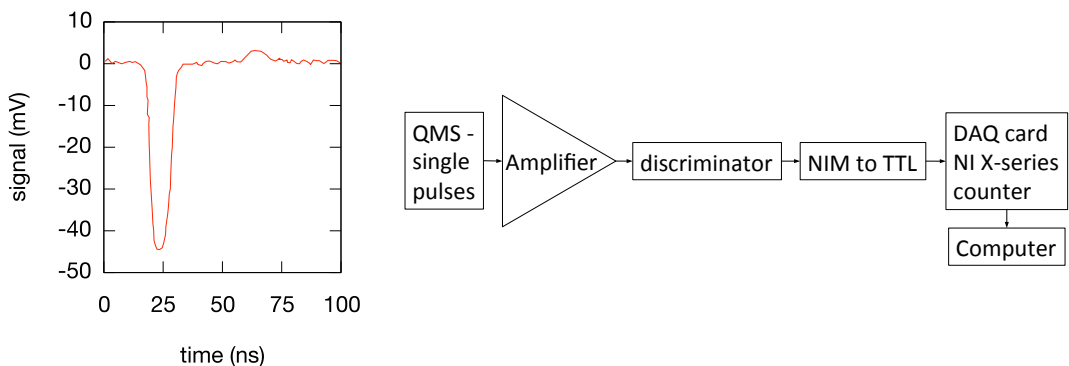


**Figure 2.5:** DAQ scheme for the ion count rate. Left: typical single ion pulse from the SCEM measured with an oscilloscope. Right: schematic diagram of the digitisation of the measured pulses. The pulses coming from the QMS are amplified and a discriminator triggers events at a certain threshold. The NIM signals are converted to TTL signals which are accepted by a NI counter. The NI card counts the events and transfers them to the computer.

$(e^- + H \rightarrow e^- + p + e^-)$  the cross section is small [63], nevertheless, it had to be considered as a contributing background. Figure 2.6 shows cross sections for these processes.

## 2.3 QMS tuning

An important task was the preparation of the quadrupole mass spectrometer (QMS). Since ex factory these instruments are typically tuned to fit to a broad range of masses the instrument had to be tuned for an optimised operation with atomic hydrogen [64, 65].

For the QMS optimisations could be done for

- **emission current**
- **electron energy**
- **extraction potential**
- **ion energy**
- **pole bias**
- **mass alignment**

The tuning parameters are illustrated in figure 2.7.

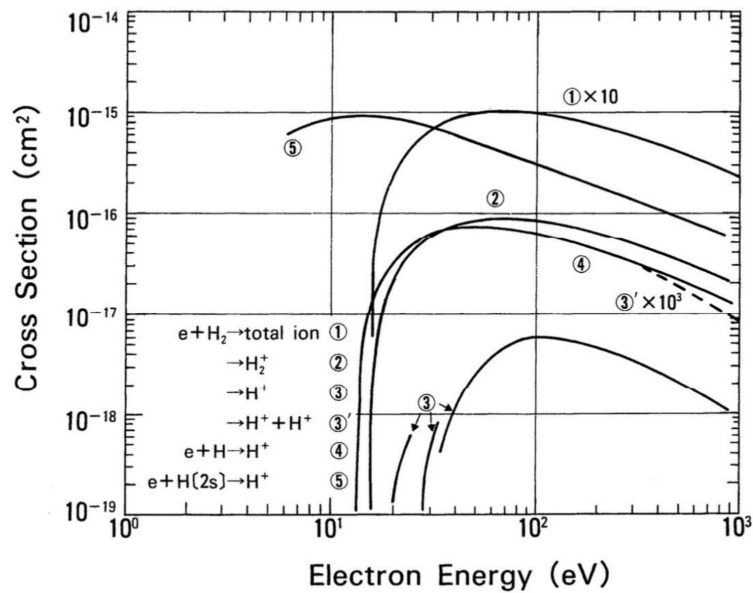


**Figure 2.6:** Cross sections for various processes with molecular and atomic hydrogen. Taken from [63].

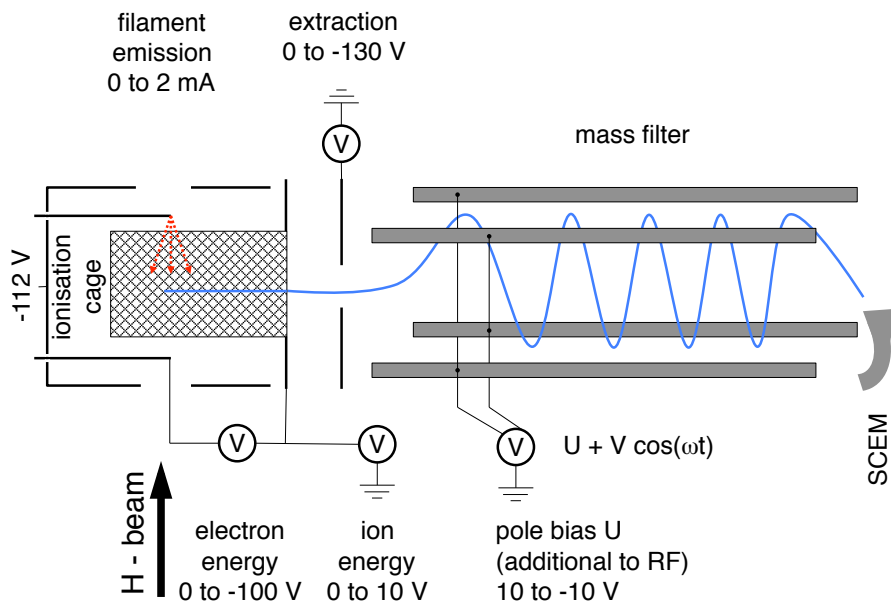


**Figure 2.7:** Illustration of the tuning parameters [64].

### 2.3.1 Emission current

The emission current defines the current of emitted electrons into the ionisation cage of the QMS. This quantity could be varied between 0 and 2 mA. In order not to compromise the filament life time the current was held at the factory setting of 1 mA.

### 2.3.2 Electron energy

Electron energy corresponds to the energy of the electrons in the QMS ionisation cage. The residual gas is ionised by means of electron bombardement. The parameter can be optimised to the cross section for the gas of interest. Figure 2.8 shows the dependence of the H count rate on the electron energy. The red curve fitted into the data was derived from the Lotz formula for ionisation cross sections of atomic hydrogen [66, 67].

$$\sigma(E) = \left( aq \frac{\ln(E/P)}{E/P} (1 - be^{-c(E/P-1)}) \right) \quad (2.2)$$

$$Countrate = k\sigma(E) + d \quad (2.3)$$

with the factors  $a = 4.0$ ,  $b = 0.6$ ,  $c = 0.56$ , the threshold energy  $P = 13.6$  eV, and the charge  $q = 1$ , a given in  $10^{-14}$   $\text{cm}^2\text{eV}^2$ .  $k$  is a scaling factor and  $d$  an offset which were added as fitting parameters to the formula. An electron energy of 55 eV was found to be ideal for atomic hydrogen.

### 2.3.3 Extraction

A metal plate directly after the ionisation cage of the QMS is held on a negative potential which enables to accelerate the positively charged Ions, created by the electron bombardement, into the mass filter. This extraction potential has a big impact on light ions and especially protons. A scan for the parameter can be seen in figure 2.9. The potential was chosen to be set to  $-72$  V.

### 2.3.4 Ion energy

As figure 2.7 shows, the electric potential between the first plate and earth potential defines the ion energy. Changing this potential has an effect for the time of the ions in the mass filter. Lower ion energy leads to longer presence in the oscillating quadrupole field whereas higher ion energy means shorter interaction time with the mass filter. As a consequence of

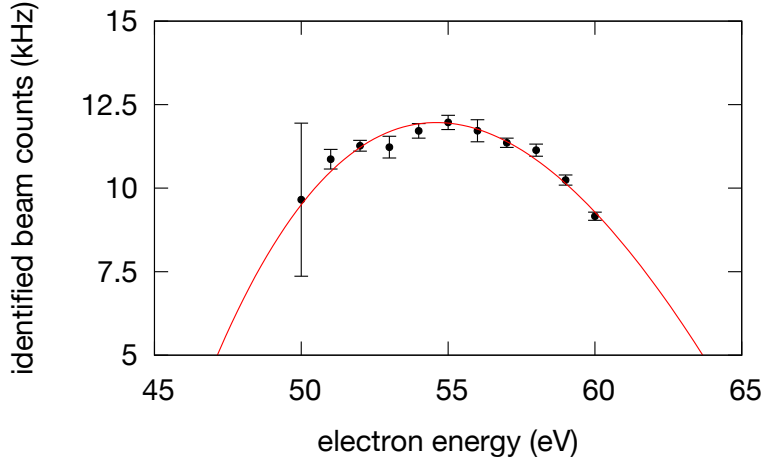


**Figure 2.8:** Plot of the beam counts detected with a digital lock-in amplifier vs. the energy of the electrons. The data is fitted (red curve) with an empirical formula for the electron impact ionisation cross section  $e^- + H \rightarrow p + e^- + e^-$  [66, 67]. The only fit parameters are a scaling factor and an offset to absorb a constant background rate.

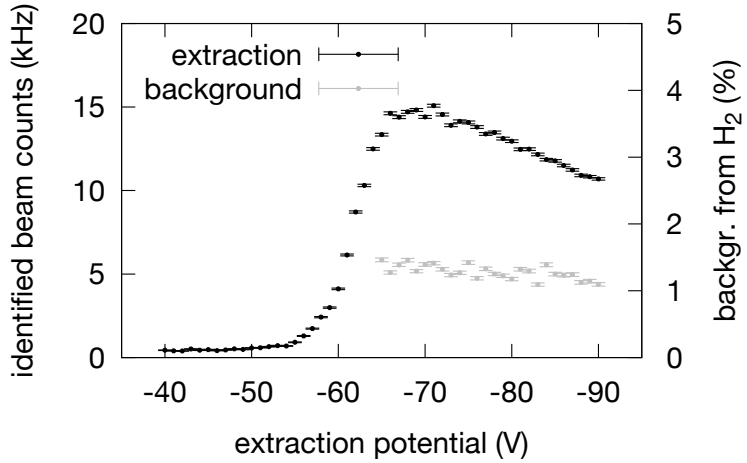


**Figure 2.9:** The extraction potential is the potential that attracts the ions out from the ionisation cage. As can be seen an optimum of the potential is around  $-72$  V. Care had to be taken that no big amount of background gas of molecular hydrogen in the beam would be wrongly identified as  $m/q = 1$ . As can be seen (grey error bars)  $H_2$  background is not contributing in big amounts to the signal. The  $H_2$  background was calculated from the hydrogen source turned off to source turned on ratio  $(\frac{m}{q} = 1)^{off}/(\frac{m}{q} = 1)^{on}$ . The  $H_2^{off}$  abundance was weighted by the cracking efficiency information.

this parameter the resolution of the  $m/q$  peak is increased (lower ion energy) or decreased (higher ion energy). Figure 2.10 shows the scan. The parameter was set to 6 eV.

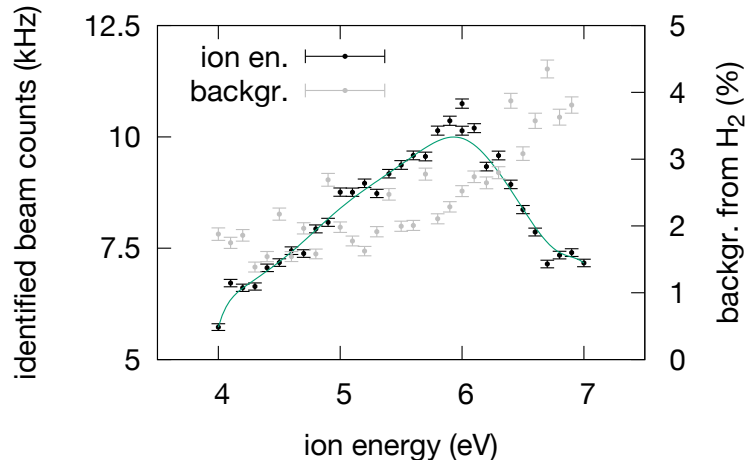


**Figure 2.10:** Plot of the optimisation of the ion energy. Ion energy defines the time of a particle in the mass filter, thus increasing/decreasing the resolution of the instrument. Increasing ion energy incremented also the fake mass 1 component from the background. Since the amount still was low the value was set to 6 eV. The green line was added to guide the eye.

### 2.3.5 Pole bias

Additionally another electrical potential - the pole bias - is a DC voltage on the QMS rods. A pole bias different from zero avoids that ions to hit the quadrupole rods during their oscillatory movement in the mass filter. This potential is also proportional to the resolution of the instrument. Consequently the pole bias is correlated to the ion energy. See figure 2.11 for the dependence of the count rate on pole bias. Typically the value was set to  $-4$  V.

### 2.3.6 $m/q$ scan

The alignment of the mass peaks with respect to the appropriate  $m/q$  was necessary. In ordinary QMS mass scans the whole residual gas at a certain  $m/q$  is measured. Therefore, the beam cannot be distinguished from background. The lock-in amplifier scheme allows to perform a mass scan where ionised beam atoms can be distinguished from ionised residual gas. Thus, the  $m/q$  peaks were centred with the MKS software to their appropriate peaks. After this procedure the peak position for hydrogen was at the correct place (figure 2.12).

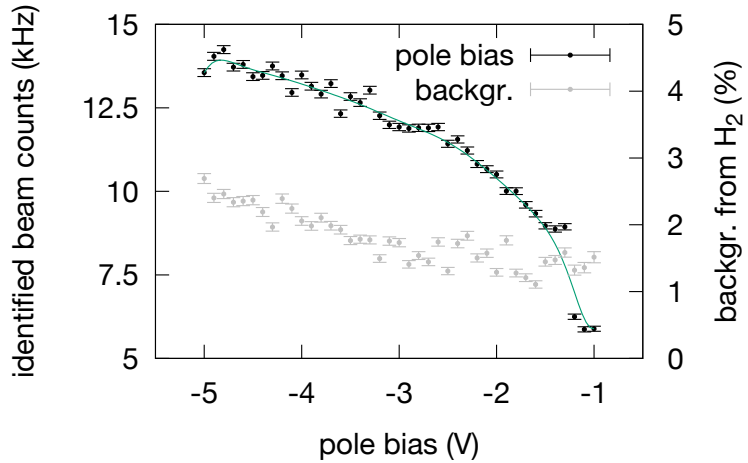


**Figure 2.11:** Measurement of the potential pole bias. The green line was added to guide the eye.

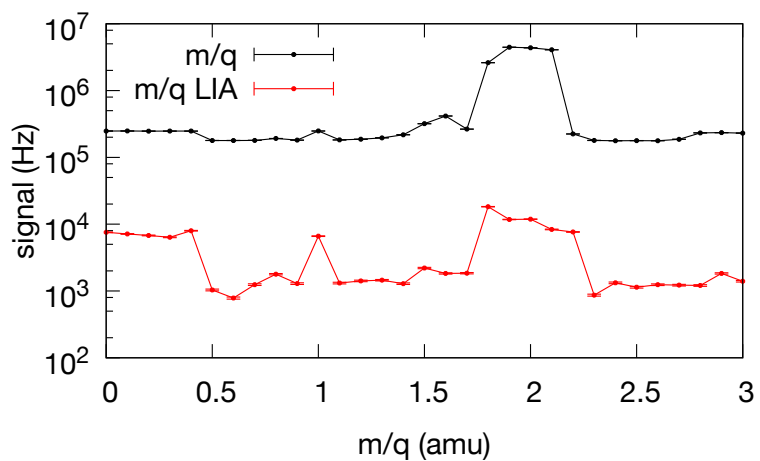


**Figure 2.12:** The plot shows the discrimination of background signals with the lock-in amplifier. Y-axis: on a logarithmic scale the counts of the detector can be seen. The red curve shows the lock-in amplifier signal of the beam, the black curve shows the total counting rate without the usage of the LIA. The  $m/q = 1$  peak is pronounced more when using the lock-in amplified signal.

### 2.3.7 SCEM saturation effect

In case of high counting rates the channeltron of the mass spectrometer suffered from saturation effects [68], i.e. the average height of single particle pulses was reduced. This reduction pushed the height of the peaks below the fixed discriminator threshold. As a consequence the increased event rate on the SCEM can lead to a reduction of the detected count rate and hence to a signal inversion. Especially for molecular hydrogen which was used to determine the cracking efficiency of the hydrogen source this behaviour was problematic. To overcome this issue for H<sub>2</sub>, the resolution of the instrument was increased by reducing the ion energy. This lowered the event rate to a regime where the detected count rate still grew linearly with the event rate (below 1 million counts/sec).

## 2.4 Background suppression

A challenge of a hydrogen beam experiment is the large amount of background, since hydrogen is an ubiquitous residual gas. One way to reduce unwanted signals was to have differentially pumped vacuum chambers similar to reference [69]. The beam could pass through apertures mounted on the separating walls. This way ultra high vacuum conditions could be reached in the detection chamber, although the pressure in the vacuum chamber, where the beam originates was about five orders of magnitude higher. Here the vacuum system was further supported by usage of a getter pump (SAES C 200-MK5 ST707) and two stage turbo molecular pumping. Turbo molecular pumps are more efficient for heavier residual gas components. The getter pump efficiently absorbs hydrogen and is therefore an important complementary and assisting pumping method for the hydrogen experiment. Before operating the hydrogen beam the base pressures in the last (QMS) chamber were below the sensitivity of the Bayard-Alpert type pressure gauges (ITR90: pressure  $< 5 \times 10^{-10}$  mbar)

For a further suppression of the background signal the beam was modulated and phase sensitive methods such as the usage of the lock-in amplifier were used to estimate the beam amount as was also initially done by the McCullough group [59].

### 2.4.1 Chopper

For the modulation of the beam a Scitec CH-10 tuning fork chopper with a duty cycle of 50 percent was installed.

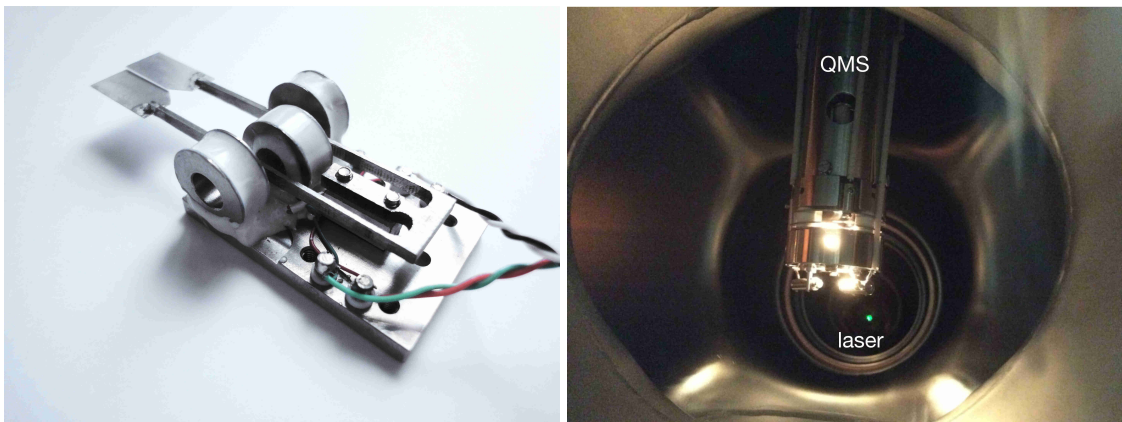


**Figure 2.13:** Left: photograph of the tuning fork chopper which modulated the beam. Right: photograph of the mass spectrometer. The QMS is mounted in a crossed beam configuration. The bottom part where the white light is visible is the ionisation source. The green light is coming from a laser which was aligned coaxially to the beam and therefore shining through the whole beam line during operation.

The advantages of such a tuning fork chopper are the frequency stability, UHV capability (just bending parts, no joints or bearings, therefore no grease, bakeable to 100 °C), small magnetic fields, adjustable amplitude, and direct output of reference signal for usage in the lock-in amplifier. The disadvantage of this type of chopper is the fixed frequency which for our case was approximately 178 Hz.

The chopper function (or also called response function) was recorded in parallel. A low power alignment laser at 532 nm was shining through the glass tube of the hydrogen source on the most upstream position. The signal was detected with a photodiode and bandpass filter for the green light at the most downstream side after the QMS and a vacuum window.

As the time delay for light is negligible (few ns) this measurement gave a real time information on the chopper opening (chopper function). The output of the chopper driver had some electronic delays which had to be corrected for when extracting the beam velocity from time of flight measurements.

## 2.5 Beam cooling

One of the requirements for the hydrogen experiment is a beam with a temperature of below 100 K as this is the expected range for the antihydrogen beam that will be provided within the ASACUSA-CUSP experiment. This property was achieved with the hydrogen beam by cooling the atoms to a desired temperature range with a cryocooler (DE-204SLB-A) and

a compressor (APD HC-4-MK2). On the coldhead two aluminium plates were mounted which were milled to fit a teflon tubing of 1.6 mm inner diameter in between. This PTFE tubing was attached to the orifice of the hydrogen source with a PTFE adapter on the one side and pointing onto a skimmer (which established the first differential pumping stage) on the other side. In the experiment two different cooling setups were used. For the first tests the hydrogen source was pointing straight in beam axis and the tubing also was attached straight. This first setup had the disadvantage that depending on the alignment of the coldhead a warm beam component was also present. Later, during the hyperfine structure measurements, this disadvantage was overcome by installing the hydrogen source perpendicular to the beam axis. With the attached PTFE tubing the cracking efficiency reduced to  $55 \pm 4\%$  for the straight source and  $33 \pm 5\%$  for the 90 degree source respectively which was nevertheless sufficient for the experiment. As can be seen in the next section the beam could be cooled to 22.4 K in the straight aligned setup.

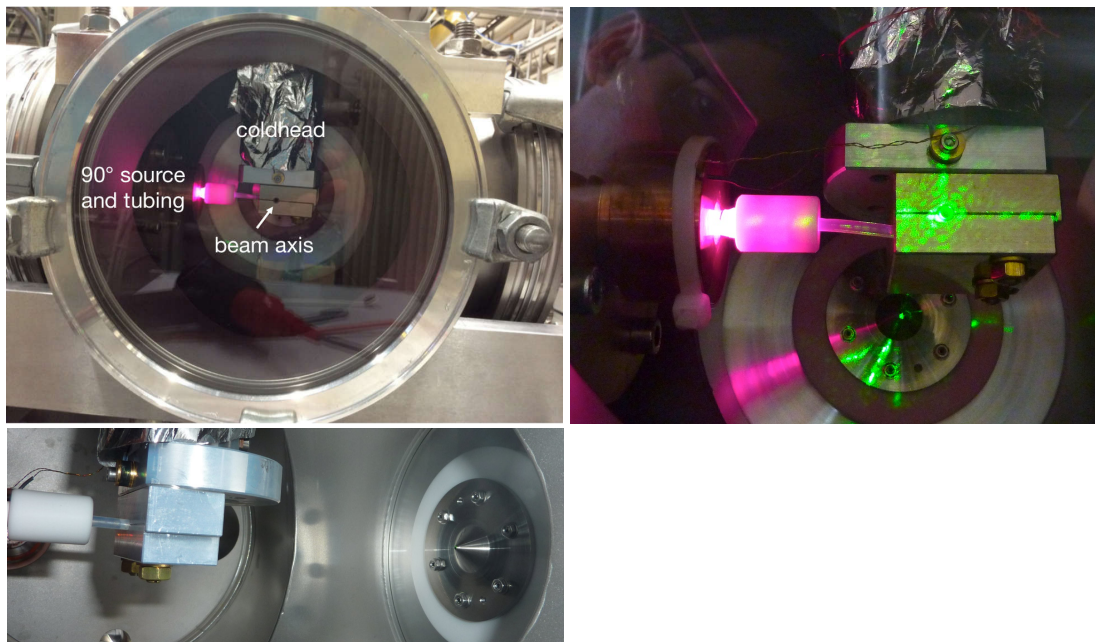


**Figure 2.14:** Top left: photograph of the hydrogen source mounted perpendicular to the beam axis. The teflon tubing was attached to the pyrex tube, fed into the aluminium block, cooled by a cryogenic system. Top right: bigger photograph of same configuration. A laser is shining through the tubing in beam direction onto the first aperture (skimmer). Bottom: photograph of the straight hydrogen source configuration where the hydrogen source is mounted in beam direction.

## 2.6 Time of flight

Time of flight (TOF) information was important for knowing the beam temperature and setting it to a desired value. The basic way how to retrieve this information is described comprehensively in a paper by J. Walraven [70]. In principle the measured modulated signal at the detector is a convolution of a Boltzmann distribution and the response function of the chopper acting on the beam.

$$S(t) = \int_{-\infty}^t e(\tau)h(t - \tau) = e(t) * h(t) \quad (2.4)$$

$$h(t) = \frac{4}{\sqrt{\pi}} \frac{1}{\theta} \left( \frac{\theta}{t} \right)^4 e^{-(\theta/t)^2} \quad (2.5)$$

where  $t$  is time,  $S(t)$  is the measured signal,  $e(t)$  the response function of the chopper,  $h(t)$  a Boltzmann function weighted with a  $v^{-1}$  dependence for the sensitivity of quadrupole mass spectrometers,  $\theta = L/v$  the TOF,  $L$  the distance chopper - detector, with the velocity  $v$  of the atoms [70].

In our case the response function simply was the positive part of a sine (zero if negative) with a flat top depending on the amplitude of the chopper modulation. The reason for this shape is that the beam could be bigger than the chopper amplitude. Figure 2.15 illustrates the shape of the response function

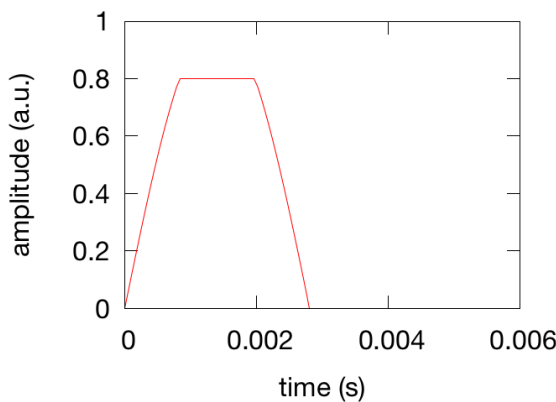


**Figure 2.15:** Illustration of the chopper response function. Depending on the chopper opening the flat top will be at a different amplitude.

Having the chopper signal as a starting time and the arriving signal as stop one can extract the TOF. The convoluted function of the response function with the Boltzmann

distribution then can be fitted into the detected signal and the temperature can be extracted. Figure 2.16 shows typical detector signals fitted with the convoluted function for a room temperature beam and a cold beam. For the measurement of these data no polarising magnets were installed in the beam line. The coldest achieved beam temperature was 22.4 K for a coldhead temperature  $T_c$  of 20.9 K.

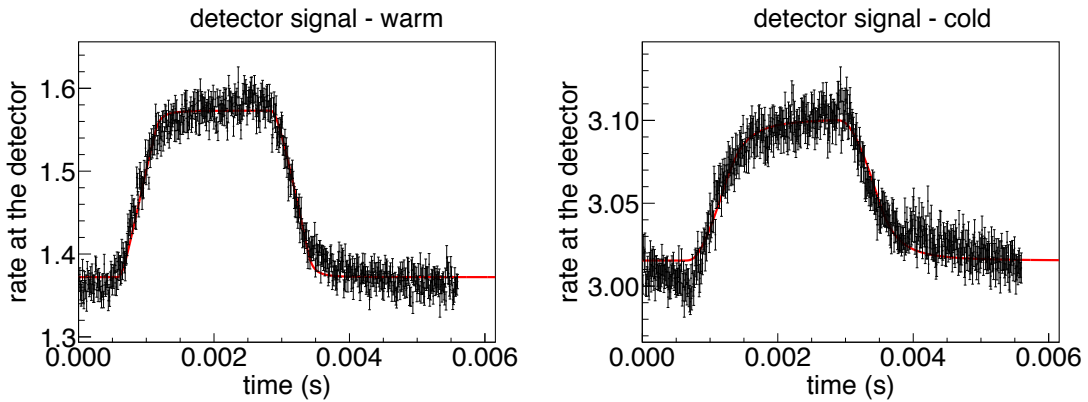


**Figure 2.16:** Boltzmann type TOF spectra. Here no polarising magnets were installed in the beam line. Left: the detector signals for a warm beam; right: cold beam. Red lines shows the fit with function 2.4. The flight path for the short setup was 50 cm. left: temperature fit  $T_{fit} = 295.3 \pm 18.9$  K, red.  $\chi^2 = 1.6$ , temperature coldhead  $T_c = 294.4$  K; right:  $T_{fit} = 22.4 \pm 0.8$  K, red.  $\chi^2 = 1.4$ ,  $T_c = 20.9$  K;

Another way to extract the velocity was by using the phase information of the lock-in amplifier. The LIA signal had a phase difference with respect to the chopper signal. This information also yielded similar results for the flight time as the fit.

## 2.7 Polarisation

A Rabi-like experiment exploits the possibility to spatially separate spin-states by magnetic field gradients. The first step is to generate a polarised beam. In the case of the hydrogen beam experiment the polarisation was performed by a set of two permanent sextupole magnets. The design and the construction were done by the CERN magnet group [71]. The sextupoles magnetic field was about 1.4 T at the poles, the length was 65 mm, and the inner diameter was 1 cm. The magnetic alloy consisted of  $\text{Sm}_2\text{Co}_{17}$  and the support was made out of titanium.

The reason for using two magnets instead of a single one is illustrated in figure 2.18. With two magnets and an aperture with 3 mm diameter in the middle, a narrow velocity band can be cut out of the broader Boltzmann distribution. Simulations showed that after

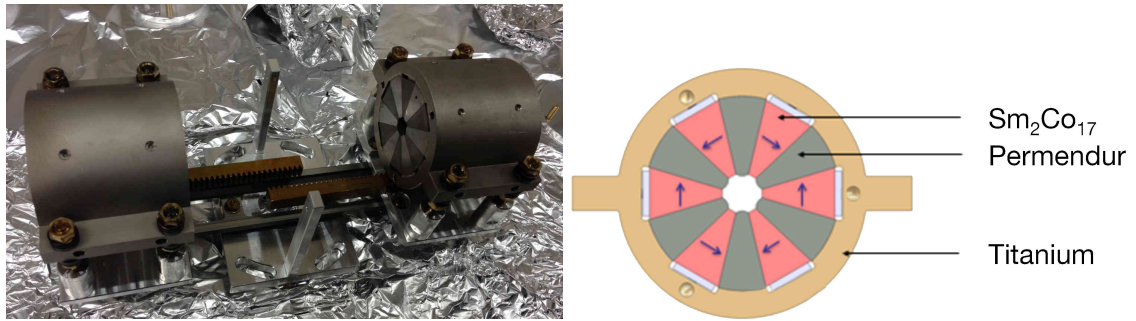


**Figure 2.17:** Left: picture of the permanent sextupole magnets mounted on a moveable manipulator. A gear wheel mounted on a vacuum rotation feedthrough enables the change of the distance between the magnets from outside of the vacuum chamber. Right: Schematic drawing of the permanent sextupole magnets. The magnetisation of the individual sections is indicated by the arrows. A Fe-Co alloy type Vanadium Permendur separates the magnetic poles (drawing from CERN magnet group [71])

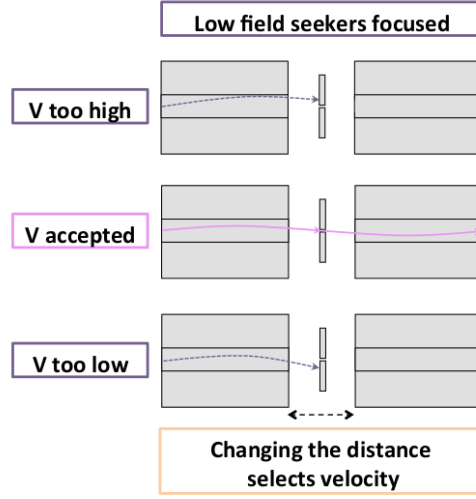
passing the magnets the beam should have a gaussian like, almost mono-energetic velocity distribution, and that it is effectively completely polarised ( $99.2^{+0.8}_{-8}$  percent [72]). The velocity of the cut out beam should only depend on the distance between the permanent sextupole magnets and not of the initial temperature, which can be controlled via the coldhead temperature.

Figure 2.19 shows a simulation of the velocity acceptance of the two permanent sextupole magnets depending on the distance between each other. The simulated particle number is 1e6, the beam starts at the entrance of the skimmer with a divergence of 5 degree opening angle. The velocity distribution of the simulated particles is a 50 K Boltzmann distribution. The detector was placed at the position of the QMS with a diameter of 3 mm. Only low field seekers have been simulated. When closer the magnets favour slower beam, whereas when the distance is higher the magnets favour a faster beam.

## 2.8 Modified fitting function

Fitting the detector signals of the polarised beam, i.e. with the permanent sextupole doublet installed, made an adjustment of the fitting function necessary. Since instead of a Boltzmann distributed beam the gas was gaussian like distributed, the ansatz for the convolution was:

$$S(t) = h_1(t) * e(t) = e^{-(\frac{L}{t} - \mu)^2 / (2\sigma^2)} * e(t) \quad (2.6)$$



**Figure 2.18:** Principle of the velocity acceptance of the permanent sextupole magnets. Depending on the distance between the magnets different velocities are accepted. Through the hole with an aperture diameter of 3 mm a beam with a gaussian distributed velocity will pass and therefore, after the sextupole magnets the beam will be almost mono-energetic.

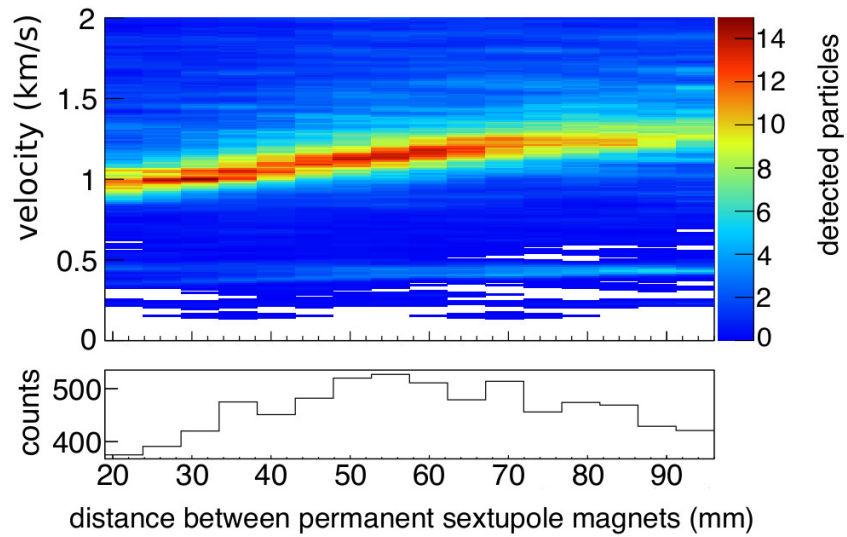


**Figure 2.19:** Simulation of the velocity acceptance of the permanent sextupole magnets depending on the distance between each other ( $d_{ss}$ ). The colour indicates the amount of particles being detected by the detector. When the magnets are closer, a slower beam is favoured to pass to the detector, when more distant a faster beam is favoured. The bottom histogram shows a projection of the events for a every distance between the permanent sextupole magnets (simulated by C. Sauerzopf).

with  $h_1(t)$  the gaussian distribution,  $L$  the distance chopper to detector,  $\mu$  and  $\sigma$  the mean velocity of the beam and standard deviation of the gaussian distribution. Figure 2.20 shows the fit of function 2.6. For these data the 90 degree hydrogen source was used. The data was recorded with the full spectrometer inserted in the beam line. Additionally the superconducting sextupole magnet was used since the magnet focuses the atoms and therefore increases the count rate. The fully assembled beam line will be explained in the next chapter.

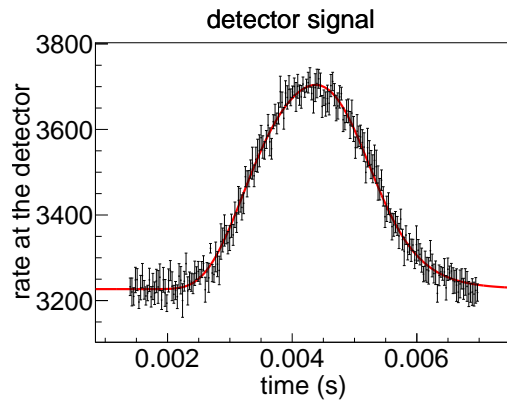


**Figure 2.20:** Detector signal with new fit routine. The polarising sextupole magnets were installed for these data. A gaussian like velocity convoluted with the chopper function was fitted into the data. During the data taking the superconducting sextupole had a maximum pole field of 3.5 T. The distance to the chopper was 2.8 m.  $v = 885(4)$  m/s,  $\sigma = 130(6)$  m/s,  $\chi^2 = 0.8$ .

In the straight hydrogen source configuration a warm beam component was present. Therefore, for these data an additional Boltzmann component as mentioned in section 2.6 was added as fitting parameter. The fit of the straight hydrogen source data yielded a warm beam component with roughly  $20 \pm 5\%$ .

# 3 Hyperfine spectrometer apparatus

For all the following experiments the fully assembled apparatus was used, as described below. Figure 3.1 shows a technical drawing for the hydrogen beam line. The convention in the graphs will be: the Z axis points from upstream to downstream, the X axis goes horizontally, and the Y axis goes vertically. In comparison to the aforementioned setup the spin flip cavity including Helmholtz coils, mu metal shielding, and the superconducting sextupole magnet were inserted between source (chopper) and detector. Figure 3.2 shows photographs of the complete setup.

## 3.1 Cavity

The central component of a Rabi-type experiment is the oscillating magnetic field, which induces the spin-flips. In the case of ASACUSA's (anti)-hydrogen hyperfine splitting experiment this field shall be provided by a microwave cavity. The requirement of a trajectory independent oscillating field strength over a large area lead to the choice of strip line type resonator. The cavity, a magnetic shielding and, Helmholtz coils were designed and constructed by S. Federmann. Technical details can be found in her Ph.D. thesis [73, 74]. See figure 3.3 for a photograph and a drawing of the cavity.

The main idea of this microwave resonator is to have a standing wave of the oscillating microwaves at 1.42 GHz for achieving large amplitudes, which are needed for the comparatively short interaction times of an in-beam experiment. The main advantage of such a design is that little power is needed from the microwave system. The microwave field was chosen to be perpendicular to beam axis (see figure 3.4). This design property avoids doppler shift broadening in the resonance line shape. Since Maxwell's equations forbid for dimensions larger than the half wavelength of the RF field to have a perfect homogeneity in all directions of space, the oscillating magnetic field was designed to be cosine distributed in beam direction. In the xy plane the field homogeneity is  $\pm 2\%$ . To prevent a leakage of

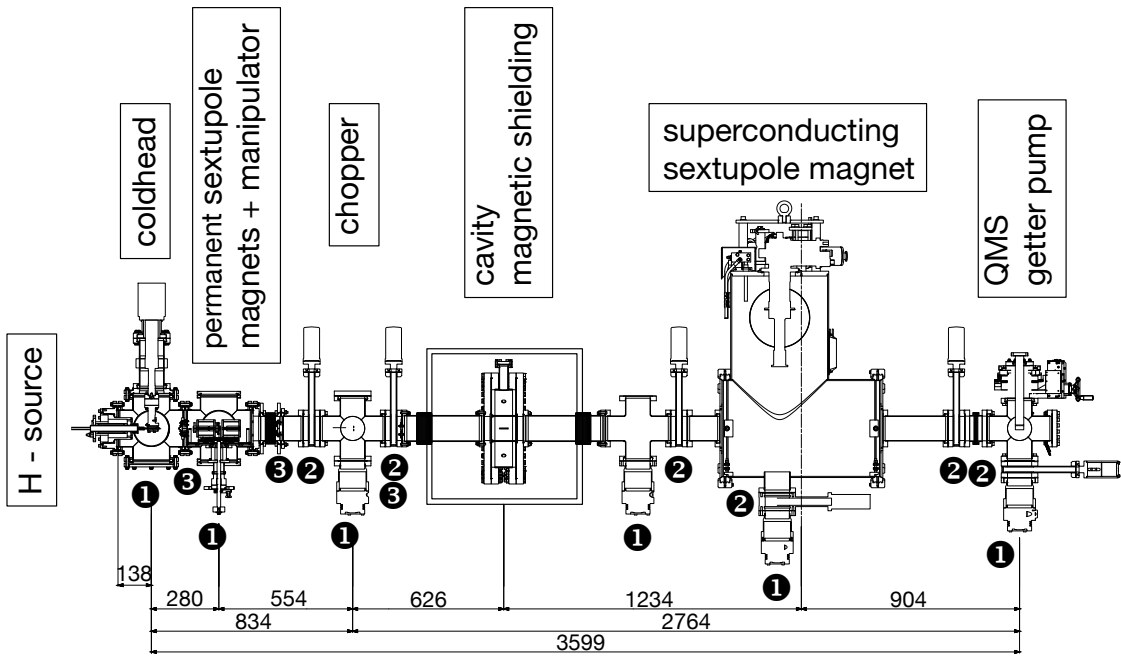


**Figure 3.1:** Technical drawing (dimensions in mm) of the complete Rabi-like setup (beam direction / beam propagation direction left to right). H-source - hydrogen produced in a plasma, coldhead - beam pre cooled, permanent magnets - polarised and velocity component selected, chopper - modulates the beam, cavity and magnetic shielding - spin flips are induced and external magnetic fields are blocked away, Helmholtz coils (not shown in the figure) are installed, which define the static magnetic field, superconducting sextupole magnet - analyses the beam by sorting out high field seeking state, and the QMS as detector. ① shows sections where turbo molecular pumps are installed, at ② gate valves are placed, and at ③ the skimmer and apertures are placed. 8 pressure sensors are distributed over the setup (H<sub>2</sub> supply, coldhead, permanent sextupoles, chopper, cavity, superconducting sextupole, QMS, getter pump)

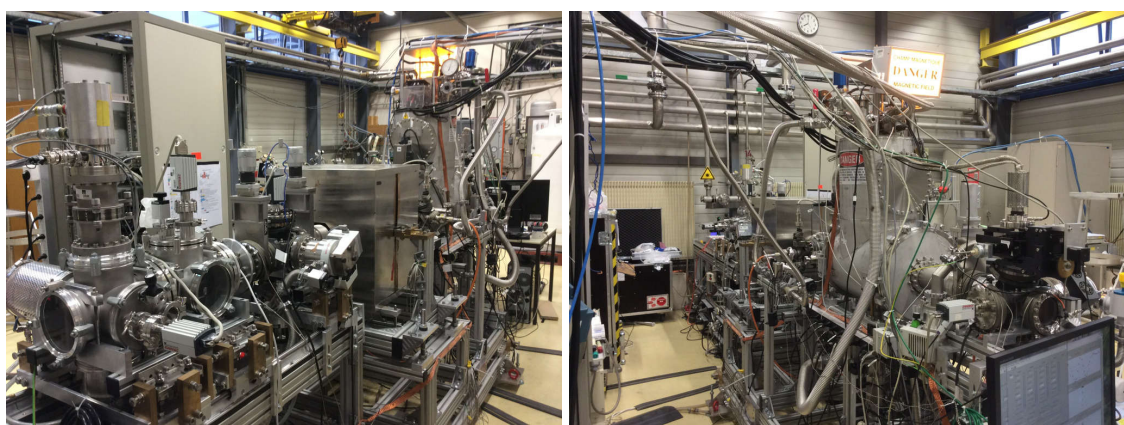


**Figure 3.2:** Photographs of the complete setup; left: downstream view; right: upstream view

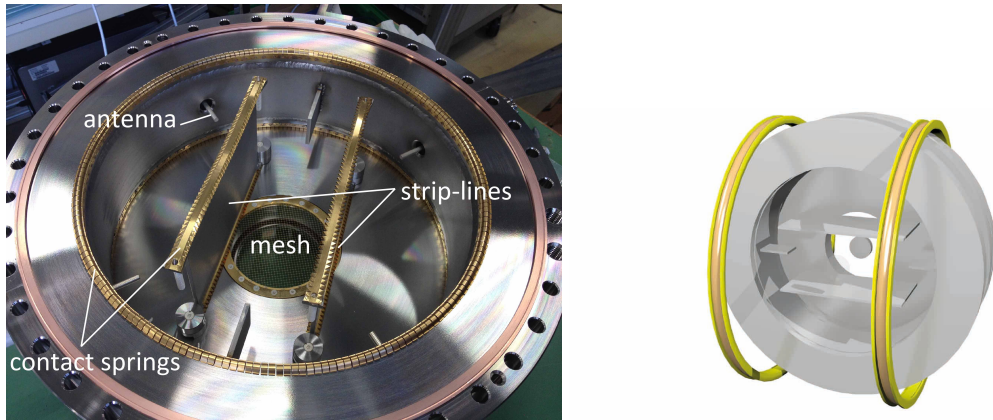


**Figure 3.3:** Left: photograph of the spin flip cavity. The antennas transmit the microwaves into the cavity, the gold plated Copper Beryllium contact springs ensure an RF contact between the cavity parts, the gold meshes electrically close the cavity, the wings suppress unwanted modes and the strip lines define the homogeneous standing wave of the RF mode in the cavity. Right: drawing of the cavity surrounded by Helmholtz coils (drawing from Bernadette Kolbinger [37])

the microwaves from the resonator into the beam pipes a gold coated mesh was attached at the entrance and exit. The meshes have a transparency for the atoms of 96 %. The cavity Q-factor is approximately 200.

The field distribution yields a special transition line shape characteristic for this cavity. The spin-flip probability as a function of the detuning frequency at every point in the cavity during passage of the (anti)-hydrogen atom is shown in fig. 3.5. This plot is obtained by solving the optical Bloch equation and was generated by Clemens Sauerzopf [76]. When on resonance (detuning = 0) the population of the second state increases over the first half of the cavity, however, in the second half the exactly opposite field exactly compensates the effect of the first half, thereby restoring the initial state. This is true for any beam velocity. A certain detune is necessary to end up with a net-effect [56].

For a back-of-the-envelope calculation of the detuning required for an efficient spin-flip drive one can interpret the inversion of the direction of the oscillating magnetic field along the beam direction as a  $\pi$ -phase-shift. Therefore, the magnetic field effectively stays on resonance if the detune leads to a  $\pi$ -phase-shift between the resonance frequency and the microwave field frequency over the time of passage through the cavity:

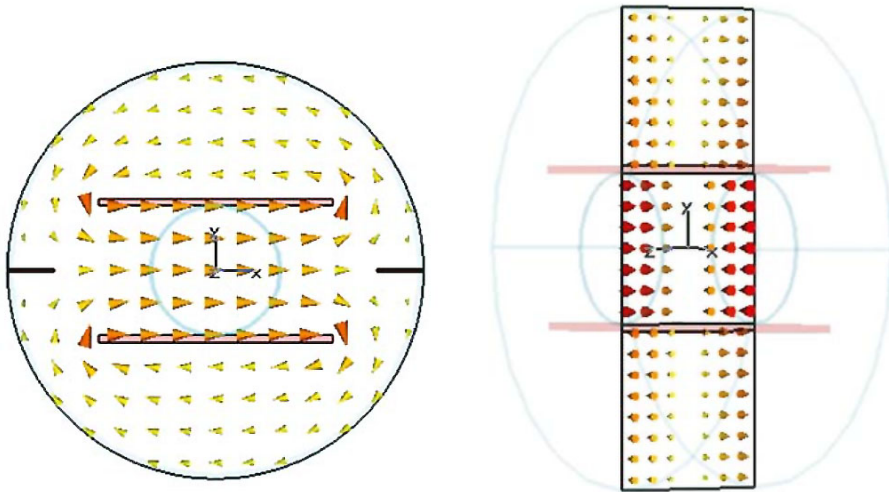


**Figure 3.4:** Field distribution of the RF field inside the cavity. Left: in beam direction, the field is perpendicular to the beam propagation direction (z direction) and homogeneous in the beam region (inner blue circle). Right: Drawing sideways to the beam direction. The RF field is changing in magnitude, having a maximum at the left side mesh, in the centre the RF field is zero, then towards the other cavity wall increases to the initial maximal value again. (from [75])

$$\Delta_{\text{detune}} = \nu_{\text{drive}} - \nu_c \quad (3.1)$$

$$\tau_{\text{int}} = l_{\text{cav}} / v \quad (3.2)$$

$$2\pi\Delta_{\text{detune}}\tau_{\text{int}} \approx \pi \quad (3.3)$$

$$\Delta_{\text{detune}} \approx \frac{1}{2\tau_{\text{int}}} \approx 0.5 \times 1000 \text{ m s}^{-1} / 0.1 \text{ m} \approx 5 \text{ kHz}, \quad (3.4)$$

with  $\Delta_{\text{detune}}$  the offset frequency of one of the side lobes w.r.t. the centre of the resonance curve,  $\nu_{\text{drive}}$  the frequency at the highest state population density (side lobe of the resonance curve),  $\nu_c$  the frequency in the centre of the resonance line (between the two lobes),  $\tau$  the time a particle spends in the cavity,  $l_{\text{cav}}$  the cavity length, and  $v$  the velocity of the atoms.

### 3.1.1 Description of the cavity and the RF system

In the work of S. Federmann it was proposed to feed in microwaves from two opposite antennas using a 180 degree hybrid for in-phase excitation. However, a vector network analyser showed that the antennas had slightly different electrical lengths so that the waves did not interfere positively. To overcome this problem the cavity was excited by one port only as illustrated in figure 3.6. Furthermore, the contact springs which enable the RF

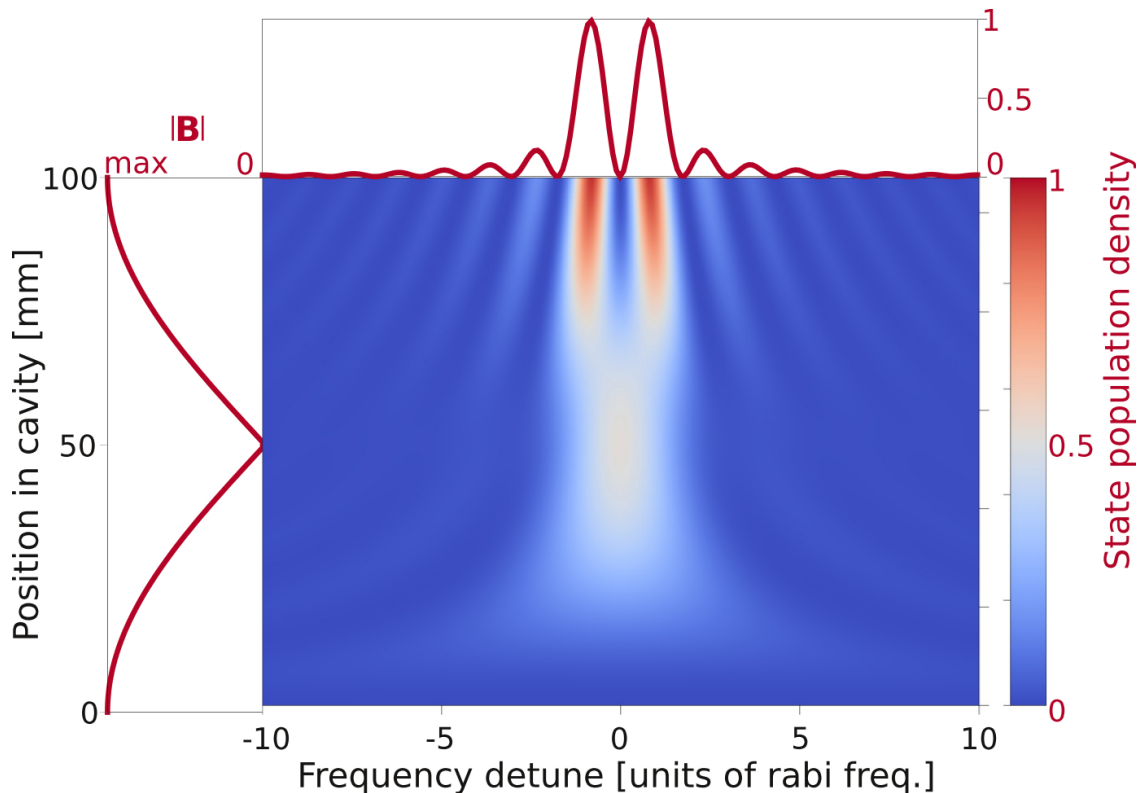


**Figure 3.5:** Explanation of the resonance line shape. Y axis shows the Z position in the cavity, X axis shows the frequency detune of the microwaves in the cavity in units of Rabi frequency, the colour shows the state population (blue initial state, red spin flipped to other state). The shown situation applies to a mono-energetic beam and a microwave power adjusted to yield a  $\pi$ -pulse (see section 4.3). On the left side outside of the plot the cosine like absolute value of the magnitude of the oscillating magnetic field of the microwave field is plotted in z direction. On top of the plot there is a projection of the spin flip probability when leaving the cavity depending on the frequency detune. At zero detune no net effect in state population can be observed, whereas if slightly detuned spin flips can occur. [77].

contact between the cavity flanges and the cavity body did not reliably stay in position and consequently did not yield the optimal RF contact. Therefore, less power could be transmitted into the system. Nevertheless, hyperfine transitions could be measured. However, this situation was unacceptable especially for later antihydrogen experiments as reliability and reproducibility are absolutely crucial. The solution was spot welding the contact springs onto the cavity. Additionally a stub tuner was installed for a better impedance matching. After these steps more power could be fed into the system (see section 5.3.4 for more details).

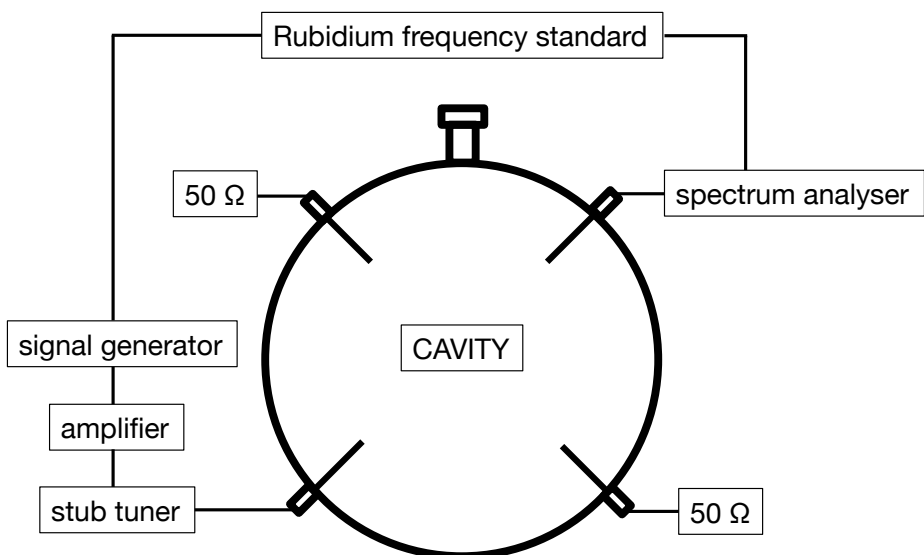


**Figure 3.6:** Exciting scheme of the microwave field in the cavity. One antenna port instead of in phase excitation with two opposite ports excites the RF field. The microwaves are produced in a signal generator which is locked to a rubidium frequency standard, then the signal is amplified, a stub tuner couples the microwaves into the cavity via an antenna. At another port a spectrum analyser, also using the rubidium standard as clock, picks up the signal and measures the power. The two remaining ports were terminated with 50 Ohm resistors.

A signal generator (synthesiser) - Rohde & Schwarz SML02 provided the microwaves with a desired frequency and power. A Mini Circuits ZHL-10W-2G(+) amplifier with a maximum output power of 10 W amplified the signal by 40 dB. The stub tuner matched the

impedance of the antenna with the amplifier. From a second port an Agilent Technologies N9010A spectrum analyser picked up the signal and recorded the power as a function of the frequency. A SRS FS725 rubidium frequency standard served for frequency stabilisation for both, the signal generator and the spectrum analyser.

### 3.1.2 Magnetic shielding

The external magnetic field in the cavity volume, where spin flips are driven, has to be adjustable and uniform in order to control the Zeeman shifts and avoid broadening caused by them. In the antihydrogen experiment high residual magnetic fields coming from the cusp trap (up to 30 G) and the superconducting sextupole (up to 10 G) have to be expected. Therefore, the spin-flip cavity is surrounded by a magnetic shielding. The chosen design has cuboid shape with two layers of  $\mu$ -metal. The inner layer shielding was provided by Magnetic Shields Ltd with the dimensions  $531 \times 531 \times 606$  mm. The outer layer was produced by Ohtama Co., Ltd with dimensions  $561 \times 561 \times 636$  mm. For the recorded data the shielding is less critical compared to the antihydrogen experiment, since in the hydrogen experiments only the earth magnetic field and the field of the superconducting sextupole magnet needed to be blocked away.

### 3.1.3 Static magnetic field

A measurement of the hyperfine transition at zero magnetic field is problematic, as Majorana spin-flips might occur [78]. Therefore, a guiding field is required. However, due to the Zeeman effect this leads to a shift of the hyperfine transition frequency as depicted in the Breit-Rabi diagram (figure 1.4). The guiding field has to be well known. For this experiment Helmholtz coils were used to generate a static magnetic field. The coils had 90 windings with a 1.6 mm diameter copper wire and a radius of 235 mm. The distance between the two coils was  $214 \pm 1$  mm. The current for the coils was delivered by a Heinzinger PTNhp 32-10 power supply with a stability of  $\leq 0.02\%$  over eight hours. The current could be varied between 0 and 1 A comparable to a magnetic field of a few gauss. The corresponding magnetic field was determined precisely in the course of this work from the measured resonance data and can be found in the result section (figure 5.48).

Two fluxgate sensors (Bartington Mag-03IE1000 read with Bartington Decaport) were installed on the cavity to watch the magnetic field inside the shielding and to get values for the magnetic field and the Zeeman splitting. The sensors were mounted approximately 20 cm from the centre of the cavity but only  $\approx 10$  cm away from the beam axis. Sensor 1

was located on the upstream side of the cavity and sensor 2 on the downstream side. On each of the fluxgates a Pt100 temperature sensor was attached. In parallel the current in the Helmholtz coils was measured with a Keithley 2001 multimeter. Since both fluxgate devices had an offset in some of their components the main instrument for measuring / defining the Zeeman splitting was the current in the Helmholtz coils, monitored with the Keithley multimeter ( $7\frac{1}{2}$  digits resolution). Figure 3.7 shows the sensor readings depending on the current in the Helmholtz coils.

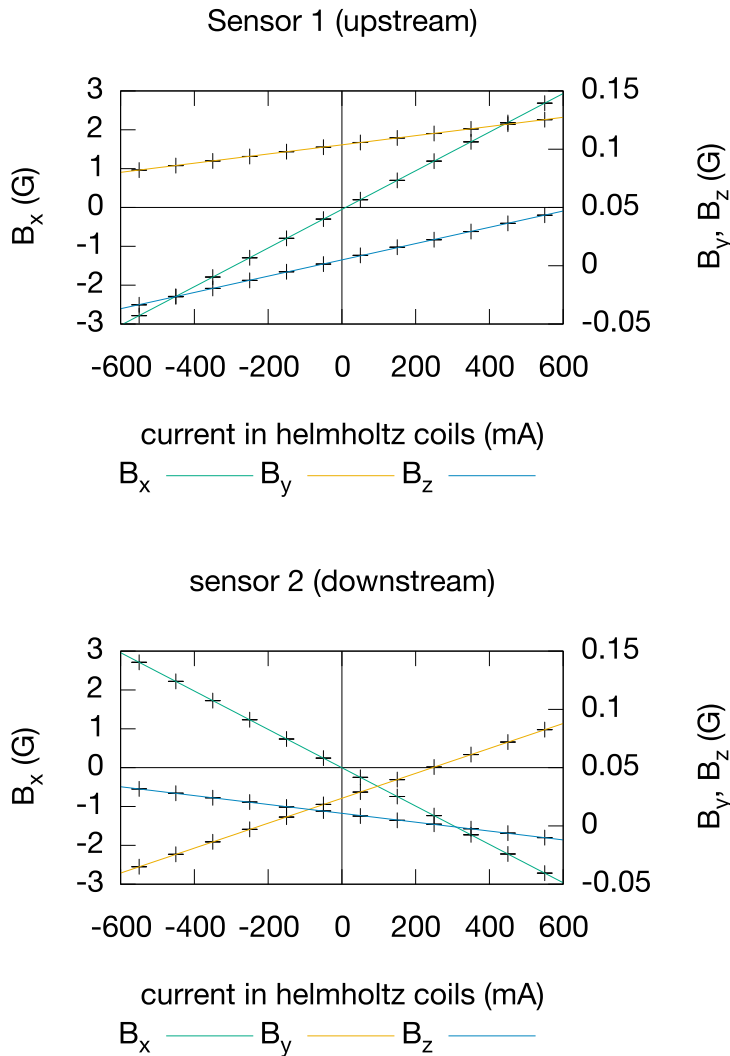


**Figure 3.7:** Offset of the flux gate sensors. Note the different Y axis for  $B_x$  and  $B_y, B_z$ . A linear fit  $y = kx + d$  yielded the slope and the zero offset

$$\begin{aligned}
 B_{x1}: k &= 4.97(1) \times 10^{-3} \text{ GmA}^{-1} & d &= -0.0500(3) \text{ G}, \\
 B_{y1}: k &= 3.940(8) \times 10^{-5} \text{ GmA}^{-1} & d &= 0.10374(2) \text{ G}, \\
 B_{z1}: k &= 6.98(2) \times 10^{-5} \text{ GmA}^{-1} & d &= 0.00503(6) \text{ G}, \\
 B_{x2}: k &= -4.934(1) \times 10^{-3} \text{ GmA}^{-1} & d &= -0.0015(3) \text{ G}, \\
 B_{y2}: k &= 1.0696(8) \times 10^{-4} \text{ GmA}^{-1} & d &= 0.02373(2) \text{ G}, \\
 B_{z2}: k &= -3.80(2) \times 10^{-5} \text{ GmA}^{-1} & d &= 0.01081(6) \text{ G}.
 \end{aligned}$$

## 3.2 Superconducting sextupole magnet

In the antihydrogen experiment a superconducting magnet will be used to spin-analyse the beam coming from the cusp trap and through the spin-flip cavity. It has the role of the second Stern Gerlach type magnet in a Rabi setup. Therefore, it was essential to check if the instrument works as specified by the manufacturer and to specify it further. Figure 3.8 shows a photograph of the superconducting magnet.

The magnet, supplied by the company Tesla, can be ramped up to a pole strength of 3.5 T at the maximum radius of the CF-100 beam pipe corresponding to 400 A maximum current. The overall integrated gradient is 150 T/m. The effective length is 22 cm (full width at half maximum).

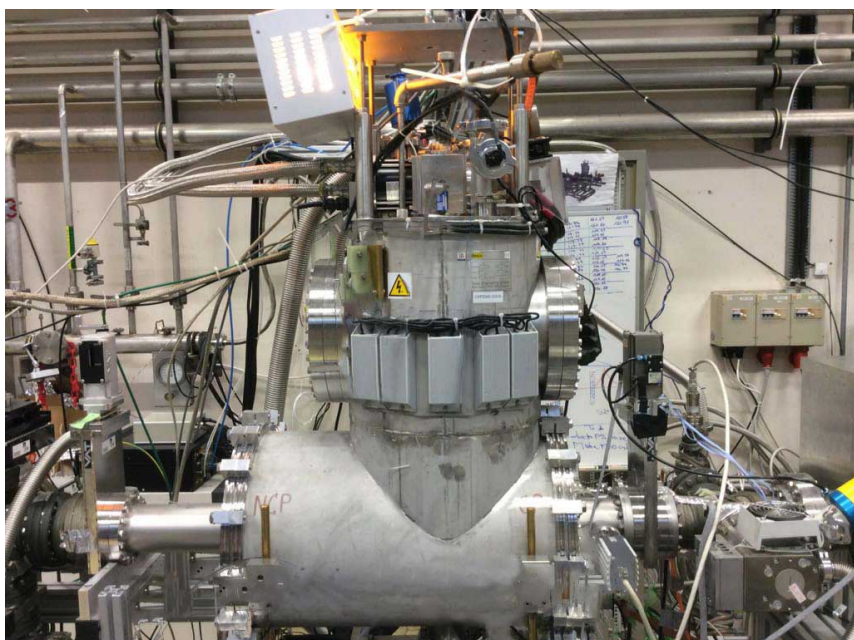


**Figure 3.8:** Picture of the superconducting sextupole magnet.

Figure 3.9 shows a simulation of the velocity acceptance of the superconducting sextupole magnet for the hydrogen beam line. For the simulation the particle number is 1e6, the beam opening is straight and not divergent starting at the superconducting sextupole, only low field seekers are simulated, and the velocity distribution is flat. The detector is set at the place of the QMS with a diameter of 3 mm. The maximum velocity accepted by the superconducting sextupole is approximately 1500 m/s.

The first experimental tests were done by increasing the current to the maximum and measure the velocities and the beam rate. Figure 3.10 shows the detected beam rate

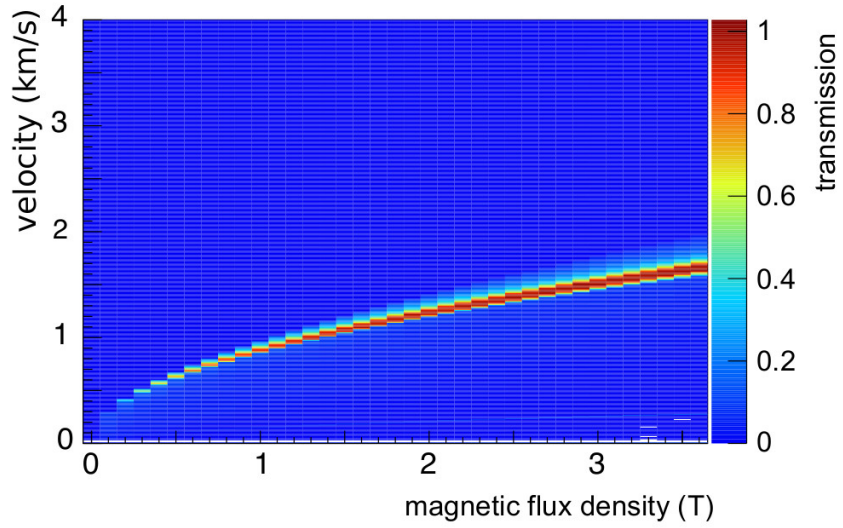


**Figure 3.9:** Simulation of the velocity acceptance of the superconducting sextupole magnet depending on the magnetic flux density (simulated by C. Sauerzopf).

during ramps from 0 to 400 A for various distances  $d_{ss}$  between the polarising permanent sextupole magnets. These sextupole ramps were measured with the perpendicular hydrogen source.

The plot shows that starting at a field of about 1.5 T the focussing effect becomes strong enough to increase the rate at the detector. The slope and shape of the following rate increase depends on the distance between the small polarising permanent magnets. The setting with the shorter distances  $d_{ss}$ , which correspond to the selection of a slower beam component, indicates over focusing, resulting in a drop of rate at the highest superconducting sextupole currents.

During a ramp of the superconducting sextupole current also the velocities, extracted by the first order phase information of the LIA signal, were investigated. Figure 3.11 shows again for the different permanent sextupole distances the change in velocities. The velocity is decreasing and at the over focusing point increasing again. At 0 A in the superconducting sextupole the velocities are higher. The most likely explanation is that the velocity distribution is broader, during the ramp a velocity component is focused onto the detector and thus, the average velocity drops. Phenomenologically the behaviour of the permanent sextupole magnets seems to fit to the simulations presented in figure 2.19. When the permanent sextupoles are closer the beam is slower and when  $d_{ss}$  is higher a

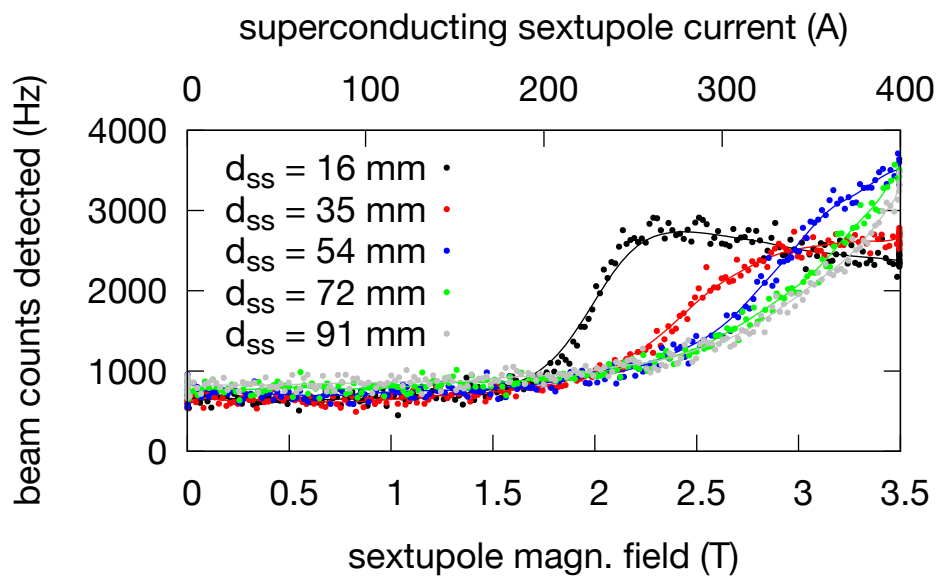


**Figure 3.10:** Beam rate (background subtracted) measured at various permanent sextupole distances during ramps of the superconducting sextupole magnet. The curves are Bezier spline interpolated to better highlight the slopes. It can be seen that for different settings at the permanent sextupoles, the superconducting sextupole current setting of optimal focusing is changing. When the permanent sextupoles are closer and select a lower velocity component the superconducting sextupole has its best focusing already at lower magnetic fields.

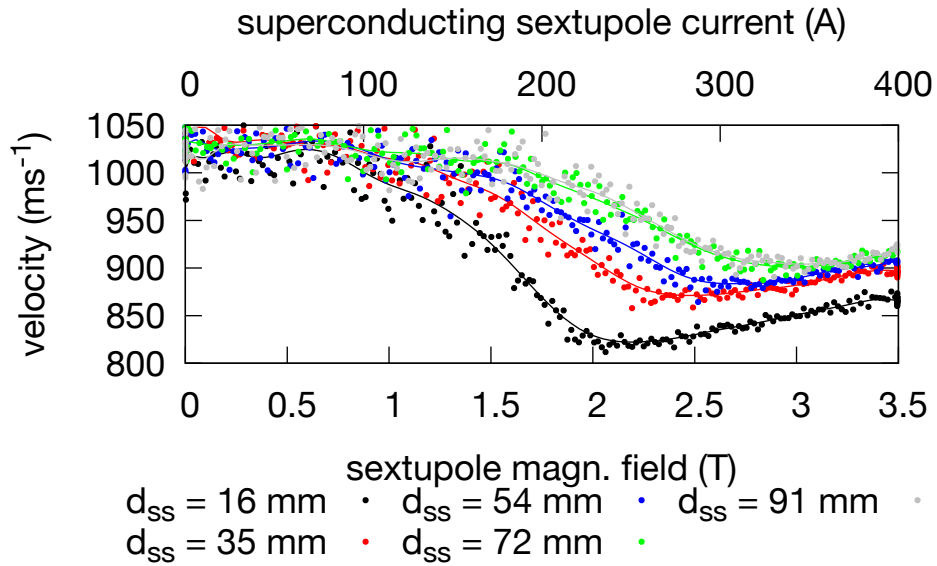


**Figure 3.11:** Velocity measured during superconducting sextupole ramps. The curves are Bezier spline interpolated to better highlight the slopes. The curves show that when the permanent sextupole magnets are closer they favour slower components. At the same time the focal point of the superconducting is moving towards smaller field strengths for slower beams. (Also shown in the plot 3.10).

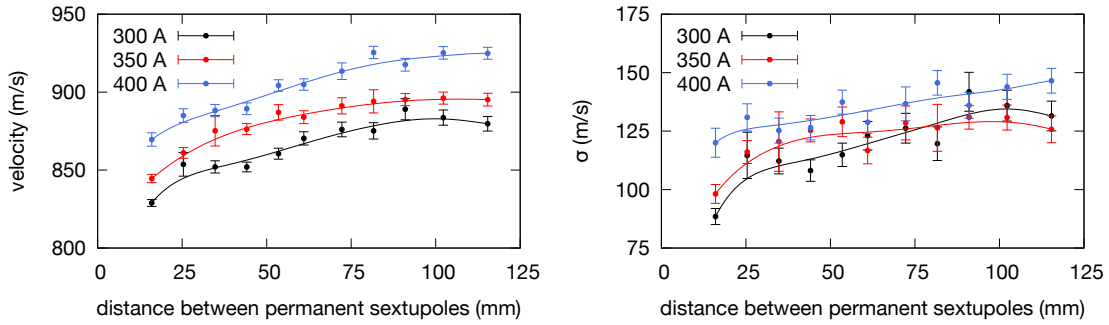
faster beam is favoured. Apparently the velocity acceptance in the experiment starts at a slower beam than shown in the simulations.

Figure 3.12 presents the dependence of the velocity and the width of the velocity distribution on the distance between the permanent sextupole magnets by using the information from time of flight fits for 300, 350 and 400 A.

The mass spectrometer was mounted on an XY-moveable manipulator (McAllister Technical Services, Inc.) which enabled to align the detector and for taking two dimensional profiles of the beam. In figure 3.13 the focusing is once more demonstrated. For the 0 A scan the beam is broader and almost cannot be seen. At 400 A ( $\cong 3.5 \text{ T}$ ) the beam can be clearly distinguished from background signals. Looking at the velocity (again taken from the LIA phase information), the centre spot is colder which is a result of colder components being focused.

Figures 3.14 and 3.15 show the focusing effect for various distances between the permanent sextupoles. As also shown before in figures 3.10 and 3.11, higher  $d_{ss}$  result in a more dense beam.

Next the figures 3.16 and 3.17 show cuts in the x- and y-direction for the beam count rate and the velocity for a sextupole current of 400 A (extracted from TOF fits). One



**Figure 3.12:** Velocity and  $\sigma_v$  (width of gaussian velocity) for 300 A, 350 A, and 400 A in the superconducting sextupole magnet as extracted from TOF fits. Left: bigger permanent sextupole distances favour higher velocities, due to different focusing of the superconducting sextupole magnet the individual curves have a different velocity. Right:  $\sigma_v$  of the gaussian velocity (The graphs were Bezier interpolated to better distinguish between the settings).

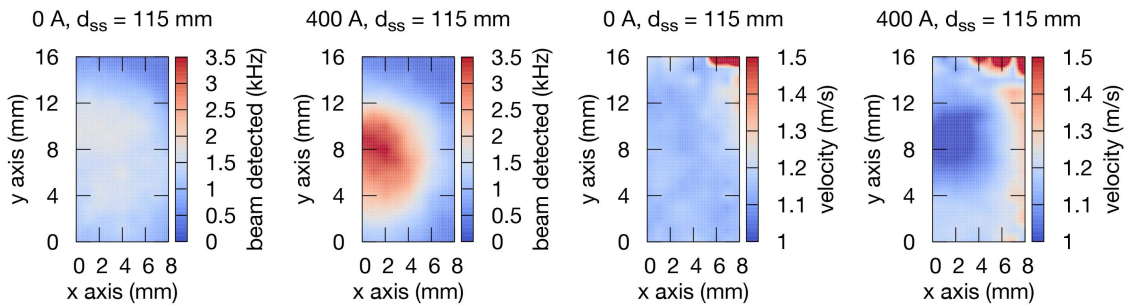


**Figure 3.13:** Beam profiles taken with the XY movable manipulator at permanent sextupole distance of 115 mm (beam rate and beam velocity). The beam focusing effect can be seen for the left two plots where the intensity of the beam increases for a higher superconducting sextupole magnetic field. The plots compare the beam rate when the superconducting sextupole is turned on to its maximal value (400 A) with sextupole turned off (0 A). The right two plots show for the same settings the focusing by looking at the velocity of the beam. The plots show that slower beam components are focused into the centre of the beam axis at the QMS position.

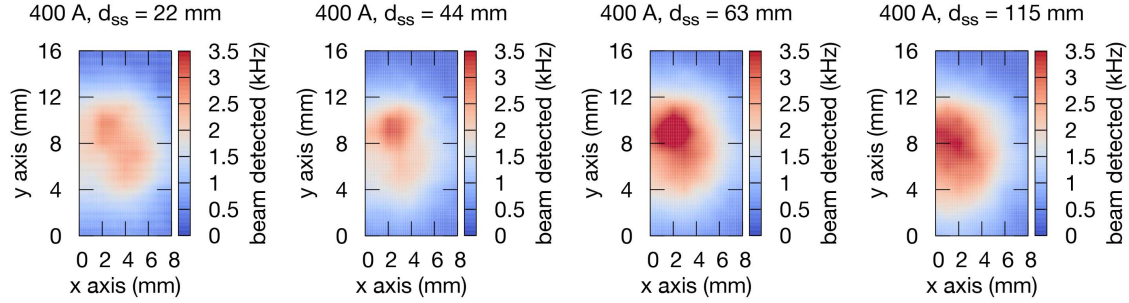


**Figure 3.14:** XY profiles for various permanent sextupole distances. From left plot ( $d_{ss} = 22$  mm) to right plot ( $d_{ss} = 115$  mm) the beam intensity is increasing.

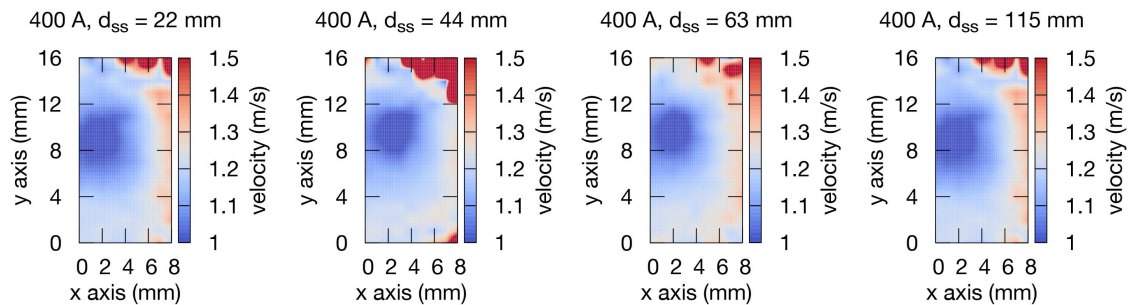


**Figure 3.15:** Velocity profiles for the XY scanned area for the same measurements as shown in fig 3.14.

side of the profiles show an asymmetry. Moreover the beam was apparently not perfectly aligned with respect to the laser axis (coordinates ( $x = 0$  mm,  $y = 0$  mm)). This behaviour is potentially coming from the alignment of the two permanent sextupole magnets. Given the fact that these magnets are about 3 meters away a slight misalignment of the detector it is not surprising.

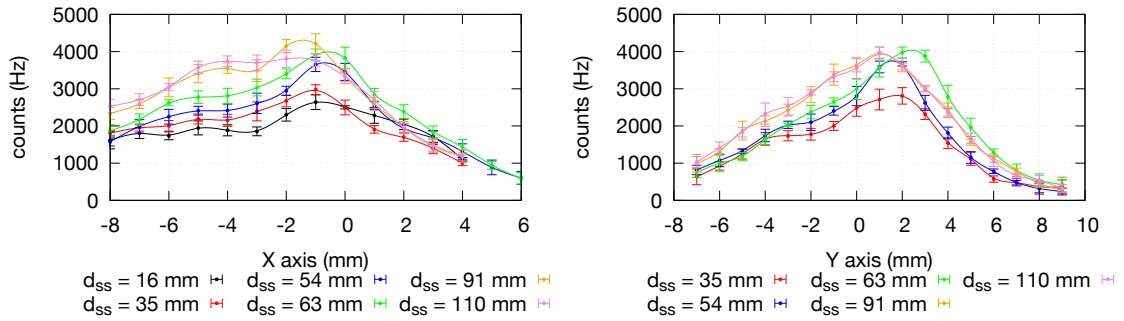


**Figure 3.16:** One-dimensional cut for the beam rate through the beam centre for the X axis (left) and for the Y axis (right). Apparently on the negative side the beam alignment is not optimal. Curves are interpolated to better highlight the individual settings.

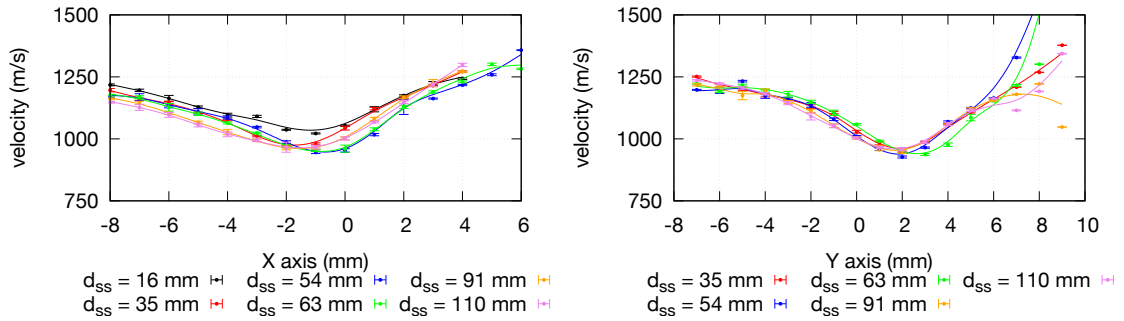


**Figure 3.17:** One-dimensional velocity cut through the beam centre for the X axis (left) and for the Y axis (right). Curves are interpolated to better highlight the individual settings.



# 4 Analysis of the resonance spectra

As has been described in section 1.3.1, spectra of rabi-like experiments show the total count rate as a function of the microwave frequency in the cavity. The occurrence of spin flips is registered as a drop in count rate. In this chapter more details on the fitting function of the hyperfine transitions will be presented. Moreover, the correct setting of the microwave power radiated into the cavity is of importance and power scans to assure this are presented in this chapter. Furthermore, first resonances of transitions in the earth's magnetic field are shown. Finally a method to estimate the degree of polarisation will be proposed.

## 4.1 Fitting function

The line shape of resonance curves for the strip line cavity can be calculated by numerically solving the optical Bloch equations. The main idea was already presented shortly in the last chapter, however, the state population density was calculated by C. Sauerzopf in his Ph.D. thesis [76] for the given cosine shape of the oscillating magnetic field amplitude along the Z axis of the cavity. The transition calculations were done by solving the von Neumann equation

$$\frac{\partial \hat{\rho}}{\partial t} = \frac{i}{\hbar} [\hat{H}_{\text{int}}, \hat{\rho}] \quad (4.1)$$

where  $\hat{\rho}$  is the density matrix and  $\hat{H}_{\text{int}}$  is the interaction Hamiltonian operator. The  $\hat{H}_{\text{int}}$  can be written as:

$$\hat{H}_{\text{int}} = \frac{(g_p \mu_N - g_e \mu_B)}{2} B_{\text{osc}} \cos\left(\frac{2\pi t}{\tau_{\text{int}}}\right) \quad 0 < t < \tau_{\text{int}} \quad (4.2)$$

where  $\mu_N$ ,  $\mu_B$ ,  $g_p$  and  $g_e$  are the nuclear and Bohr magneton, the proton and electron  $g$ -factors respectively and  $B_{\text{osc}}$  is the oscillating magnetic field in the cavity,

For the ground state hyperfine transition of atomic hydrogen four states are present. Their evolution can be treated by the optical Bloch equations using the generalised Rabi fre-

quencies in the rotating wave approximation. The generalised Rabi frequency is expressed as

$$\Omega' = \sqrt{\Omega_{\text{Rabi}}^2 + \Delta_{\text{detune}}^2} \quad (4.3)$$

where  $\Delta_{\text{detune}}$  is the detuning of a Rabi frequency and  $\Omega_{\text{Rabi}}$  is the Rabi frequency  $\Omega_{\text{Rabi}} = \mu B_{\text{osc}} / \hbar$ , which characterises the atom-field interaction strength ( $\mu$  - magnetic transition moment between two states).

The calculation yielded the double dip structure for the line shape of the strip line cavity. Figure 4.1 is the result of numerical calculations for different detuning and different oscillating magnetic field amplitudes for a mono-energetic beam [37, 76, 79].

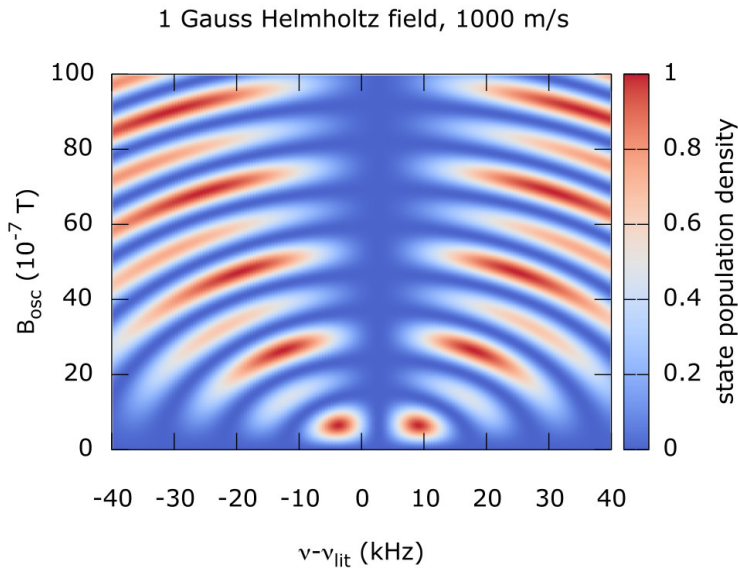


**Figure 4.1:** Calculated state population density map for a strip line cavity by using the optical Bloch equations (by C. Sauerzopf) for a single velocity of 1000 m/s. In the red regions the spin flips are occurring, while in the blue regions the hydrogen atoms are in initial state again.

A line shape template for a fitting function of the resonance curves was approximated by using the discrete data of the calculations. The main purpose of the fitting function of the hyperfine transition spectra is to extract the central frequency  $\nu_c$  with the smallest possible error.  $\nu_c$  is defined as the frequency in the centre between the two main dips of the resonance curve. The centre frequency is valid for one static magnetic field provided by the Helmholtz coils. However, it is important to understand that the external magnetic field is not necessary for the fitting function since this only leads to a shift (Zeeman effect) of  $\nu_c$  which is a parameter in the fitting function.

The interaction time of the atoms in the microwave field can be estimated by the line width of the resonance curve, which is approximately  $1/\tau_{\text{int}}$ . Thus, the velocity is proportional to the line width. Additionally from the conditions  $\Omega_{\text{Rabi}}\tau_{\text{int}} = \pi$  (see section 4.3) and  $\Omega_{\text{Rabi}} = \mu B_{\text{osc}}/\hbar$  it follows that  $B_{\text{osc}}$  will scale with  $1/v$ . Therefore, the velocity of a beam can be extracted as a scaling of the line width of the resonance curve and  $B_{\text{osc}}$  with reference to the theoretical map (figure 4.1). The numerical calculations were performed for one velocity (mono-energetic beam) and therefore, theoretical curves for other velocities were obtained by scaling from this velocities.

Additionally the fitting function approximated the gaussian velocity distribution with a convolution of binomially weighted discrete velocity components. Due to a reduction of computation time of the program the number of binomial components was set to  $n = 7$  where the steps were separated by  $\frac{n-1}{2}dv$ . Here  $dv$  is the distance between every velocity component.

The fitting routine was implemented by C. Jepsen during his internship at CERN. The idea was to use spline interpolations between the discrete calculated points in order to obtain a continuous function [80]. Thus, the function can be evaluated at any desired point in the function range.

The final fitting function then was:

$$\mathcal{F}(\nu; B_{\text{osc}}, \nu_c, v, \sigma_v, A, b) = A \cdot \mathcal{P}(\nu; B_{\text{osc}}, \nu_c, v, \sigma_v) + b \quad (4.4)$$

with  $\mathcal{F}$  being the fitting function,  $\mathcal{P}$  being the spin flip probability,  $\nu$  the frequency,  $B_{\text{osc}}$  the oscillating magnetic field in the cavity (in units  $10^{-7}$  T),  $\nu_c$  the centre frequency between the double dips (Hz),  $v$  the velocity of the particles ( $\text{km s}^{-1}$ ),  $\sigma_v$  ( $\propto dv$ ) the sigma of the gaussian velocity distribution ( $\text{km s}^{-1}$ ),  $A$  (Hz) amplitude for scaling the line shape to the amount of hydrogen atoms in a measurement and,  $b$  (Hz) a zero offset as baseline to take the background into account.

Figure 4.2 illustrates the effect of slight changes in the fitting parameters (centre frequency, baseline, amplitude, velocity, velocity spread, and oscillating magnetic field) on the line shape close to a  $\pi$ -pulse (first conversion maximum of the Rabi oscillation)

## 4.2 Total count rate vs. lock-in amplifier signal

As mentioned in previous chapters the tuning fork chopper modulates the beam and in combination with a lock-in amplifier is capable of suppressing background. In the final beam line the lock-in amplifier needed about 60 s of averaging to allow for a reliable

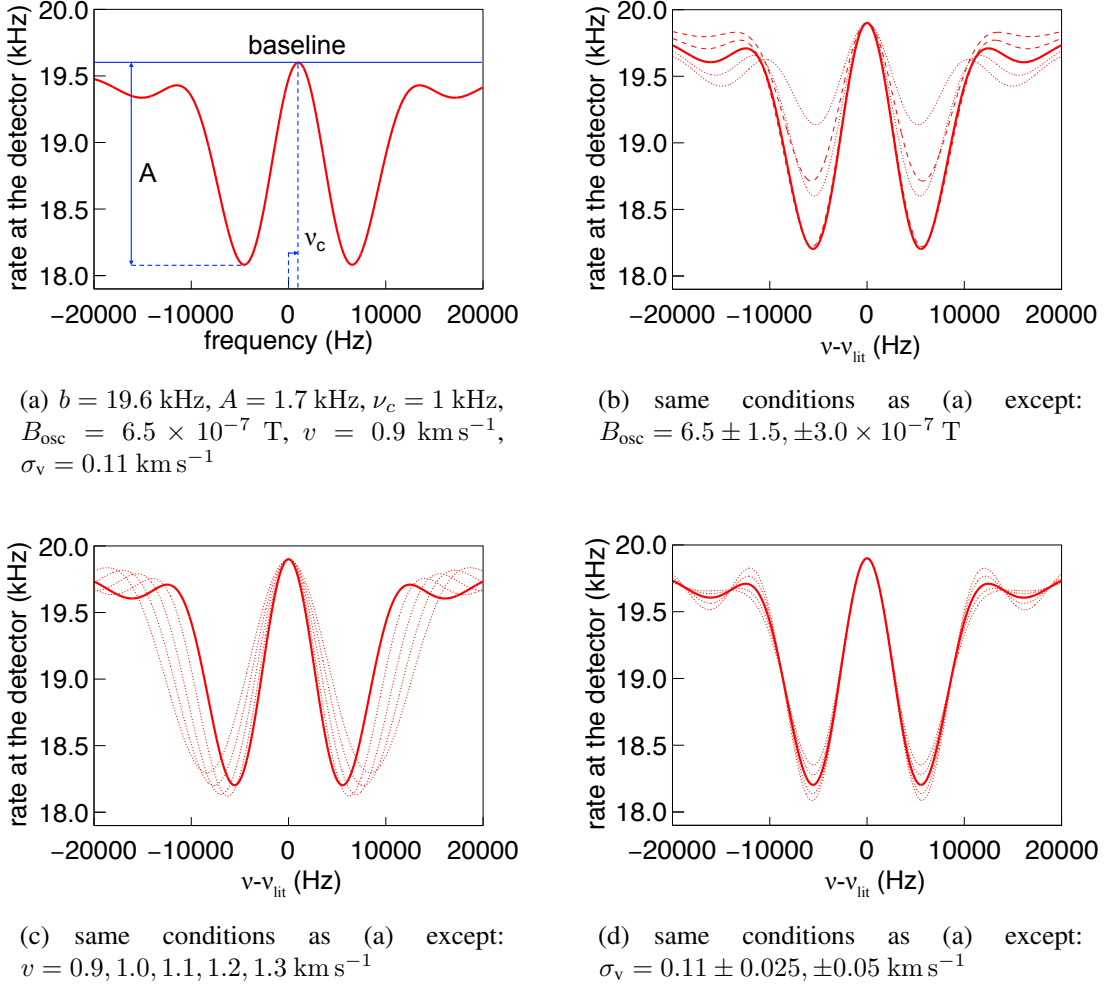


**Figure 4.2:** (a)-(d) Illustration of the parameters of the fitting function and influence of changes in the parameters for the resonance curve. (a) Description of the parameters amplitude  $A = 1.7$  kHz, baseline  $b = 19.6$  kHz and centre frequency  $\nu_c = 1$  kHz. (b) Variation of the oscillating magnetic field amplitude in the resonator. The red line corresponds to  $B_{\text{osc}} = 6.5 \times 10^{-7}$  T, the dashed lines correspond to  $B_{\text{osc}} = 5.0, 3.5 \times 10^{-7}$  T, the dotted lines correspond to  $B_{\text{osc}} = 8.0, 9.5 \times 10^{-7}$  T. (c) Curves for different velocities  $v = 0.9, 1.0, 1.1, 1.2, 1.3$  km s $^{-1}$  (d) Influence of velocity width on the spectra. The curves with flat side lobes show  $\sigma_v = 135, 160$  m s $^{-1}$  and ones with deeper lobes show  $\sigma_v = 60, 85$  m s $^{-1}$ .

reconstruction of the beam rate. Taking a hyperfine spectrum therefore can be rather time consuming. A way of reducing the acquisition time was by using the total count rate of the detector instead of the lock-in amplifier signal. It turned out that the background rate (not chopper phase-dependent signal) is also sensitive to the spin state selection, i.e. if spin flips to high field seekers occur which are defocused by the superconducting sextupole magnet the background count rate goes down. For crosschecks and tuning aspects the lock-in amplifier still was helpful and hence the chopper was not taken out of the beam line which would have increased the beam rate almost a factor of two (50 percent duty cycle).

## 4.3 Power scan and $\pi$ -pulse

An important concept in the experimental Rabi setup is the  $\pi$ -pulse. In the oscillating magnetic field, if on resonance between two states, the atom will be driven periodically between these two states. In a Rabi beam line the atom is in the microwave field for a certain time and will thus, see the microwaves for this period  $\tau_{\text{int}} = l_{\text{cav}}/v_{\text{H}}$ . A pulse of matching amplitude and duration, such that the population is driven once and completely from the initial to the final state is called  $\pi$ -pulse (named after the condition  $\Omega_{\text{Rabi}}t = \pi$ ). Depending on the magnitude of the oscillating magnetic field the atom can change the spin state and therefore,  $B_{\text{osc}}$  has to be adjusted before performing hyperfine transition measurements [42, 81–83].

Figure 4.1 shows that depending on the oscillating magnetic field strength the atoms are periodically driven back and forth between their spin states. Note that no Rabi oscillations can be observed at zero detuning due to the special line shape resulting from the magnetic field distribution in the strip-line resonator. A normal power scan corresponds to a scan along a vertical line in fig. 4.1.

$B_{\text{osc}}$  is proportional to the square root of the power transferred into the cavity  $\sqrt{P_{\text{MW}}}$  [81]. To reach a good working point the synthesiser output power should be tuned close to a  $\pi$ -pulse. The plots in figure 4.3 show the count rate when varying the power for a fixed detuning. For performing the measurement the frequency was set constant to one of the two main dips of a resonance curve and the input power was changed. In these experiments two cavities were available, where the first cavity was without the optimised RF contact springs and the for the second cavity the contact springs were spot welded onto the flange. The power measurement on the left hand side has been performed with the first cavity where the power coupling was not yet improved. Consequently only one Rabi oscillation could be driven at maximal power. The right plot shows a power measurement for the

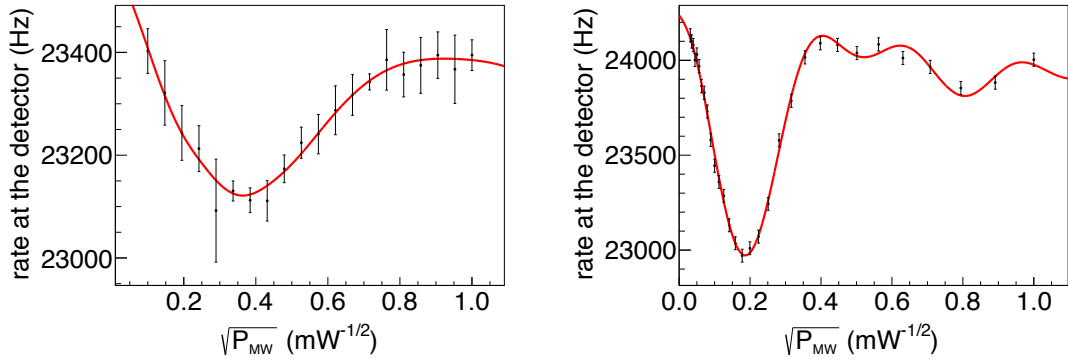
second cavity where the power coupling was improved. Here with increased power more spin flip periods could be driven. The largest observable count rate drop happens for a  $\pi$ -pulse.

## 4.4 Power vs. frequency maps

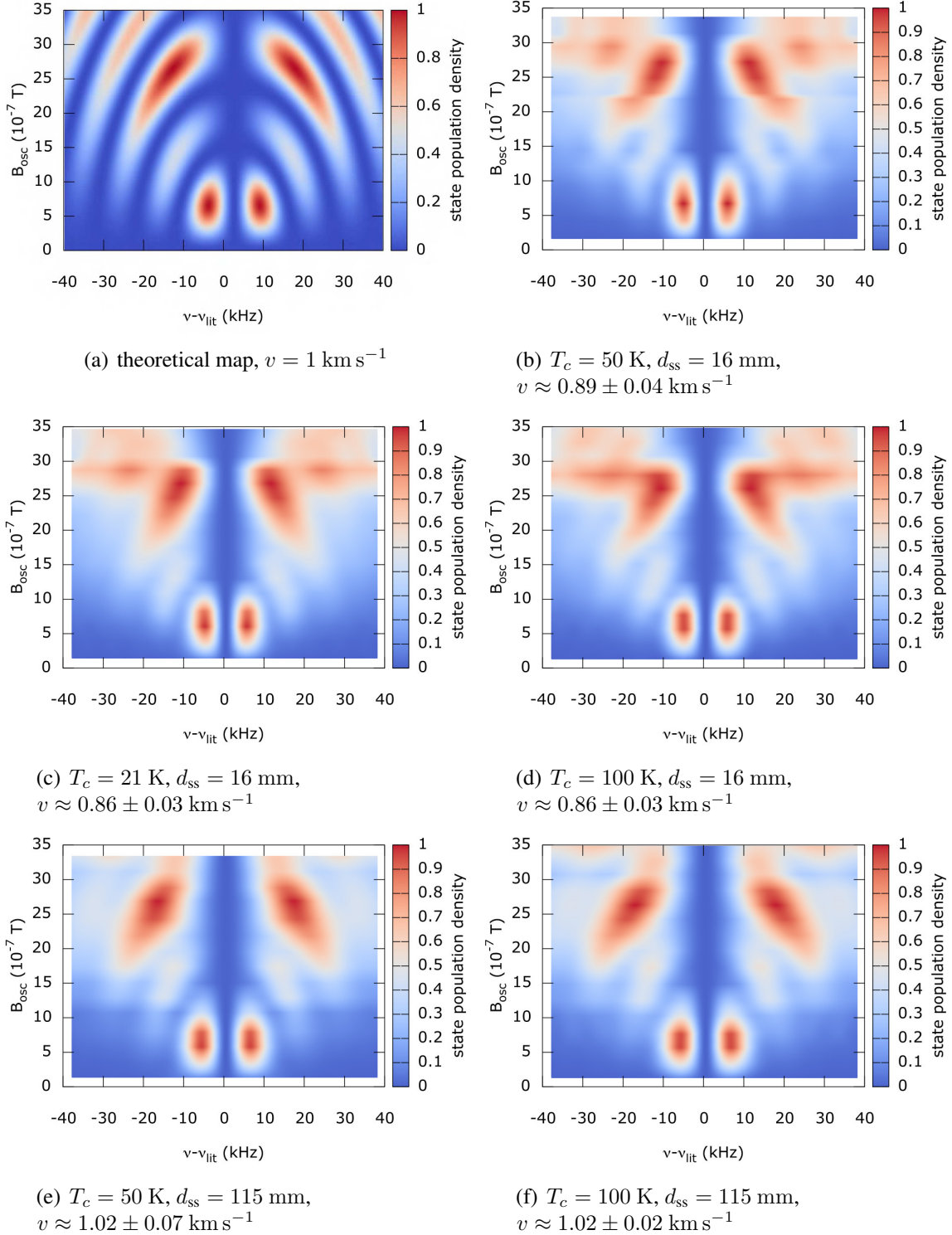
By recording frequency spectra at a sequence of microwave powers (or equivalently  $B_{\text{osc}}$ ) the theoretical conversion map of fig 4.1 can be approximated by a measurement. In total 5 measurement sets were performed at 16 different  $B_{\text{osc}}$ . For every scan the changes of the input power of the cavity were done in steps of the square root of the power. This variation is linear proportional to changes in the oscillating magnetic field  $B_{\text{osc}}$ . The aforementioned function 4.4 was fitted into the scans which yielded continuous curves for every  $B_{\text{osc}}$ . For every scan the spin flip probabilities  $p_{\sigma 1}$  were evaluated from a spline interpolation of the theoretical map (figure 4.1) according to the oscillating magnetic field extracted by the fit ( $B_{\text{osc}}$  yielded  $p_{\sigma 1}$ : see section 4.5). To gain a smooth map the data was interpolated. For these plots  $B_{\text{osc}}$  was fixed by the cavity input power as will be described in the next chapter.

Figure 4.4 shows these maps for different settings and also the theoretical one for comparison. The main difference between the theoretical map and the recorded one is that the theoretical map is calculated with a fixed velocity without field inhomogeneity whereas the measured one has the gaussian velocity spread. Figure 4.5 shows the same data but the colour axis is normalised in another way. The lowest value of the fitting function is subtracted from the function and then normalised by the function height:  $(f - \min(f))/A$ . This normalisation shows better the regions of minima of the fitting function. The maximal spin flip regions for every resonance are projected, but no physical interpretation except the projection of spin flip regions should be derived.

In addition to confirming that the resonance structures are well understood, these maps show that the velocity selection of the permanent sextupoles works as expected. In contrast the temperature of the coldhead  $T_c$  does not influence the velocity in this configuration. Furthermore the maps show that enough power is available in the cavity to drive spin flips at the optimal regions.



**Figure 4.3:** Power scans with count rate at the detector vs. synthesiser power; left: before spot welded contact springs; right: after spot welded contact springs - more conversions can be performed. The function fitted into the data was derived similarly to the resonance curve, but instead of plotting along  $\nu$  at a constant  $B_{\text{osc}}$  the function was plotted in  $B_{\text{osc}}$  direction for constant  $\nu$ . With the information of a power scan the synthesiser could be set to the optimal value, where the largest number of spin flips occurs. left figure:  $\chi^2 = 0.19$ ,  $\min(\sqrt{P}) = 0.36 \text{ mW}^{-1/2} = -8.9 \text{ dBm}$  at synthesiser, right figure:  $\chi^2 = 0.96$ ,  $\min(\sqrt{P}) = 0.19 \text{ mW}^{-1/2} = -14.4 \text{ dBm}$  at synthesiser.



**Figure 4.4:** Spin flip maps; (a) the theoretical map for the strip line cavity simulated at  $1 \text{ km s}^{-1}$ . (b), (c), (d) were measured at  $d_{\text{ss}} = 16 \text{ mm}$ . This distance yields a velocity of the beam of about  $0.86 - 0.89 \text{ km s}^{-1}$ . (e), (f) were measured with  $d_{\text{ss}} = 115 \text{ mm}$  yielding a velocity  $\sim 1 \text{ km s}^{-1}$ . The coldhead temperature does not matter, but  $d_{\text{ss}}$  sets the velocity of the polarised beam. The plots consist of 16 resonances for different  $B_{\text{osc}}$ , interpolated between each other. The red regions show the probable spin flip areas, in the blue regions the atoms are in the initial state.

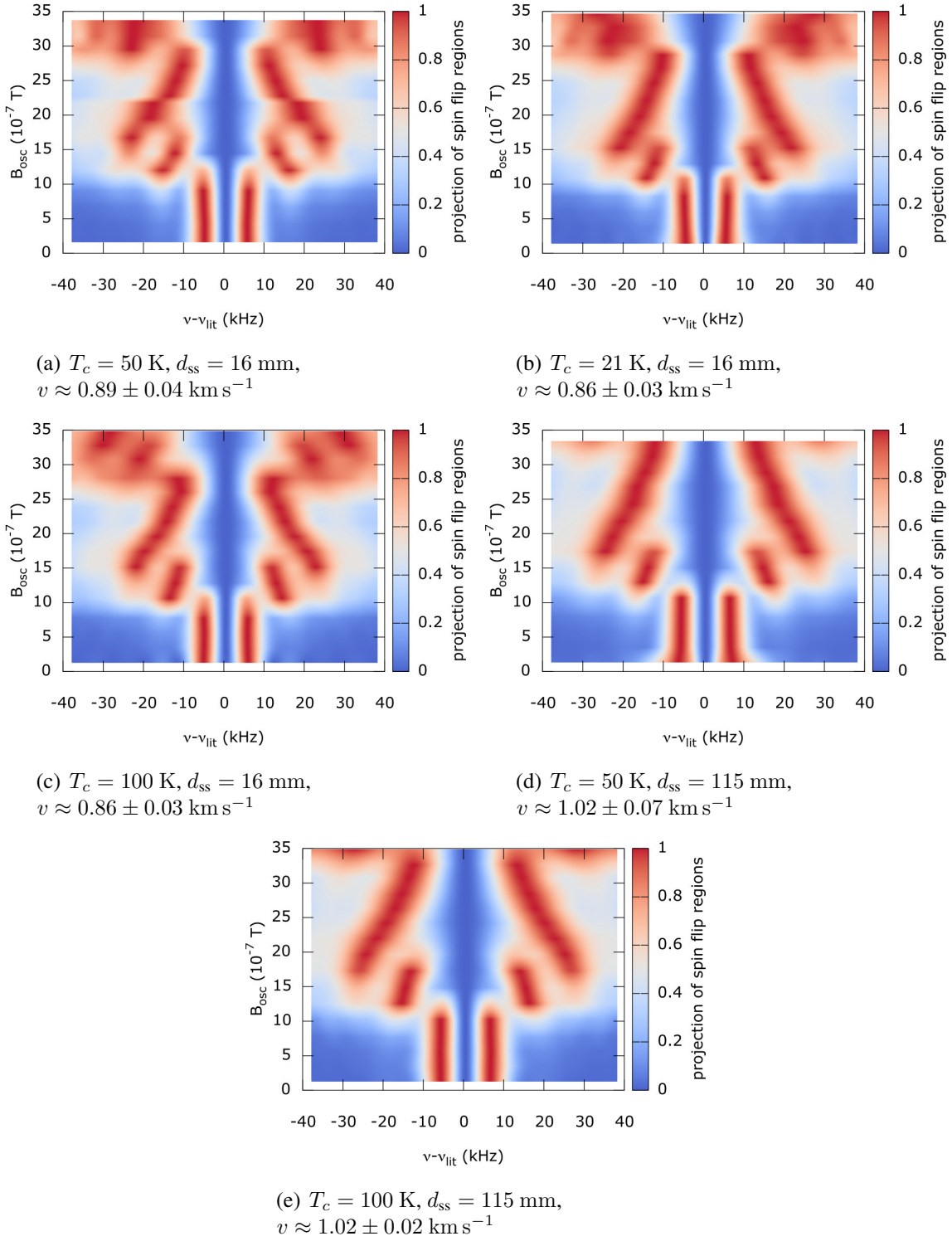


**Figure 4.5:** Same data as in 4.4 but every resonance was normalised by subtracting the minimum value of the resonance curve and divided by the resonance height. With this type of normalisation the areas of highest spin flip probability appear more pronounced and the difference between (a)-(c) and (d)-(e) is more clear.

## 4.5 Polarisation

The initial requirement in a Rabi experiment is having a polarised beam. In chapter 2.7 it was mentioned that simulations showed a degree of polarisation of  $99.2^{+0.8}_{-8}\%$ . In the following the degree of polarisation is defined as

$$P = \frac{\dot{N}_{LFS}}{\dot{N}_{LFS} + \dot{N}_{HFS}} \quad (4.5)$$

where  $\dot{N}_{LFS}$  is the count rate of low field seekers and  $\dot{N}_{HFS}$  is the count rate of high field seekers which will be defined as:

$$\dot{N}_{HFS} = \dot{N}(0, 0) + \dot{N}(1, -1) \quad (4.6)$$

$$\dot{N}(1, -1) = \dot{N}(0, 0) \quad (4.7)$$

$$\dot{N}_{LFS} = \dot{N}(1, 0) + \dot{N}(1, 1) \quad (4.8)$$

$$\dot{N}(1, 0) = \dot{N}(1, 1), \quad (4.9)$$

$\dot{N}(F, M)$  being the count rate of atoms in the different states, and  $\dot{N}_{LFS}$  and  $\dot{N}_{HFS}$  being the count rate of low field seeking and high field seeking states respectively. The abundance of the states in the equations 4.7 and 4.9 is the same, since the magnets part the atoms depending on *HFS* state or *LFS* state in equal amounts. By analysing resonance curves of the hyperfine transitions recorded with the lock-in amplifier the degree of polarisation of the beam can be estimated. The illustration of the different effects contributing to the approximation can be seen in figure 4.6.

In a  $\sigma_1$  scan the  $(M, F) = (1, 0)$  state is the low field seeking state that can perform the transition  $(1, 0) \rightarrow (0, 0)$ . At the detector the measured drop in counting rate  $\Delta_{\text{meas}} = \dot{N}_{\text{max}} - \dot{N}_{\text{min}}$  shows that only parts of the atoms perform a  $\sigma_1$  transition. Additionally to  $\Delta_{\text{meas}}$  some effects have to be considered.

First, the hydrogen beam had a certain velocity spread and thus, not all the atoms in the  $(1, 0)$  state could do a spin flip. The reason is that some atoms were faster and therefore would not see a perfect  $\pi$ -pulse best for the according velocity component. The factor taking this velocity smear into account is called  $x_v$ .

For the analysed data the average spin flip probability was less than 100 %. The factor was  $x_v$  was  $94 \pm 2\%$  and was derived by doing a spline interpolation for  $B_{\text{osc}}$  found by fitting function 4.4 in frequency  $\nu(B_{\text{osc}})$ . From the derived curve the minimum of one of the side lobes  $\nu_{\text{min}} = \min(\nu(B_{\text{osc}}))$  was determined. By introducing an effective

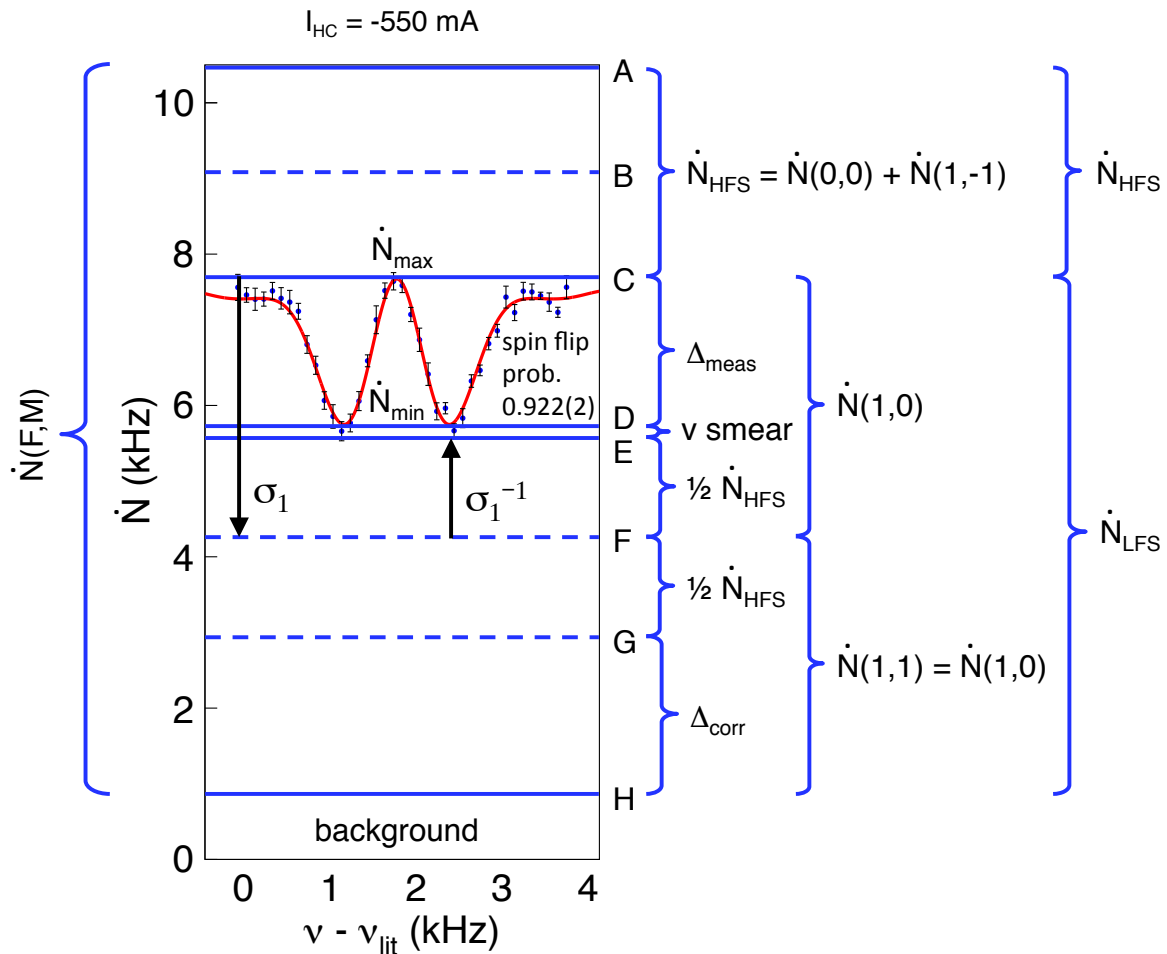


**Figure 4.6:** Estimation of effects contributing to the polarisation of the hydrogen beam. Typical spectrum which was recorded with the lock-in amplifier. A: estimated signal after the polarising magnets; A-C: HFS consisting half of  $(F, M) = (0, 0)$  and half of  $(1, -1)$ ; C: maximum count rate *max*; C-D: taken HFS spectrum; D: minimum counting rate; D-E: velocity smear (taken into account by  $x_v$ ); E-F: the  $(F, M) = (0, 0)$  state will effectively decrease the signal amplitude with the  $\sigma_1^{-1}$  spin flips; C-F estimated signal of  $(F, M) = (1, 0)$ ; F-H same amount as C-F for the  $(F, M) = (1, 1)$

oscillating magnetic field which accounts for the individual velocity components of the beam  $B_{\text{osc } i}^{\text{eff}} = B_{\text{osc}}/v_i$  where  $v_i$  stands for the individual velocity component, the overall spin flip probability  $x_v$  of the beam is given as:

$$x_v = 1 - \sum_{i=1}^n p_{vi}(p_{\sigma_1}(\nu_{\min}, B_{\text{osc } i}^{\text{eff}})) \quad (4.10)$$

Here  $p_{vi}$  is the binomial weighting factor which takes the individual velocity abundances into account.  $p_{\sigma_1}(\nu_{\min}, B_{\text{osc } i}^{\text{eff}})$  is the probability at  $\nu_{\min}$  and at the effective oscillating magnetic field to perform a spin flip.

Therefore,  $\Delta_{\text{meas}}$  has to be adjusted by  $x_v$ :

$$\Delta_{\text{meas}} = x_v \Delta_{\text{corr}} \quad (4.11)$$

$$\Rightarrow \Delta_{\text{corr}} = \Delta_{\text{meas}}/x_v \quad (4.12)$$

Second, since the beam is not fully polarised the  $(M, F) = (0, 0)$  high field seekers will perform a spin flip from  $(M, F) = (0, 0) \rightarrow (1, 0)$ , here called  $\sigma_1^{-1}$ . The atoms performing these spin flips will be counteracting the signal drop at the detector by decreasing the signal amplitude.

As a last part an additional background signal ( $\dot{N}_{BG}$ ) should be taken into account. The atoms passing the sextupoles (permanent and superconducting) at the very centre will not be deflected enough by the inhomogeneous magnetic field and hence participate to the signal. This means that the beam amount without the usage of the superconducting sextupole (0 A) contains a certain non polarised amount of the *LFS* and *HFS*. The beam with superconducting sextupole magnet turned off can be used to estimate upper limits for  $\dot{N}_{BG}$ . It still has to be considered that approximately 5 percent of the beam at 0 A in the superconducting sextupole magnet will be coming from molecular hydrogen background, which is due to the effect that  $H^+$  ions are also formed of  $H_2$  in the QMS ionisation housing ( $H_2 + e^- \rightarrow H^+ + H + e^- + e^-$ , see section 2.3). Therefore, lower additional limits can be assumed.

With all this studies the amount of the high field seekers and low field seekers can be estimated as:

$$\dot{N}_{HFS} = \dot{N}_{\text{max}} - \frac{2\Delta_{\text{meas}}}{x_v} - \dot{N}_{BG} \quad (4.13)$$

$$\dot{N}_{LFS} = \dot{N}_{\text{max}} - \dot{N}_{BG} \quad (4.14)$$

which yields a formula for the polarisation:

$$\begin{aligned}
 P &= \frac{\dot{N}_{LFS}}{\dot{N}_{LFS} + \dot{N}_{HFS}} = \frac{\dot{N}_{max} - \dot{N}_{BG}}{2\dot{N}_{max} - 2\Delta_{meas}/x_v - 2\dot{N}_{BG}} \\
 &= \frac{1}{2} \frac{1 - \frac{\dot{N}_{BG}}{\dot{N}_{max}}}{1 - \frac{\Delta_{meas}}{\dot{N}_{max} x_v} - \frac{\dot{N}_{BG}}{\dot{N}_{max}}}
 \end{aligned} \tag{4.15}$$

The polarisation for the beam, measured with the numbers of 12 resonance scans for  $d_{ss} = 16$  mm and 12 resonance scans for  $d_{ss} = 115$  mm, can therefore be expected to be:

$$0.67 < P < 0.71 \quad \text{for } d_{ss} = 16 \text{ mm} \tag{4.16}$$

$$0.72 < P < 0.78 \quad \text{for } d_{ss} = 115 \text{ mm} \tag{4.17}$$

Depending on how  $\dot{N}_{BG}$  is chosen the lower bound uses  $H_2$  background only whereas the upper limit is chosen if additionally to  $H_2$  a maximally unpolarised central beam is added.

The slight polarisation difference between the two permanent sextupole distances can be explained such: when the magnets are closer it is more likely that  $HFS$  will pass because of the higher solid angle of the aperture between the two magnets. When more distant, defocused  $HFS$  will not be able to pass. Qualitatively the distance dependent polarisation is in agreement with simulations. The difference derived by simulations is that the polarisation is less than the 99.2 %

One consideration that has not been taken into account is the loss in detector signal at the QMS due to the repetitive character of the beam resulting from the chopper. The disadvantage of the tuning fork chopper is that its frequency is fixed to one frequency due to its spring constant. Therefore, the longer the distance between chopper and detector the velocity distribution will more and more smear out the signal at the detector. At some point the signals will overlap and the signal below the minimum will be detected as background signal. This behaviour is illustrated in figure 4.7 where the detector function is displayed vs. time by using the fitting function described in equation 2.6 for the periodic signal results from the single cycles of the chopper. For this plot the average values for the velocity and velocity spread from the 12+12 polarisation estimation resonance scans were taken and function 4.4 was plotted by using these values. The loss in signal is about 4 %. The not detected signal was obtained by subtracting the overall function of one signal cycle.

However, the loss was not taken into account for the polarisation estimations, since hyperfine states should be distributed equally in the detected but also in the not detected signal. For an estimation of the polarised atoms the total count rate is not of importance,

because in the fractional measurement the *LFS* and *HFS* abundances should be equally distributed as in the full beam rate. Therefore, the measured count rate should yield the same results and the approximation as explained before can be used.

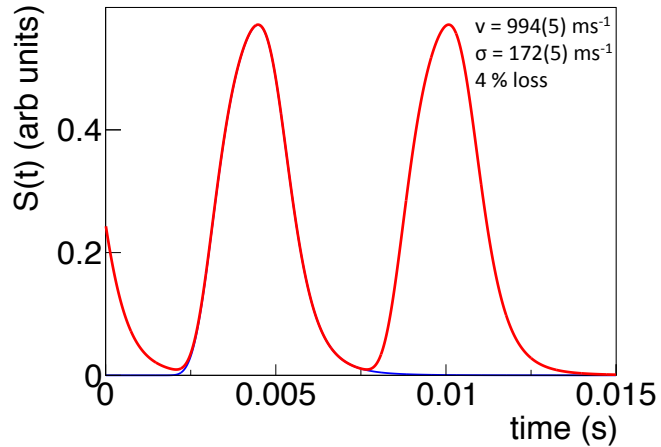


**Figure 4.7:** Calculated signal at the detector with average velocity and velocity spread from transition measurements. Approximately 4 % of the signal cannot be identified by the lock-in amplifier signal due to the overlap of the modulated beam. The red lines show the periodic signal and the blue line shows the signal for one single not periodic chopper cycle.

# 5 Results and discussion

## 5.1 General considerations

The value of interest is the zero-field hyperfine structure. The transition frequencies obtained from resonance spectra as described above are taken at certain external magnetic field strengths, which are not known to high precision. Therefore, methods have to be used, that allow for the extraction of the zero-field hyperfine splitting from a set of transition frequency measurements. Two different methods are presented here:

1. measure the  $\pi_1$  and the  $\sigma_1$  transition at the same static magnetic field. As the only two unknowns are this single magnetic field value and the zero-field splitting, the two measured frequencies are sufficient to calculate those two unknowns by usage of the Rabi equations 1.4-1.7.
2. Measure the  $\sigma_1$  transition at different static magnetic fields and perform an extrapolation to zero field by also using the Rabi formulas. As each transition frequency is obtained at a different field value a fitting procedure has to be applied.

A comparison of the two methods using numerical simulations is presented by B. Kolbinger et al. [39]. This study showed that the method 1 has the advantages that no more than two transition measurements are needed, whereas for the second method at least three resonance curves have to be measured. However, the homogeneity of the static magnetic field for method 1 has to be higher than for method 2 since the  $\pi_1$  transition is more sensitive to field changes. For method 2 the field homogeneity is less critical because only  $\sigma_1$  transitions are needed (see figure 5.1). For a  $\sigma_1$  transition the oscillating magnetic field should be parallel to the static one ( $\vec{B}_{\text{osc}} \parallel \vec{B}_{\text{stat}}$ ) whereas for the  $\pi_1$  transition the fields should be orthogonal ( $\vec{B}_{\text{osc}} \perp \vec{B}_{\text{stat}}$ ) [84]. Experimentally this could be realised by a set of two Helmholtz coils for the parallel and orthogonal field components, or one set of Helmholtz coils having a certain angle between the orthogonal and parallel alignment. The orientation of the magnetic fields should be chosen, that the Rabi frequency is strong enough to drive both transitions. For the Breit-Rabi diagram the absolute value

of the static magnetic field  $|\vec{B}_{\text{stat}}|$  defines the transition frequency. However, for the given experiments the Helmholtz coils were aligned parallel to drive only  $\sigma_1$  transitions. In the following sections method 1 will be presented by using measurements taken in the earth's magnetic field. Later the main focus will be on the zero field extrapolation achieved by the  $\sigma_1$  transitions. Systematical properties were investigated and a comprehensive understanding of the spin flip resonator has been achieved.

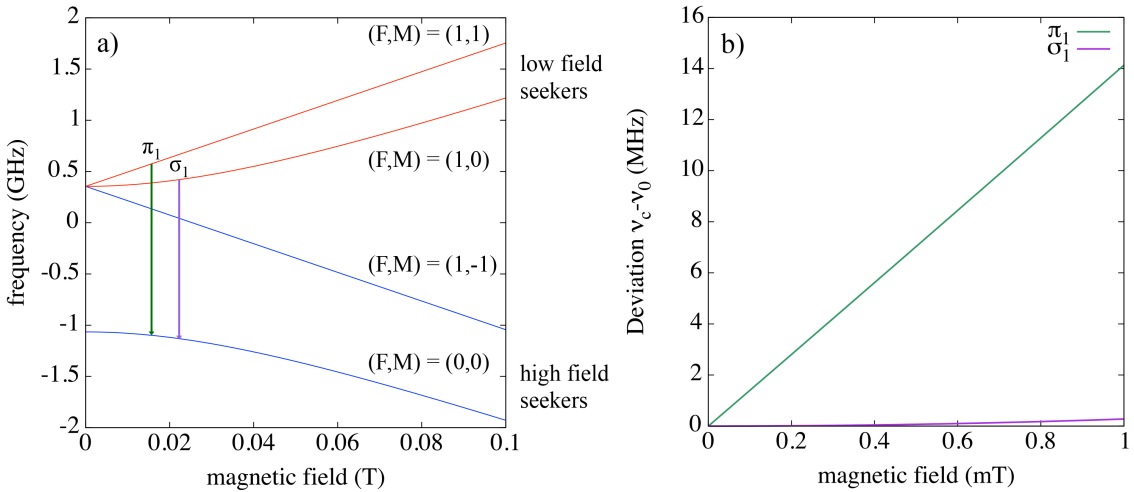


**Figure 5.1:** a) Breit-Rabi diagram for atomic hydrogen, b) Frequencies for  $\pi_1$  and the  $\sigma_1$  transitions as a function of the magnetic field. At weak magnetic fields the  $\pi_1$  transition shifts faster and therefore, is more critical to magnetic field inhomogeneities. Note that the units for the X axis of graph a) are given in T whereas in b) are given in mT (taken from [85]).

## 5.2 $\nu_0$ determination by usage of $\sigma_1$ and $\pi_1$ transitions in the earth's magnetic field

First test measurements of hyperfine transitions could be performed without Helmholtz coils and magnetic shielding. The  $\vec{B}_{\text{stat}}$  had to have an angle towards  $\vec{B}_{\text{osc}}$  so that both the parallel and orthogonal components were non zero. The Zeeman splitting was induced by the earth's magnetic field, which had non zero components for both magnetic fields. As published in [85] it could be shown that the apparatus is capable of measuring  $\sigma_1$  and  $\pi_1$  transitions. Figure 5.2 shows the data as published but reanalysed with the line shape as described in chapter 4. As table 5.1 shows, for both transitions the magnetic fields calculated from the Rabi formulas by inserting the extracted centre frequencies and the measured magnetic field of the earth are in agreement within error bars. Additionally the

$\pi_1$  transition could be resolved despite the fact that the  $\pi_1$  transition is more sensitive to inhomogeneities of the static magnetic field.

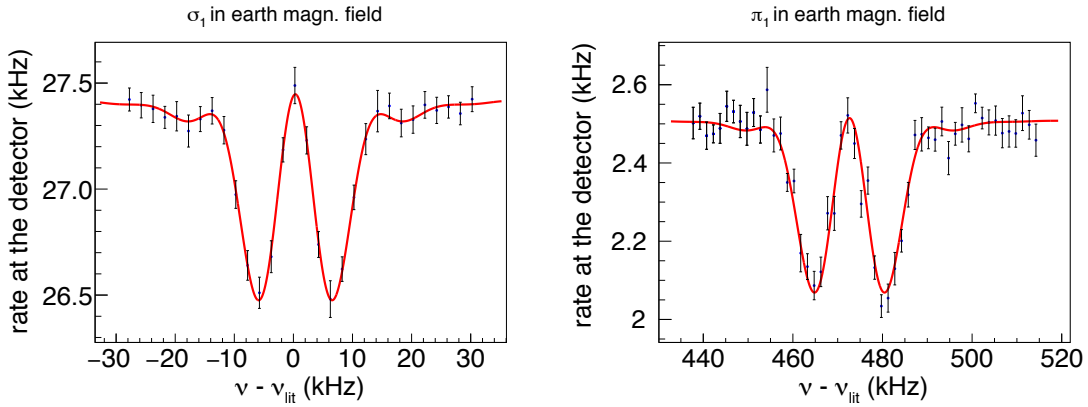


**Figure 5.2:**  $\pi_1$  and  $\sigma_1$  in earth magnetic field reanalysed. For these spectra the data acquisition was not yet optimised. The  $\sigma_1$  transition was analysed using the total count rate and the  $\pi_1$  transition was analysed using the lock-in amplifier signal.

**Table 5.1:** Results for  $\pi_1$  and  $\sigma_1$  transitions in the earth's magnetic field: First column: transition name. Second column: the centre frequency minus literature value. The errors are statistical and come from the fit. Third column: magnetic field calculated with Breit-Rabi formula using centre frequency of the fit and the literature value  $\nu_0$  for the zero-field splitting. The error comes from error propagation. Fifth column: the measured magnetic field.

transition	$\nu_c - \nu_0$ (Hz)	calculated magn. field ( $\mu\text{T}$ )	measured magn. field ( $\mu\text{T}$ )
$\sigma_1$	$337 \pm 113$	$34.9 \pm 5.8$	
$\pi_1$	$472640 \pm 134$	$33.78 \pm 0.01$	$37 \pm 4.2$

The formula for method one derived from the Rabi equations for calculating back the  $\nu_0$  is given below [39]

$$\nu_0 = \frac{g_+ \sqrt{g_+^2 \nu_\sigma^2 - 4g_-^2 \nu_\pi^2 + 4g_-^2 \nu_\pi \nu_\sigma} + g_-^2 (2\nu_\pi - \nu_\sigma)}{g_+^2 + g_-^2} \quad (5.1)$$

where  $g_\pm = g_I \pm g_J$ ,  $g_I$  is the magnetic moment of the atom's electrons in units of the Bohr magneton. In the case of ground-state H (single electron,  $l = 0$ ):  $g_J = g_e$ ,  $g_I = g_p m_e / m_p$  is the magnetic moment of the proton (nucleus of hydrogen) in units of the Bohr magneton,  $g_p$  the proton g factor,  $m_e$  the mass of the electron,  $m_p$  the mass of the

proton,  $\nu_\pi$  the transition frequency for the  $\pi_1$  transition, and  $\nu_\sigma$  the transition frequency for the  $\sigma_1$  transition. Both transitions ( $\sigma_1$  and  $\pi_1$ ) have to be measured at the same magnetic field.

The measurements from section 5.2 in the earth's magnetic field can be used to perform a zero field calculation for  $\nu_0$ . Using the extracted fit values for  $\nu_c$  for the  $\sigma_1$  and the  $\pi_1$  transitions and applying formula 5.1 yields for  $\nu_0 = 1\,420\,405\,776 \pm 88$  Hz which has a relative error of  $6 \times 10^{-8}$ . This value deviates from the literature value by 25 Hz and agrees within the error.

### 5.3 Extrapolation to zero magnetic field with $\sigma_1$ transitions

The second method where  $\nu_0$  is extracted from  $\sigma_1$  transitions at different static magnetic fields can be performed by using the following formulas also derived from the Rabi formulas:

$$\nu_c(I_{\text{HC}}; d\nu, C, B_0) = (\nu_{\text{lit}} + d\nu) \sqrt{1 + \lambda^2(CI_{\text{HC}} - B_0)^2} \quad (5.2)$$

Here  $\nu_c$  - the centre frequency of the resonance curve fitting function (see figure 4.2) - is the frequency obtained for the transition at a certain current in the Helmholtz coils  $I_{\text{HC}}$ .  $\nu_{\text{lit}}$  is the literature value for the transition frequency (see eq. 1.3),  $\lambda$  is a constant which can be expressed by the Landé factor of the coupled spin angular momentum and proton g-factors  $g_J$  (for ground-state hyperfine splitting of H the angular momentum = 0  $\rightarrow g_J = g_e$ ) and once more  $g_p$ , the nuclear and the Bohr magneton  $\mu_N$  and  $\mu_B$ ,  $\nu_{\text{lit}}$  and the Planck constant:

$$\lambda = \left( g_J + g_p \frac{\mu_N}{\mu_B} \right) \frac{\mu_B}{\nu_{\text{lit}} h} = 19.76021982 \text{ T}^{-1} \quad (5.3)$$

where  $\mu_N = 3.1524512326(45) \times 10^{-8} \text{ eV T}^{-1}$ , numerical values for  $\mu_B$ ,  $g_p$  and  $g_J$  are listed in section 1.2.3.

$d\nu, C, B_0$  are fitting parameters. The parameter  $d\nu$  describes a deviation of  $\nu_{\text{lit}}$ ,  $C$  is a conversion factor from a current to a magnetic field (in units T/A) and  $B_0$  is a potential residual static magnetic field inside the shielding.

For numerical reasons the fitting function was used in a way that  $\nu_{\text{lit}}$  was subtracted.

$$(\nu_c - \nu_{\text{lit}}) = (\nu_{\text{lit}} + d\nu) \sqrt{1 + \lambda^2(CI_{\text{HC}} - B_0)^2} - \nu_{\text{lit}} \quad (5.4)$$

In figure 5.3 effects of the fitting parameters  $B_0$  and  $C$  are illustrated.

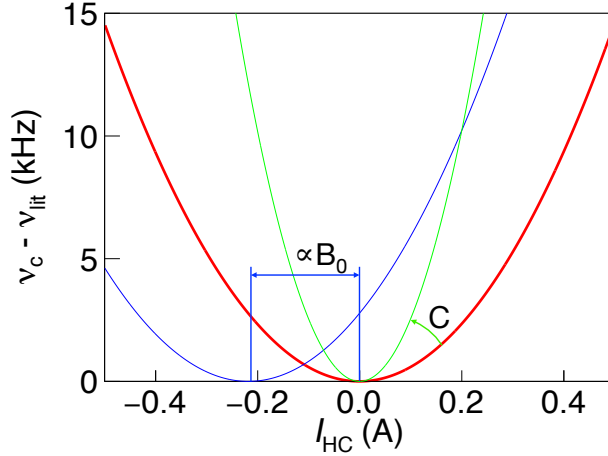


**Figure 5.3:** Explanation of the extrapolation curve fitting parameters. The residual magnetic field  $B_0$  (blue curve) leads to a shift on the x-axis whereas conversion factor  $C$  results in a bigger or smaller slope (green curve).

### 5.3.1 Settings of the $\sigma_1$ measurement sets

Resonance spectra have been taken at different external magnetic field values, controlled through the current in the Helmholtz coils, while leaving all other experimental settings unchanged. Typically 40 such spectra yielded a set to obtain one zero-field hyperfine splitting value by extrapolation. In total 10 such sets have been taken under different conditions. The parameters that have been varied are listed below and an illustrative overview is also shown in fig. 5.3. Figure 5.4 shows the variations between the sets and 5.5 shows schematically an overview of the experiment with DAQ and some of the variations in the setup.

- Source alignment: straight for sets 1-3, 90 degree for sets 4-10.
- Cavity: exchange of cavity for sets 7-10 .
- Magnetic field polarity: with exception of set 4 all sets were measured with positive and negative polarity.
- Shielding: with exception of set 7 all sets were measured with two layers of shielding.

- Beam diameter: for the sets 9 and 10 the last aperture before the cavity (aperture 2 see figure 3.1) was exchanged by another differential pumping aperture with a bigger radius. Hence, the beam had a bigger diameter.
- Beam velocity:  $d_{ss}$  was varied to select different velocities. As it turned out  $T_c$  is not crucial, therefore, the variation of the coldhead temperature was stopped after the first three sets.
- Strength of the superconducting sextupole: all sets were taken at 350 A except set 3, which was taken at 400 A.
- Data acquisition, and coils current measurement (see below).

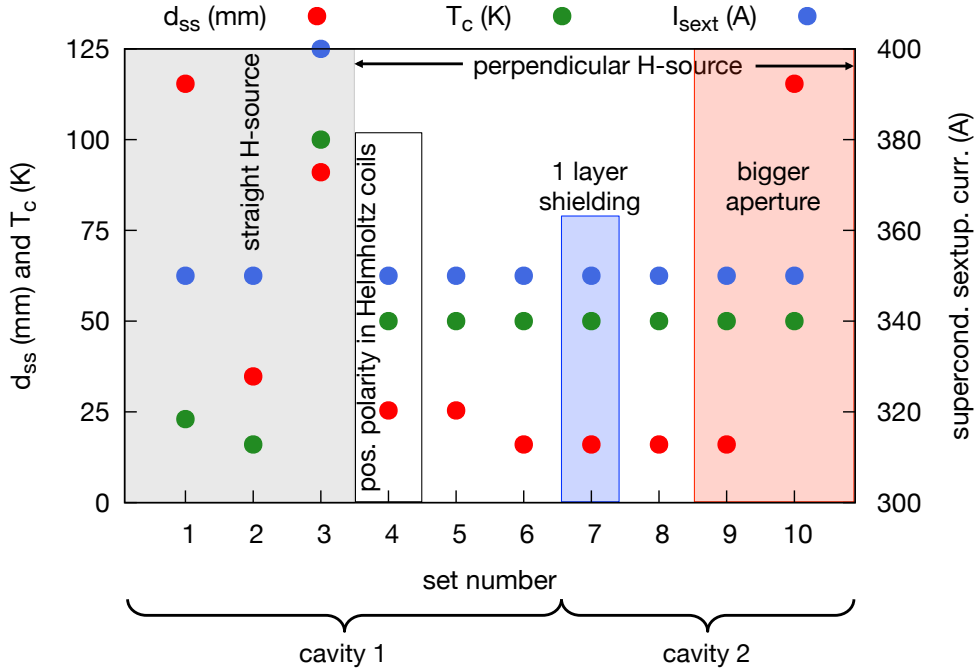


**Figure 5.4:** Settings for all  $\sigma_1$  extrapolation sets. Extrapolations 1-3 were still recorded with not optimised parameters, and had the atomic hydrogen source straight aligned. Set 9 and 10 used the bigger beam pipe aperture.

$d_{ss}$  - distance between the permanent sextupole magnets,  $T_c$  - temperature of the coldhead / tubing, current in the superconducting sextupole magnet are displayed. A more detailed overview of the settings can be found in the appendix table A.4

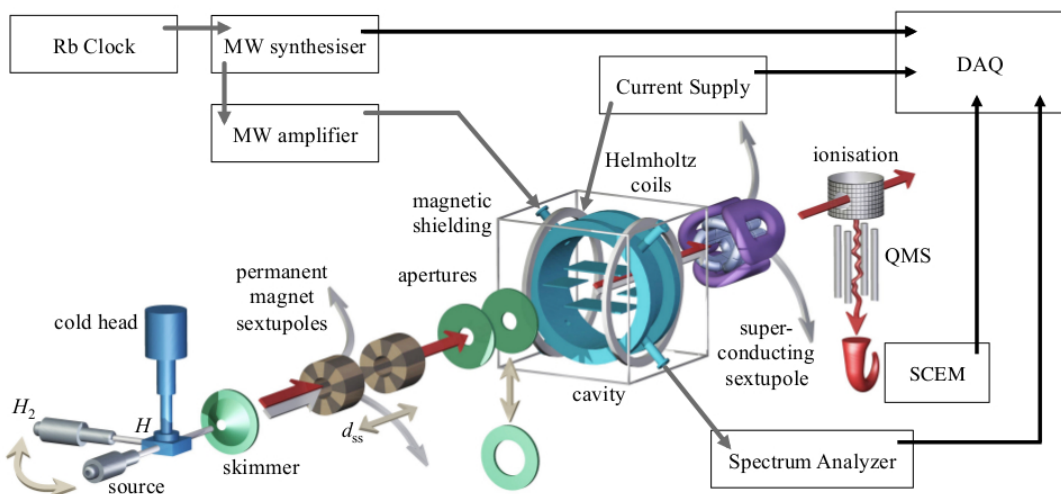


**Figure 5.5:** Schematic drawing of the Hydrogen beam setup and DAQ scheme.

As pointed out in chapter 2, the hydrogen source was employed in two different ways. First the hydrogen atoms were directed straight in beam direction (sets 1-3). In this configuration generally the velocities of the atoms were higher. In contrast all other transitions were performed by using the hydrogen source perpendicular to the beam axis.

A second major variation was that the spin flip resonator was changed once. For this change the setup needed to be vented with air and the Helmholtz coils had to be dismounted and remounted. The reason behind this change of instruments was that in cavity 1 the contact springs were loose and the antennas had slightly different lengths. The consequences were that less power than expected could be transferred into the resonator. In cavity 2 these disadvantages were overcome by spot welded contact springs between the flanges and the usage of a stub tuner for a better coupling of the microwaves into the resonator.

For all sets  $I_{HC}$  were set to positive and negative polarities except set number 4 operated only with positive polarity.

Another critical investigation was the influence of the  $\mu$ -metal shielding. All series of measurements were performed with two layers of  $\mu$ -metal surrounding the cavity except series 7, where only one layer shielded away external magnetic fields.

Also of importance for comparison with the antihydrogen experiment is the diameter of the beam. For antihydrogen the beam has a diameter of the vacuum components (CF-100). For hydrogen on the contrary the sections were pumped differentially which established a reduction of background signals from the gas load. The last aperture providing the

differential pumping was exchanged to provide a bigger beam (aperture 2, smaller beam aperture: hole 4 mm, wall thickness 3 mm; bigger beam: pipe aperture with 100 mm length, 15 mm diameter). The expected two beam sizes, estimated by simple geometric extrapolation in the centre of the cavity, were 8 mm for sets 1-8 and 22 mm for sets 9 and 10.

Additionally the distances  $d_{ss}$  between the permanent sextupole magnets, which set the velocity of the beam, the temperature of the cold head, as well as the current in the superconducting sextupole were varied.

### 5.3.2 DAQ procedure

The transitions for a later extrapolation were measured at different currents in the Helmholtz coils. For a resonance curve measurement  $I_{HC}$  was set to one fixed value and the frequency points were also selected randomly. The idea behind this procedure was to average out possible drifts that could lead to a systematic shift, resulting e.g. from the instability of the gas flow, or efficiency of instruments, and average these effects out. After a resonance scan at a fixed  $I_{HC}$ , the following current setting was chosen in a random order.

For further discussions the following terms are defined to describe a specific hierarchy in the data taking process.

term	description
<i>cycle</i>	a <i>cycle</i> describes a single sweep through the frequency steps of a hyperfine spectrum, which has been performed in a random sequence.
<i>scan</i>	a <i>scan</i> is the repetitive data acquisition of <i>cycles</i> at fixed current in the Helmholtz coils. Every <i>scan</i> consists of $i$ <i>cycles</i> .
<i>set</i>	a <i>set</i> is a series of <i>scans</i> at different currents in the Helmholtz coils at the same setup conditions. Such a <i>set</i> finally is used to perform an extrapolation to zero field.

In figure 5.6 a structure chart of the DAQ program for taking a *scan* for a fixed Helmholtz current is displayed.

For the *sets* 1-3 the DAQ was not yet optimised therefore, here the time for taking data varied. For these *sets* we were not yet aware of, that the total counting rate yields better signals (less averaging time for smoother curves and better  $\chi^2$  see section 4.2). For these

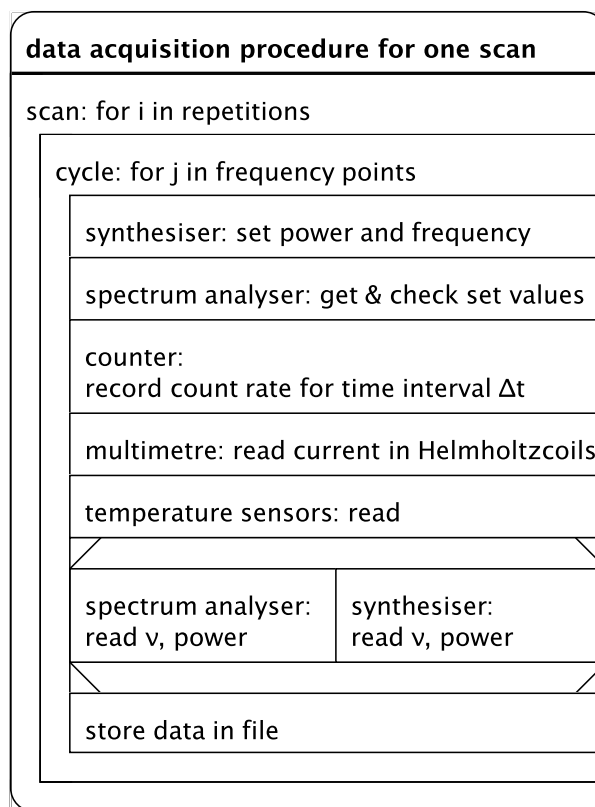


**Figure 5.6:** DAQ for recording a hyperfine transition. A *scan* consists of  $i$  *cycles* which again consist of  $j$  frequency points with associated count rate. During a *cycle* all slow control data (power and frequency synthesiser, power and frequency spectrum analyser, current in the Helmholtz coils, temperature sensors, fluxgate sensors, pressure sensors, see appendix figure A.1) are also digitised and therefore, every individual frequency point in a *cycle* has matching slow control documentation. The important slow control data are listed in the DAQ scheme.

*sets* the *scans* consisted of less *cycles* but the averaging time per *cycle* was longer (*set 1*: 60 s per frequency point; *sets 2 and 3*: 40 s per point.). Another difference is that in these *sets* the current in the Helmholtz coils was not yet digitised hence the error in current for these *sets* was assumed to be 1 mA (last digit of the reading of the power supply). In contrast to the first three data series, all other *sets* used the same averaging time (5 seconds per frequency point; more details on settings for all data *sets* can be found in appendix table A.1). The current was digitised with the Keithley multimeter (7½ digits resolution) and the average per *cycle* was calculated with the appropriate error. The errors associated with a counter signal were pure Poisson like (e.g. rate at the detector  $n \Rightarrow \sigma_n = \sqrt{n}$  [86]) and normalised to one second.

### 5.3.3 Flowchart of the analysis

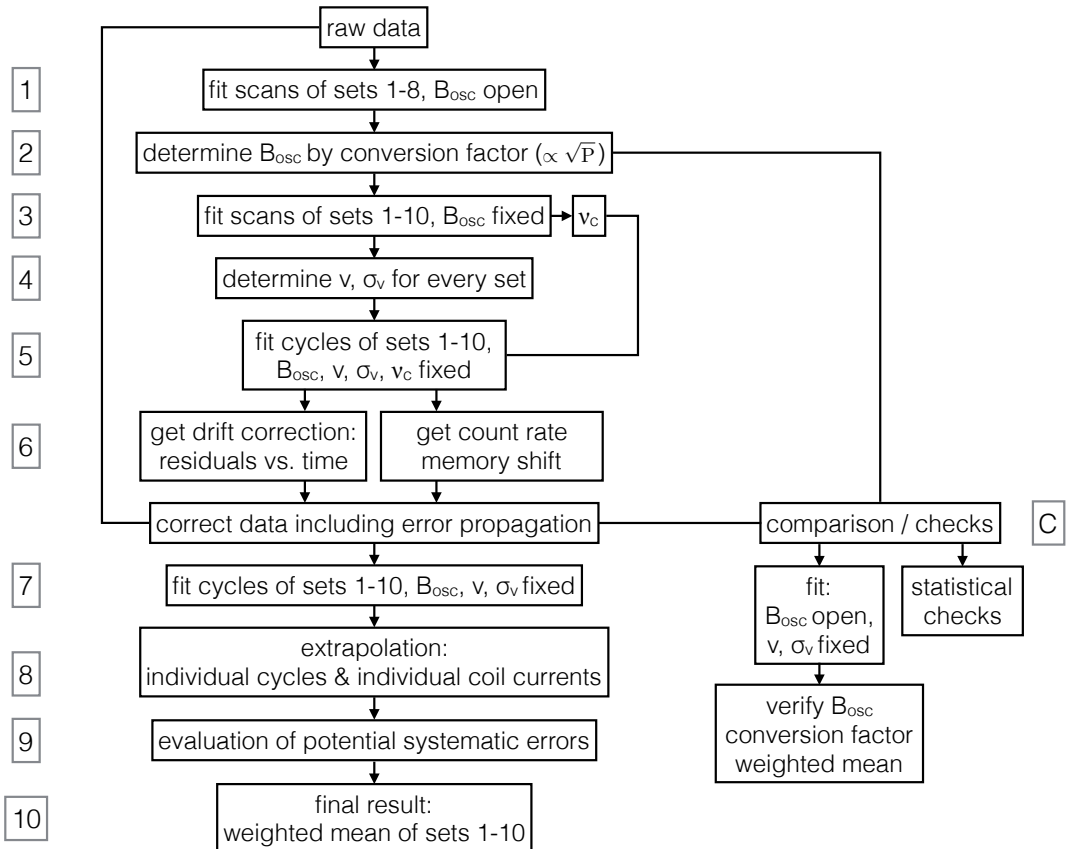
For reference and for an easier understanding of the next sections a flow chart of the analysis is presented at this point (see figure 5.7).

### 5.3.4 Power and $B_{\text{osc}}$ (flowchart step 2)

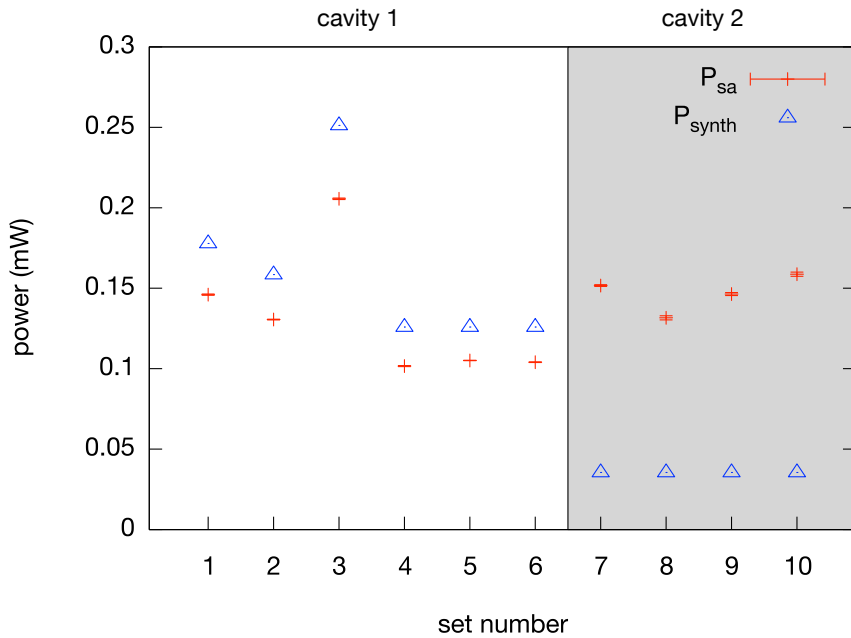
Every single measurement point in the data was recorded with its associated power value picked up with the spectrum analyser via an antenna port of the cavity ( $P_{\text{sa}}$ ). By comparing the output power of the synthesiser ( $P_{\text{synth}}$ ) and  $P_{\text{sa}}$  a clear difference in coupling of the microwaves to the first and second cavities could be identified. For both resonators the power values are compared in figure 5.8.

Figure 5.9 shows the ratio  $P_{\text{sa}}/P_{\text{synth}}$ . This graph demonstrates the improved coupling of the microwaves for cavity 2. Furthermore by comparing the  $\sqrt{P_{\text{sa}}}$  with the results for  $B_{\text{osc}}$  of the fits for the individual resonance curves, a linear relationship between the two quantities could be determined, as expected. Figures 5.10 and 5.11 show  $B_{\text{osc}}$  and  $\sqrt{P_{\text{sa}}}$  for all recorded transitions and as average for the ten *sets*. The data recorded with the bigger beam (*sets 9 and 10*) had a discrepancy when fitting with equation 4.4. The fit parameters correlated strongly ( $B_{\text{osc}}$ ,  $A$  and  $b$ ). Figures 5.10 and 5.11 indicate that for these *sets* the fitting routine found the  $B_{\text{osc}}$  at a non physical regime. Since the identified oscillating magnetic field from the fits follows the  $\sqrt{P_{\text{sa}}}$  values for the first 8 *sets*, it seems to be obvious that for *set 9 and 10* the real value for  $B_{\text{osc}}$  should also follow from the  $\sqrt{P_{\text{sa}}}$  dependence.

The factors for converting from the recorded power to an oscillating magnetic field were evaluated. Figure 5.12 shows two factors which were obtained from fit with a constant into



**Figure 5.7:** Flow chart of the analysis: 1: The *scans* are fitted with all fitting parameters open. 2: Get conversion factor for  $\sqrt{P_{sa}} \rightarrow B_{osc}$ . 3: Fit *scans* again with  $B_{osc}$  fixed for each *set*. 4: Determine the average velocities and velocity widths per *set*. 5: The individual *cycles* are fitted,  $B_{osc}$ ,  $v$ ,  $\sigma_v$  and  $\nu_c$  are fixed. 6: Corrections of the systematical effects of the raw data. C: Comparisons and checks. 7: After data corrections the *cycles* are fitted once more with fixed  $B_{osc}$ ,  $v$  and  $\sigma_v$  for each *set*. 8: For every *set* the extracted  $\nu_c$  values are used for an extrapolation to zero magnetic field to get values for  $\nu_0$ . 9: Evaluation of potential systematic errors 10: Final result with the weighted mean of all  $\nu_0$  values.



**Figure 5.8:** Power measured with spectrum analyser and synthesiser vs. set number. From set number 7 on the coupling inside the cavity was improved which leads to the leap in  $P_{\text{sa}}$  and therefore, less power was needed in the synthesiser ( $P_{\text{synth}}$ ).

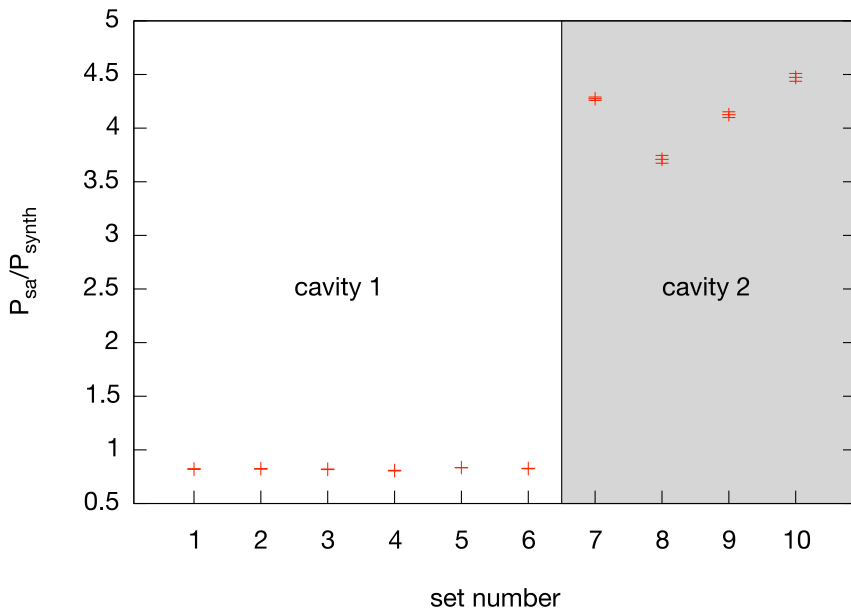


**Figure 5.9:** Ratio of the picked up power at the spectrum analyser and the power at the synthesiser. After improving the coupling in cavity 2 more power could be transferred.

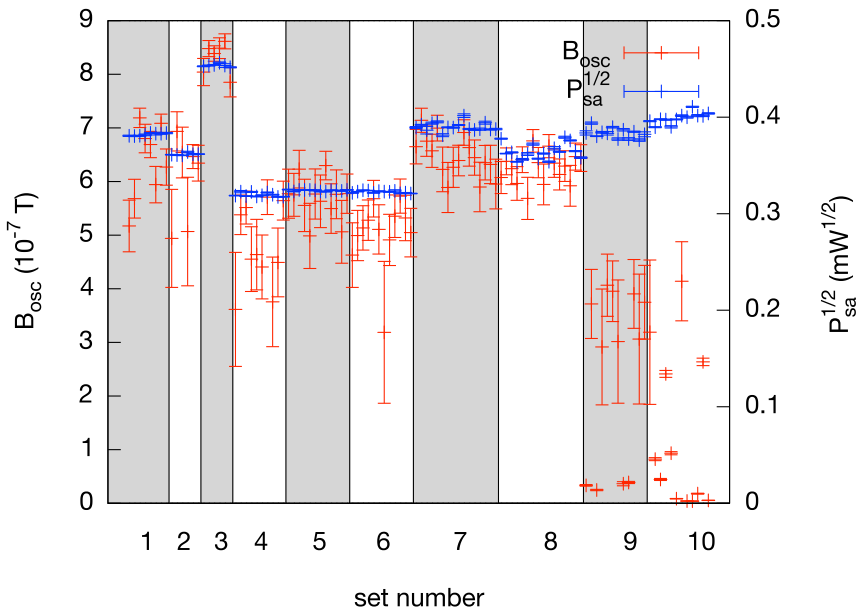


**Figure 5.10:**  $B_{\text{osc}}$  (left y-axis) and  $\sqrt{P}$  (right y-axis) vs. set number. The individual points from all sets are displayed. The values from the fit for  $B_{\text{osc}}$  and the values for  $\sqrt{P_{\text{sa}}}$  are proportional to each other except for set 9 and 10. The discrepancy in these data sets is most likely due to the bigger beam testing the cavity. For these sets the  $\chi^2$  was minimised where  $B_{\text{osc}}$  apparently had a nonphysical value due to correlation problems in the fits.

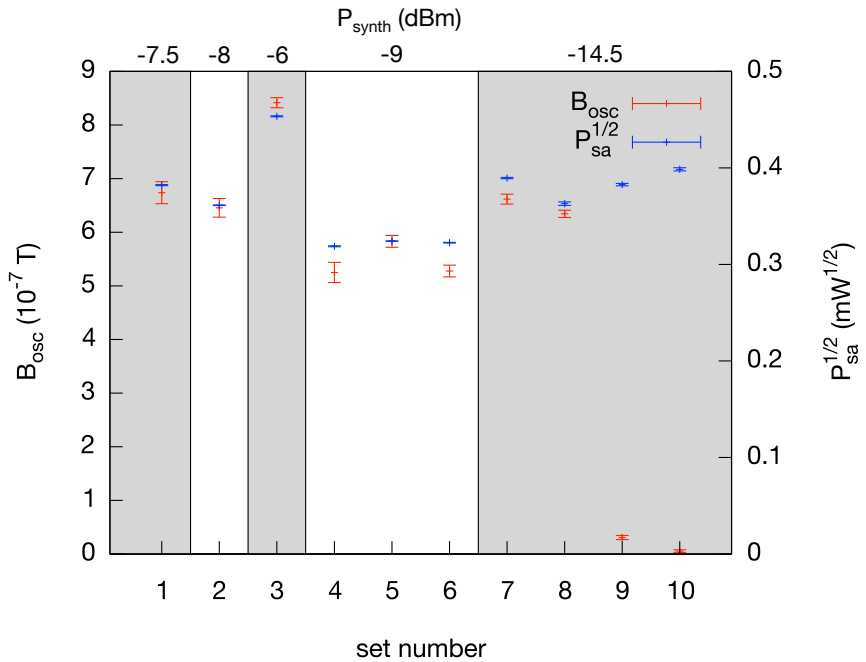


**Figure 5.11:** Once more  $B_{\text{osc}}$  (left Y-axis) and  $\sqrt{P}$  (right Y-axis) vs. *set* number (bottom X-axis). Top X-axis shows the adjusted power values at the synthesiser. In this figure the average values per *set* are displayed. As said in the previous plot there is a discrepancy between oscillating magnetic field and  $P_{\text{sa}}$  for *set* number 9 and 10. Here apparently the  $\chi^2$  of the fit was minimised at a wrong region.

$B_{\text{osc}}/\sqrt{P_{\text{sa}}}$  for cavity 1 and for cavity 2. The values could be applied to all measurements for fixing the fitting parameter  $B_{\text{osc}}$  including sets 9 and 10.

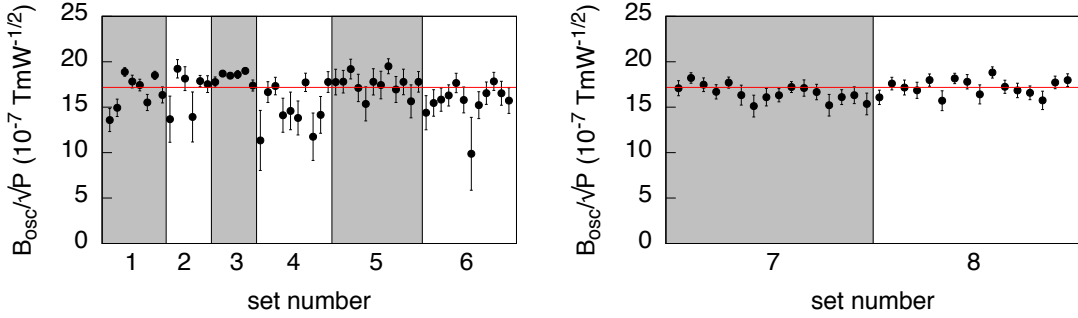


**Figure 5.12:** Conversion factor from  $\sqrt{P_{\text{sa}}} \rightarrow B_{\text{osc}}$  for cavity 1 (left picture) and cavity 2 (right picture). For both cavities and the according set scans a constant fit was applied with  $y(x) = d$  (=weighted mean). The conversion value from cavity 2 was later applied to the sets 9 and 10.  
 Cavity 1:  $\chi^2/n.d.f. = 129.5/53$ ,  $B_{\text{osc}}/\sqrt{P_{\text{sa}}} = (17.9 \pm 0.1) \times 10^{-7} \text{ T mW}^{-1}$ ;  
 Cavity 2:  $\chi^2/n.d.f. = 40.5/31$ ,  $B_{\text{osc}}/\sqrt{P_{\text{sa}}} = (17.2 \pm 0.1) \times 10^{-7} \text{ T mW}^{-1}$ ;

At this point it should also be checked that no unwanted correlation between  $B_{\text{osc}}$  and  $I_{\text{HC}}$  is present. In graph 5.13 it is shown for set 4 that this is not the case over a broad range of current steps.

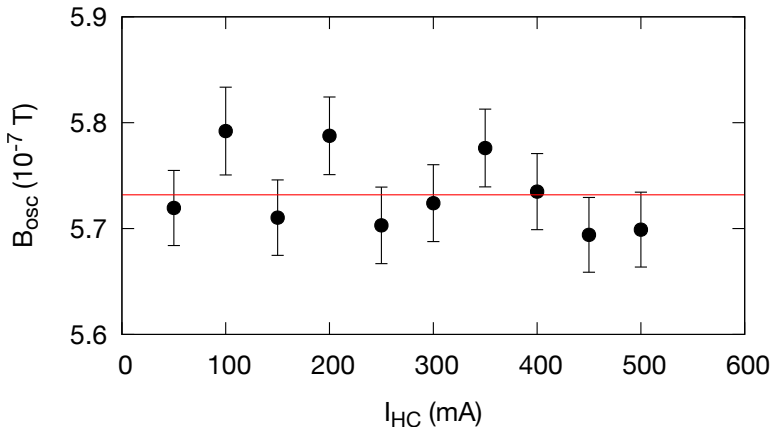


**Figure 5.13:** Search for nonlinear correlation between  $B_{\text{osc}}$  and  $I_{\text{HC}}$ .

### 5.3.5 Velocity and Velocity spread (step 4)

The velocity and the velocity spread of the beam were retrieved by equation 4.4 for every scan. The idea was to fix the velocity and velocity spreads per set to the average values

from the single *scans* since all settings were the same for *scans* within a *set* with exception of  $I_{HC}$ . To justify this procedure both quantities were fitted with  $y(x) = kx + d$  vs. time and respectively vs. current in the Helmholtz coils. The error on  $k$  was compared to the magnitude of  $k$  itself as a quantitative criterion. In general it was found that the error on  $k$  was larger than  $k$  itself. Therefore, a constant fit  $y(x) = d$  (= weighted mean) was applied and the velocities and velocity spreads were fixed to the average value for further fits. Figures 5.14 and 5.15 illustrate this procedure against time and against current in the Helmholtz coils for *set* number 4 (In appendix table A.2 a full list of the errors and  $\chi^2$  can be found).

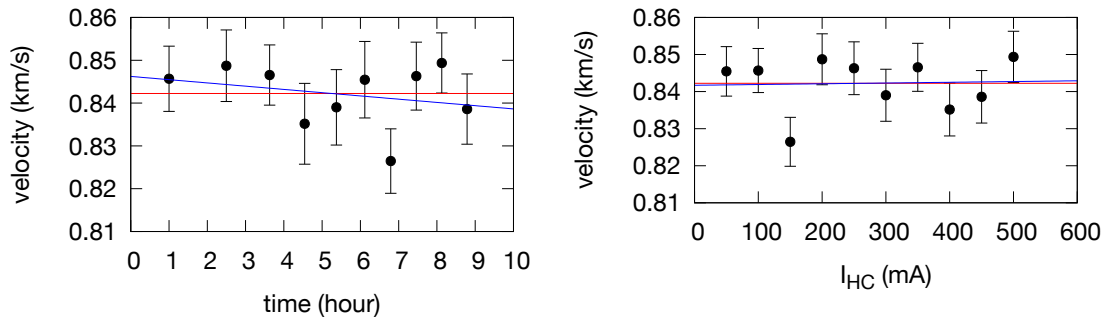


**Figure 5.14:** Justification for fixing velocity to weighted mean, blue lines  $y(x) = kx + d$ , red lines  $y(x) = d$ ;

left velocity vs. time:  $y(x) = kx + d$ :

$\chi^2/n.d.f. = 1.2$ ,  $k = -8(10) \times 10^{-4}$  ( $\triangle 125\%$  err),  $d = 0.846(6)$  ( $\triangle 0.7\%$  err)

right: velocity vs.  $I_{HC}$ :  $y(x) = kx + d$ :

$\chi^2/n.d.f. = 1.3$ ,  $k = 0.2(1.7) \times 10^{-5}$  ( $\triangle 838\%$  err),  $d = 0.842(5)$  ( $\triangle 0.6\%$  err)

$y(x)=d$  (weighted mean):  $\chi^2/n.d.f. = 1.2$ ,  $d = 0.842(2)$ , ( $\triangle 0.2734\%$  err)

### 5.3.6 Drift correction and count rate memory shift (step 6)

The raw data had to be corrected for two systematic effects: the count rate drift in time and a type of count rate memory effect. Both effects were investigated in parallel as they should not be correlated.

#### Drift correction

The time for recording a *scan* was long enough to show drifts in count the rate (typically about 40 minutes). Since the measurement points were recorded randomly in frequency, the drift is not visible directly in a resonance spectrum. Therefore, a method had to be invented where only the drift could be shown. It turned out that the best way of displaying

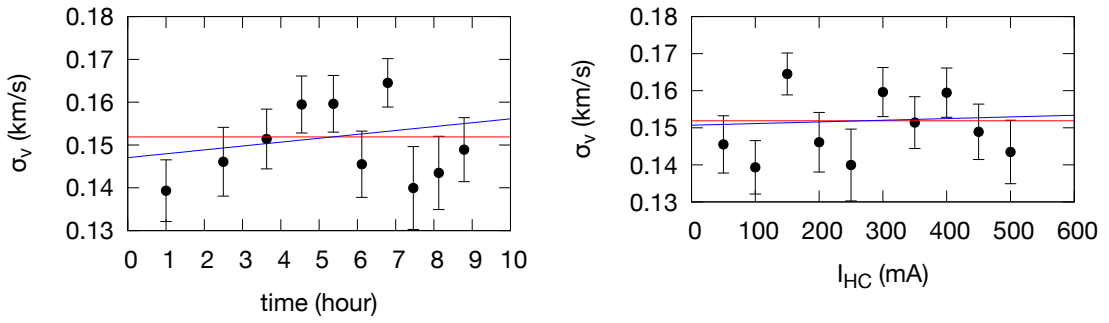


**Figure 5.15:** Justification for fixing  $\sigma_v$  to weighted mean, blue lines  $y(x) = kx + d$ , red lines  $y(x) = d$ ;  
 left:  $\sigma_v$  vs. time:  $y(x) = kx + d$ :  
 $\chi^2/n.d.f. = 1.7$ ,  $k = 9(13) \times 10^{-4}$ , ( $\triangle 144\%$  err),  $d = 0.147(8)$ , ( $\triangle 5\%$  err)  
 right:  $\sigma_v$  vs.  $I_{HC}$ :  $y(x) = kx + d$ :  
 $\chi^2/n.d.f. = 1.8$ ,  $k = 0.4 \pm 2.2 \times 10^{-5}$  ( $\triangle 491\%$  err)  $d = 0.151 \pm 0.007$ , ( $\triangle 4\%$  err)  
 $y(x) = d$  (weighted mean):  $\chi^2/n.d.f. = 1.6$ ,  $d = 0.152(3)$ , ( $\triangle 2\%$  err)

the drift is by plotting the residuals against time. As usual, the residuals were calculated the following way:

$$r_i = y_i - \mathcal{F}(\nu_i) \quad (5.5)$$

where  $r_i$  is the residual,  $y_i$  the detector count rate, and  $\mathcal{F}(\nu_i)$  is the result of equation 4.4 evaluated at the frequency  $\nu_i$  for the measurement point  $i$  [87]. An obvious *scan* showing a drift is illustrated in figure 5.16. An interesting fact is that when analysing the data with residuals vs. the excitation frequency  $\nu_c - \nu_{lit}$  no drift is visible. This behaviour is due to the fact that the measurement points were recorded in a random sequence across the frequency points and therefore, the frequency is decoupled from the drift.

Various ways of correcting the drift were investigated such as e.g. correcting with the information from the temperature sensors  $T_i$  or the chopper frequency. The problem was that a drift was also visible in the temperature sensors but the residuals did not correlate. This behaviour led to the conclusion that a correlation with temperature exists but since the reaction of the system is slow the information for drift correction could not be applied in time. A more quantitative statement for not using the temperature sensors is shown in figure 5.17. For the *sets* 4 - 10 the mean slopes of the standard scores  $z_i$ , which are the residuals normalised by the standard deviation ( $z_i = r_i/\sigma_i$ ) [87], and the slope of the temperature sensors are plotted against each other. The standard scores are used instead of the residuals since the normalised residuals make the different *sets* comparable. The

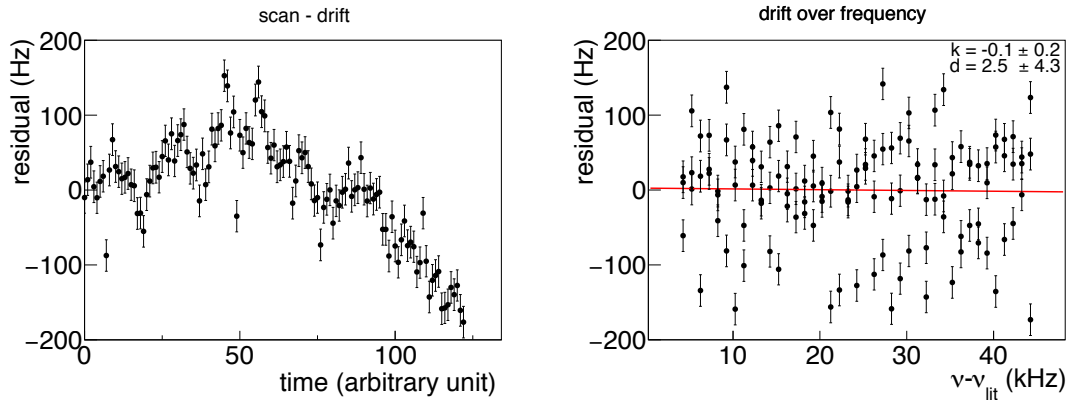


**Figure 5.16:** Left: Drift for *set 1*,  $I_{\text{HC}} = 615$  mA; for a better estimation of the drift the residuals extracted from a *scan* were plotted vs. time. One time period corresponds to 60 seconds; Right: residuals vs. the excitation frequency at the synthesiser. As can be seen in this graph the overall *cycles / scans* are decoupled of the drift. The red curve shows a linear fit into the data with  $y = kx + d$ ,  $k = -0.1 \pm 0.2$ ,  $d = 2.5 \pm 4.3$

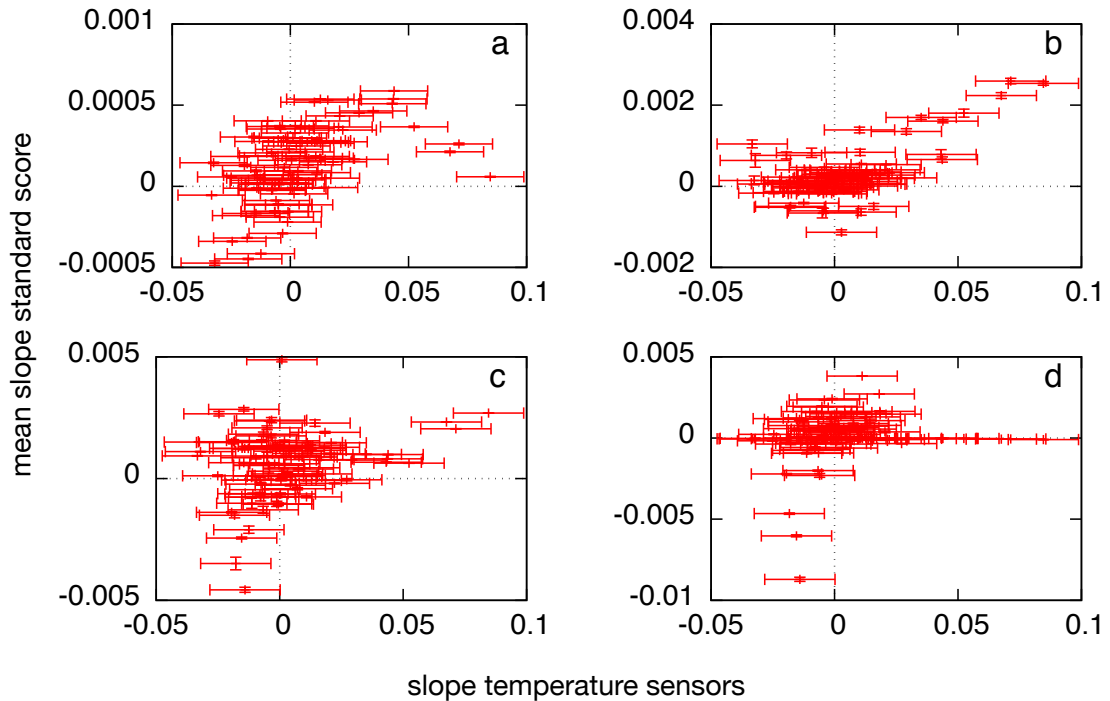


**Figure 5.17:** Slope comparison between standard scores  $z_i$  and slope of the sensors. No obvious correlation can be detected. a: temperature sensor was attached to fluxgate sensor 2 inside the shielding; b: sensor was attached inside the shielding; c: sensor was attached to externally on top of the magnetic shielding; d: sensor was attached next to the QMS.

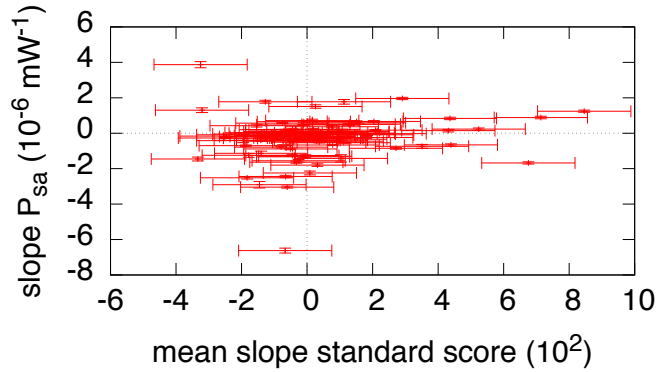


**Figure 5.18:** Slope comparison of the power picked up with the spectrum analyser with the standard score. No obvious correlation is visible.

slopes were obtained from linear fits in time. The fitting function for the  $z_i$  was  $z_i = kt + d$  and for the  $T_i$  the fitting function was  $T_i = kt + d$ . The plot shows the difficulty whether to use a temperature sensor for correction. It seems for all sensors that the signals are not correlated in time. The situation was similar when comparing the drift of the power  $P_{sa}$  in time with the standard score. The fitting function for the slopes was  $P_{sa\,i} = kt + d$ . By comparing the slopes also here no correlation was present (figure 5.18). Therefore, another way for the correction of the drift had to be conceived. The simplest way to perform a correction was to use the *cycles* instead of the *scans*. For a *scan* of  $i$  *cycles* the time  $t$  of data taking obviously was  $t/i$  and the time periods are short enough to show a linear drift (see figure 5.19). Therefore, this drift was corrected linearly in residuals vs. time. The idea behind this model was that for a linear drift correction the data would be corrected without distorting the shape too much. To get the *cycle* residuals for the corrections the *cycles* were fitted with  $B_{osc}$ ,  $v$ ,  $\sigma_v$  fixed in the way as explained in the before mentioned sections. Furthermore, in order not to change the shape of the signal also the centre frequencies  $\nu_c$ , which were extracted from the *scan* fits, were fixed (see flow chart). For these fits only the amplitude and the baseline were kept as open parameters. Finally for the corrections the slopes from the drift fit were used to correct the raw data. Since the slopes are associated with errors the Poisson errors had to be increased using error propagation.

However, the random sequences applied in data taking have successfully averaged out the effect of the drift and the results did not change significantly. The  $\chi^2$  improved by the corrections can be compared at table 5.3.

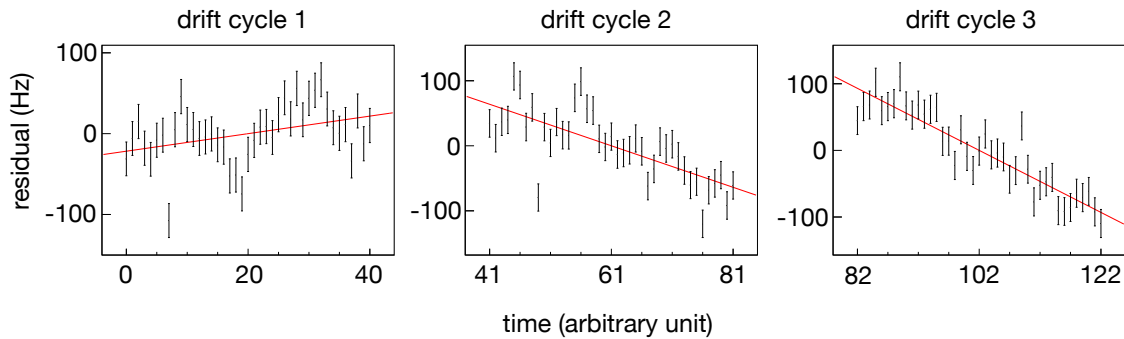


**Figure 5.19:** Drift correction in *cycles*; same measurement as figure 5.16; a drift correction was estimated with a linear fit into the residuals of the *cycles*. One time period corresponds to 60 seconds. The residuals  $r_i$  were obtained by  $r_i = y_i - \mathcal{F}(\nu_i)$ , where  $\mathcal{F}$  is the fitting function with fixed parameters as shown in the flow chart 5.7 step 5.

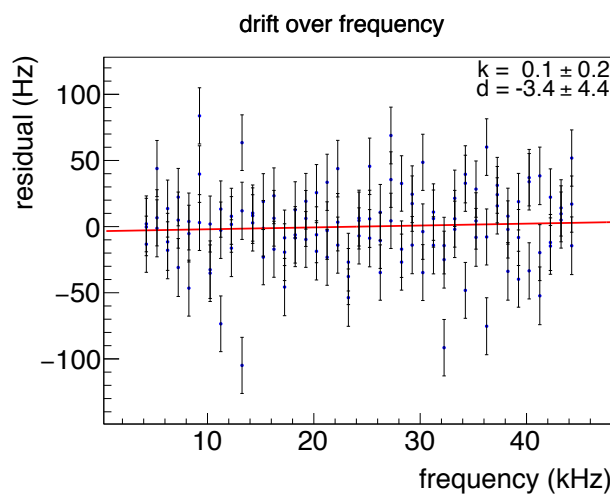


**Figure 5.20:** Check of drift in frequency after drift corrections (again *set 1*,  $I_{HC} = 615$  mA). For this spectrum the residuals of the individual *cycles* were plotted against the excitation frequency and a linear fit  $y = kx + d$  was applied.  $k = 0.1 \pm 0.2$ ,  $d = -3.4 \pm 4.4$ .

### Count rate memory shift

Another systematical effect that was corrected for in parallel to the drift was an effect which we called count rate memory shift (cms). This shift can be best explained with figure 5.21. Because of the random sequence of jumps between frequencies, higher or lower count rates are observed. The recorded count rate at a certain frequency point will be higher/lower if the previous frequency point was taken at a higher/lower count rate. The reason is, that the hydrogen beam increases the gas load in the detection chamber and the relaxation time is not instant enough to render this memory effect insignificant. Certainly the relaxation time is large compared to the chopper frequency, which explains the clear difference between count rate drop in beam rate and total count rate.

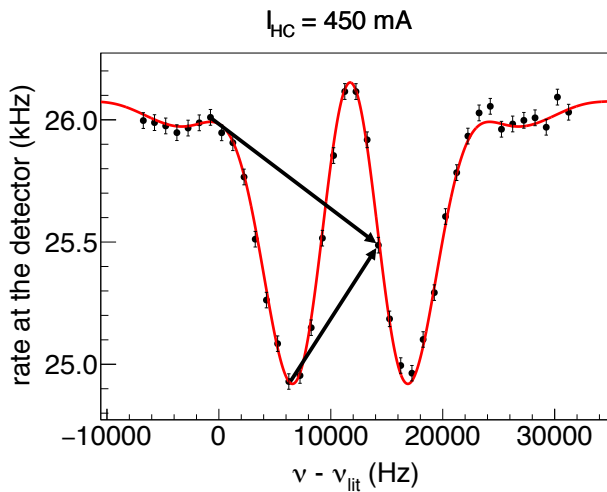


**Figure 5.21:** Explanation of the count rate memory shift in a *scan* (set 6,  $I_{HC} = 450$  mA). If the measurement before was done at a higher count rate, higher gas load will be in the ionisation housing of the QMS, if the measurement before was a lower count rate, less gas load will be in the ionisation chamber.

By plotting the residuals against the difference in count rate of two subsequently measured frequency points (count rate( $t_i$ )-count rate( $t_{i+1}$ )) the effect can be quantified. The residuals were evaluated the same way as described in the drift corrections. The cms then was fitted linearly (see figure 5.22 which is the overall cms of *scan* 5.21). The error on the zero offset  $d$  was much higher than the actual value for  $d$  which was the argument to not use  $d$ . The slopes  $k$  of all measured transitions per *set* were used to obtain a correction factor for this shift (weighted mean of the slopes → see figure 5.23). As can be seen the effect is rather small (for *sets* 1-3 even smaller since there measurement per frequency point was longer and an additional/smaller gas load at the beginning of a measurement was

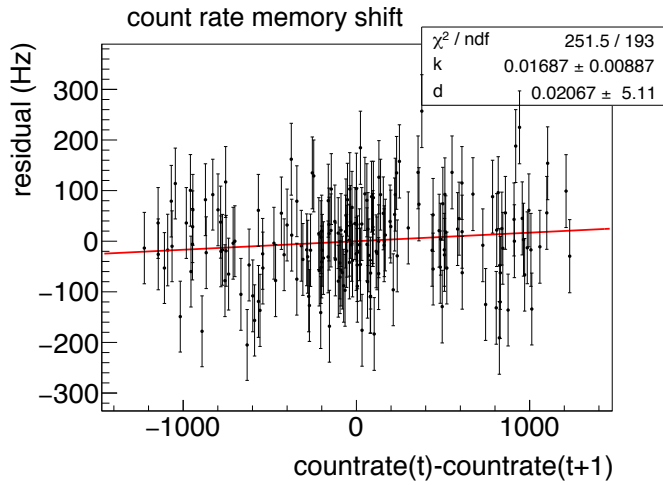


**Figure 5.22:** Count rate memory shift  $k$  for one *scan* (*set 4*,  $I_{HC} = 450$  mA); the value for the shift was obtained from a linear fit ( $y(x) = kx + d$ ) into residuals vs. count rate difference in time. Only  $k$  is used since for  $d$  the errors are larger than the value itself.

less critical). This is most likely because the program had a break of 2 seconds between the measurements to store slow control data. Table 5.2 shows the cms values for all *sets*. After correcting the raw data the errors also here had to be changed with error propagation.

**Table 5.2:** The weighted mean count rate memory shift factors for all *sets*.

set	$\chi^2$	n.d.f.	cms
1	17.0	7	0.007(2)
2	5.4	5	0.014(4)
3	3.4	5	0.007(2)
4	5.5	9	0.013(3)
5	10.9	11	0.051(4)
6	3.9	11	0.016(2)
7	11.1	15	0.026(3)
8	11.0	15	0.016(2)
9	13.3	11	0.007(1)
10	15.9	11	0.006(1)

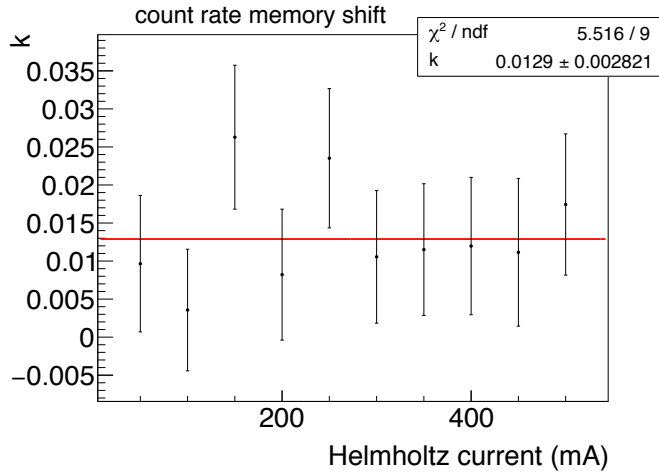


**Figure 5.23:** Weighted mean of the cms factors for *set 4*. Per *set* one factor was obtained and used for the corrections.

### 5.3.7 Comparison and checks (step C)

#### Checks of $B_{\text{osc}}$

After applying the correction to the raw data and introducing the associated errors the conversion factor from  $\sqrt{P_{\text{sa}}} \rightarrow B_{\text{osc}}$  had to be rechecked. The analysis of the factor was done analog to chapter 5.3.4 with the difference that the systematical effects were compensated at the raw data, errors adjusted, velocity and velocity spread still fixed. Since the value for the factor did not change, the corrections were accepted.

**Table 5.3:** After these systematic effects were corrected for, checks whether  $B_{\text{osc}}$  has changed needed to be done. As can be seen the conversion factor from  $\sqrt{P_{\text{sa}}} \rightarrow B_{\text{osc}}$  did not change. The reduced  $\chi^2$  ( $\chi^2/n.d.f.$ ) get closer to unity for two reasons. Firstly the residuals become smaller by applying the correction. Secondly and more importantly, the error bars on the raw data increased due to the introduced error propagation.

	$\sqrt{P_{\text{sa}}} / B_{\text{osc}}$ pre corr. ( $10^{-7} \text{ TmW}^{-1/2}$ )	$\chi^2 / n.d.f.$	$\sqrt{P_{\text{sa}}} / B_{\text{osc}}$ post corr. ( $10^{-7} \text{ TmW}^{-1/2}$ )	$\chi^2 / n.d.f.$
cavity 1	17.9(1)	129.5/53	17.9(1)	121.0 / 53
cavity 2	17.2(1)	40.5/31	17.2(1)	32.9 / 31

## Statistical properties

After the systematical effects were corrected some more systematical checks showed that for the final fit of the resonance curves the residuals were evaluated correctly. First a histogram of the standard scores per  $I_{HC}$  by using all points of the *cycle* fits had as expected a gaussian like shape (an example can be seen in figure 5.24).

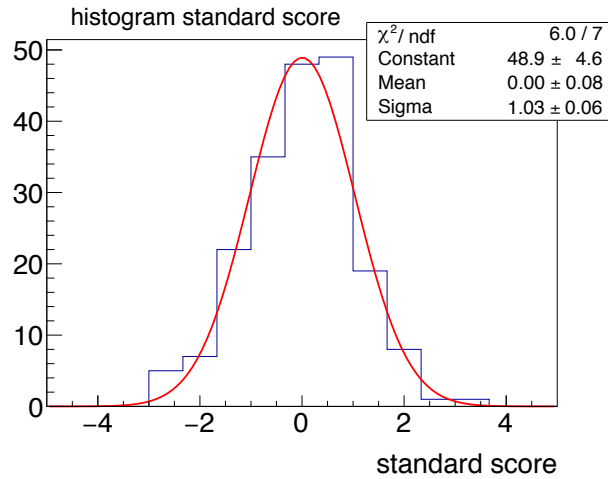


**Figure 5.24:** Histogram of the standard scores for *set 4*,  $I_{HC} = 450$  mA; a gaussian fit shows that the mean of the standard scores is around 0 (this fit  $\mu = 0.00 \pm 0.08$ ); another property is that the sigma of the fit is close to 1 (this fit  $\sigma = 1.03 \pm 0.06$ ) (as it should be for the standard scores).

After having the gaussian information another helpful statistical tool to check if a data sample is normal distributed - a QQ plot - could be applied (see figure 5.25). In a QQ plot the empirical quantiles of the data are compared with the theoretical ones (e.g. fitting curve figure 5.24). If the data is located around the diagonal it follows that the empirical distribution follows the theoretical one [87].

Since no bigger discrepancy was found, the residuals of the fit seem to be evaluated correctly. Therefore, it is legitimate to use the extracted values of function 4.4 for further processing.

### 5.3.8 Extended fitting function for larger beam diameter

An important step towards the measurements with an antihydrogen beam are testing the cavity at the full CF-100 volume with hydrogen. With the bigger aperture approximately a third of the cavity diameter could be tested. However, the data recorded with the bigger aperture had some discrepancy when fitting with equation 4.4. The fit parameters

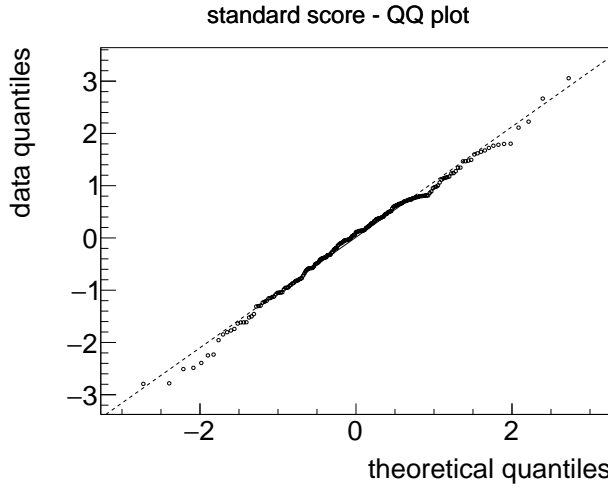


**Figure 5.25:** QQ-plot for set 4  $I_{\text{HC}} = 450$  mA; The data of all *cycles* are added into the histogram 5.24, then the quantiles of the empirical data and the theoretical ones are compared. Since the data is scattering around the diagonal the residuals of the fits seem to be chosen correctly. Therefore, the fitting function 4.4 was chosen for further processing.

correlated strongly ( $B_{\text{osc}}$ ,  $A$  and  $b$ ). As the microwave power was monitored using a pick-up antenna and a spectrum analyser (figure 3.6) the measured microwave power  $P_{\text{MW}}$  which is proportional to  $B_{\text{osc}}^2$  was used to fix this fit parameter. A second discrepancy was that the  $\chi^2$  of the fits were minimal where  $B_{\text{osc}}$  had nonphysical values. An interpretation of this behaviour is that the fitting function for these *sets* does not describe the data physically correct. This effect most likely results from the bigger beam testing the cavity since this was the change in the setup.

An idea for fixing this problem was to take the inhomogeneity of the external field (produced by the Helmholtz coils) into account. In principle the magnetic field provided by the Helmholtz coils not necessarily is fully homogeneous. Inhomogeneities in space depending on the probed volume (bigger beam size for *sets* 9 and 10), inhomogeneities depending on the level of the current but also a general inhomogeneity of the coils could be present. All these aspects would result in a broadening of the Zeeman splitting, which would depend on the magnitude of the magnetic field. The current in the Helmholtz coils is proportional to the magnetic field, thus, depending on the value of  $I_{\text{HC}}$  the B-field inhomogeneity  $\sigma_B$  should yield different sizes for a frequency inhomogeneity which for now will be called  $\sigma_\nu$ . This effect is illustrated in fig. 5.26 (a), where for the extrapolation curve 5.4 this effect of  $\sigma_{I_{\text{HC}}}$  on  $\sigma_\nu$  is shown. For higher  $I_{\text{HC}}$  the same current inhomogeneity  $\sigma_{I_{\text{HC}}}$  results in higher values for  $\sigma_\nu$ .

One way to test the goodness is by convoluting equation 4.4 with a frequency inhomogeneity. Since no information on a distribution of an inhomogeneity is available the first idea is to assume a gaussian distribution. The convolution was done the following way:

$$\begin{aligned}\mathcal{F}_{\sigma_\nu}(\nu, \sigma_\nu; B_{\text{osc}}, \nu_c, v, \sigma_v, A, d) &= h(\nu) * \mathcal{F}(\nu) \\ &= h(\nu; \sigma_\nu) * \mathcal{F}(\nu; B_{\text{osc}}, \nu_c, v, \sigma_v, A, d)\end{aligned}\quad (5.6)$$

where  $\mathcal{F}_{\sigma_\nu}$  is the convoluted fitting function,  $h(\nu; \sigma_\nu)$  is a gaussian function which was once more approximated due to computing time with binomial coefficients, and  $\mathcal{F}$  is the original fitting function.

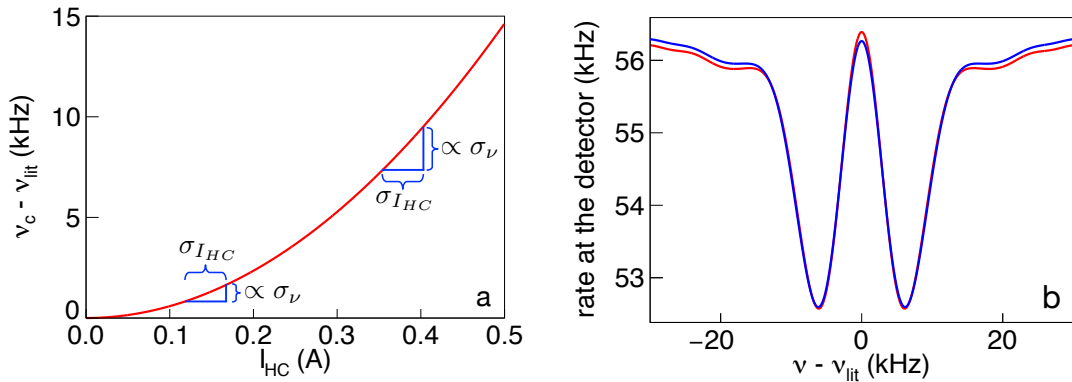


**Figure 5.26:** (a) illustration of the influence of a fluctuation of the current  $I_{\text{HC}}$  on  $\sigma_\nu$  in the zero-field extrapolation curve. Due to the parabolic shape of the curve at higher current an inhomogeneity will yield a higher  $\sigma_\nu$ . (b) illustration of the effect of  $\mathcal{F}_{\sigma_\nu}$  (blue) on the line shape and comparison with the original line shape (red). For plotting the function the average values from *set 9* were taken for the convoluted and the original fitting function.

The effect of the new function on the line shape compared with the old function is displayed in figure 5.26 (b). The result for  $\sigma_\nu$  for the fits is shown in 5.27. The displayed results were obtained by fitting the *cycles* (after the systematic corrections of drift and count rate memory shift, fixed  $B_{\text{osc}}$ ,  $v$ , and  $\sigma_v$  - see flow chart 5.7 - instead of step 7). For every *set* per current in the Helmholtz coils the weighted mean of the *cycles* has been calculated. The plot shows that consistently in *set 9* and *10* values of about 1000 Hz were found whereas for *sets 1-8* the obtained values are smaller. Especially in these *sets* the  $\chi^2$  of the fit improved (*set 9*: no  $\sigma_\nu$   $\rightarrow$  average  $\chi^2/n.d.f. = 1.9 \pm 0.4$ ; including  $\sigma_\nu$   $\rightarrow$  average  $\chi^2/n.d.f. = 1.6 \pm 0.4$ ; *set 10*: no  $\sigma_\nu$   $\rightarrow$  average  $\chi^2/n.d.f. = 1.9 \pm 0.4$ ; including  $\sigma_\nu$   $\rightarrow$  average  $\chi^2/n.d.f. = 1.5 \pm 0.3$ )

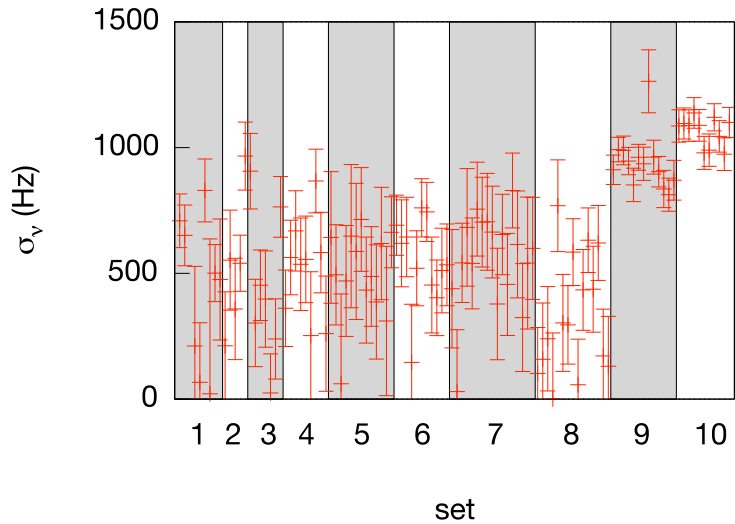


**Figure 5.27:** Cycle weighted mean of the fit results for  $\sigma_\nu$ . As can be seen for *set 9* and *10* the convolution finds consistently values deviating compared to the other *sets*.

When looking at plots of  $\sigma_\nu$  vs.  $I_{HC}$  for the *sets* 9 and 10 (see figure 5.28 a and b) the parabolic structure as described in 5.26 (a) could not be observed. For *set 9* the slope of the parabola fit is negative and for *set 10* the curvature is positive. No clear positive curvature as would be expected is visible.

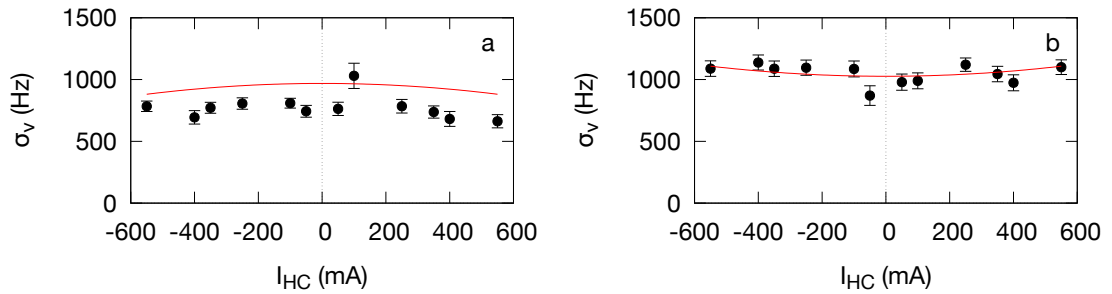


**Figure 5.28:** The values for  $\sigma_\nu$  plotted against the current in the Helmholtz coils for (a) *set 9* and (b) *set 10*. No obvious parabolic structure can be seen (red line : fit  $y(x) = kx^2 + d$ ).

Instead of the  $\sigma_\nu$  inhomogeneity a Helmholtz current depending inhomogeneity could be present and yield a constant  $\sigma_\nu$ . But as shown in figure 5.29 also here no parabolic structure can be observed for *sets* 9 and 10. Additionally the  $\sigma_\nu$  weighted means for the values of figure 5.27 are displayed in figure 5.30. Clearly the parameter is sensitive to an effect that differs for the small and large hydrogen beam diameter.

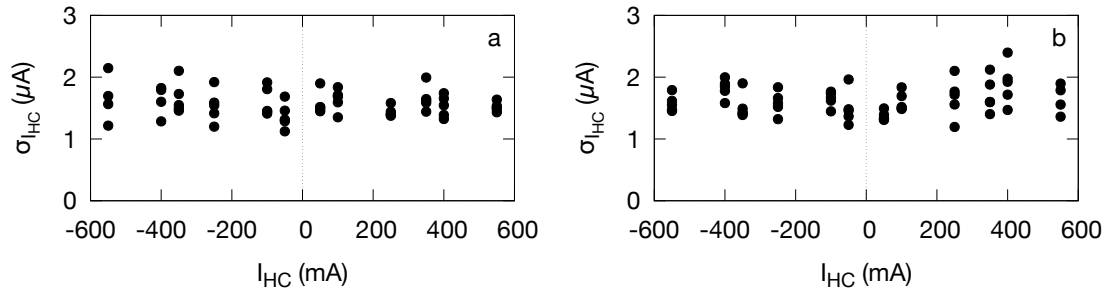


**Figure 5.29:** Check that current error  $\sigma_{I_{HC}}$  does not have clear parabolic structure which would counteract the inhomogeneity effect ( $\sigma_{I_{HC}}$  calculated as standard deviations of  $I_{HC}$  per cycle).

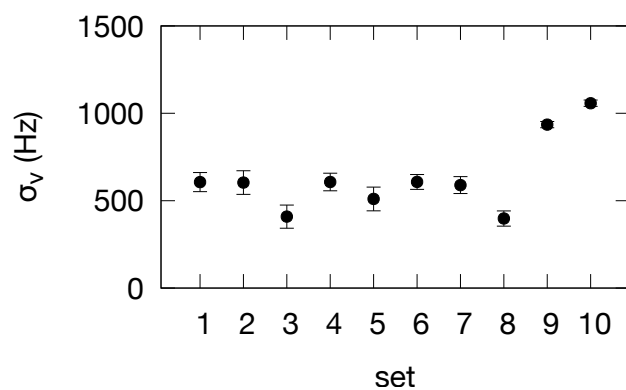


**Figure 5.30:** Since the parabolic effect does not seem to be present the weighted mean of  $\sigma_v$  per set was calculated. For sets 9 and 10 higher values were found.

In conclusion it was decided not to use the  $\sigma_\nu$  results for the following, where some more systematical investigations are considered. The reason as explained before is that the fitting parameter does not show the expected dependencies e.g.  $B_{\text{osc}}$  did not perform as expected for *set* 9 and 10 and yet it is unknown which effect would yield to a constant  $\sigma_\nu$ .

### 5.3.9 Extrapolation to zero magnetic field (step 8)

After all these considerations the values for the  $\sigma_1$  transition frequencies and their according magnetic field expressed by the current in the Helmholtz coils could be used to extrapolate to zero magnetic field. As mentioned at the beginning of this chapter equation 5.4 was used for performing a fit of these data and obtaining the zero field ground state hyperfine splitting. Figure 5.31 shows such an extrapolation, where all the values of  $\nu_c$  and  $I_{\text{HC}}$  obtained from the *cycle* fits are used to perform the extrapolation. Note that the graph involves errors in x and y direction.

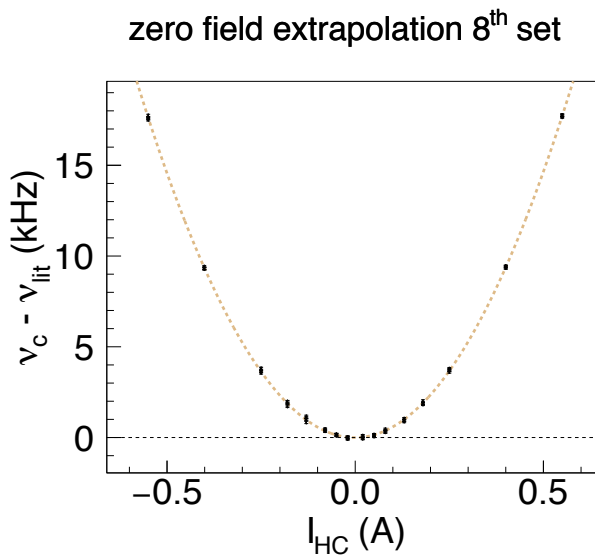


**Figure 5.31:** Zero field extrapolation; *set* number 8,  $\chi^2/n.d.f. = 82.4/77$ , deviation  $\nu - \nu_{\text{lit}} = -3.4 \pm 9.1 \text{ Hz}$ ,  $B_0 = (3.5 \pm 1.1) \times 10^{-7} \text{ T}$ ,  $C = (45.90 \pm 0.02) \times 10^{-5} \text{ T/A}$ .

Graph 5.32 shows how the reduced  $\chi^2$  of the extrapolations and also the mean reduced  $\chi^2$  for the resonance fits of the *sets* scatter. It can be seen that on average the  $\chi^2$  of the individual transition measurements are higher than the ones of the extrapolations. Nevertheless, since during data acquisition the frequency points were recorded randomly the bigger  $\chi^2$  has most likely no impact on the extrapolations.

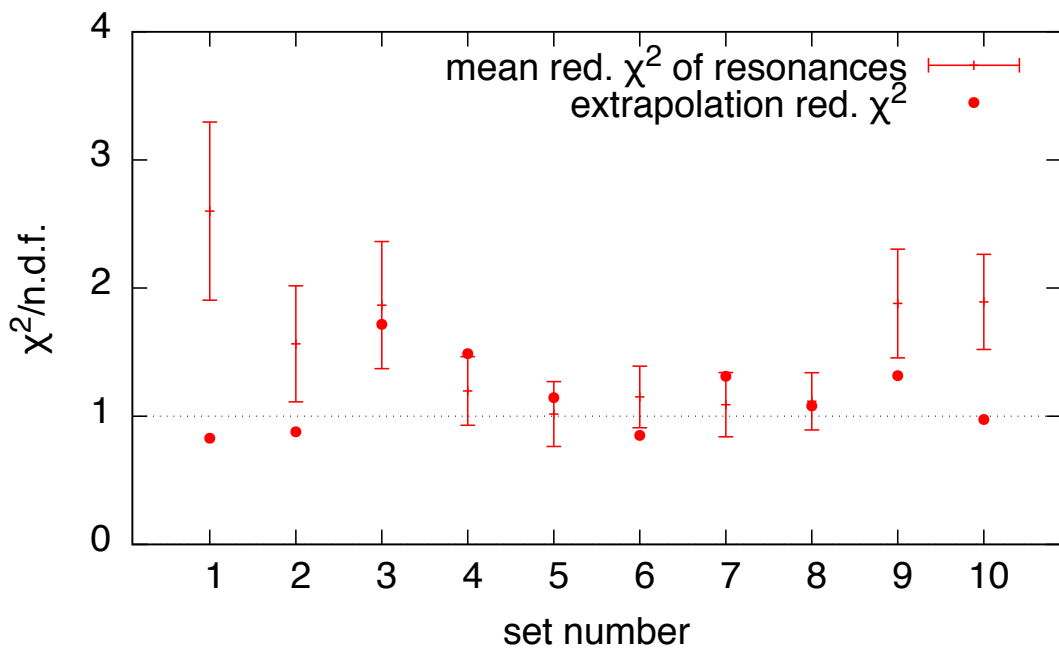


**Figure 5.32:** Average cycle fit  $\chi^2$  (therefore, including error bars) and  $\chi^2$  of the extrapolations.

For *sets* 1-3 it is obvious that the transition  $\chi^2$  is bigger since the DAQ procedure was not yet optimised. For *sets* 9-10 as already mentioned there seems to be another yet unknown effect increasing the  $\chi^2$ . All in all the reduced  $\chi^2$  of the extrapolations scatter around 1 and thus, it can be assumed that the analysis was performed correctly.

### Benchmark - comparison of methods

Next a benchmark test should be shown to see the changes between the steps in the analysis. Figure 5.33 shows the reduced  $\chi^2$  for the various steps. The illustrated analysis steps are:

- $B_{\text{open}}$ :  $B_{\text{osc}}$  not fixed fitting parameter, the *scans* were fitted.
- $B_{\text{fixed}}$ :  $B_{\text{osc}}$  fixed by  $\sqrt{P} \rightarrow B_{\text{osc}}$ , *scans* fitted.
- *Cycle* fit:  $B_{\text{osc}}, v, \sigma_v$  fixed and *cycles* fitted.
- $\sigma_\nu$  included: the frequency smear  $\sigma_\nu$  included with systematical effects of drift and count rate memory shift corrected,  $B_{\text{osc}}, v, \sigma_v$  fixed .
- Final analysis: systematical effects of drift and count rate memory shift corrected,  $B_{\text{osc}}, v, \sigma_v$ . fixed

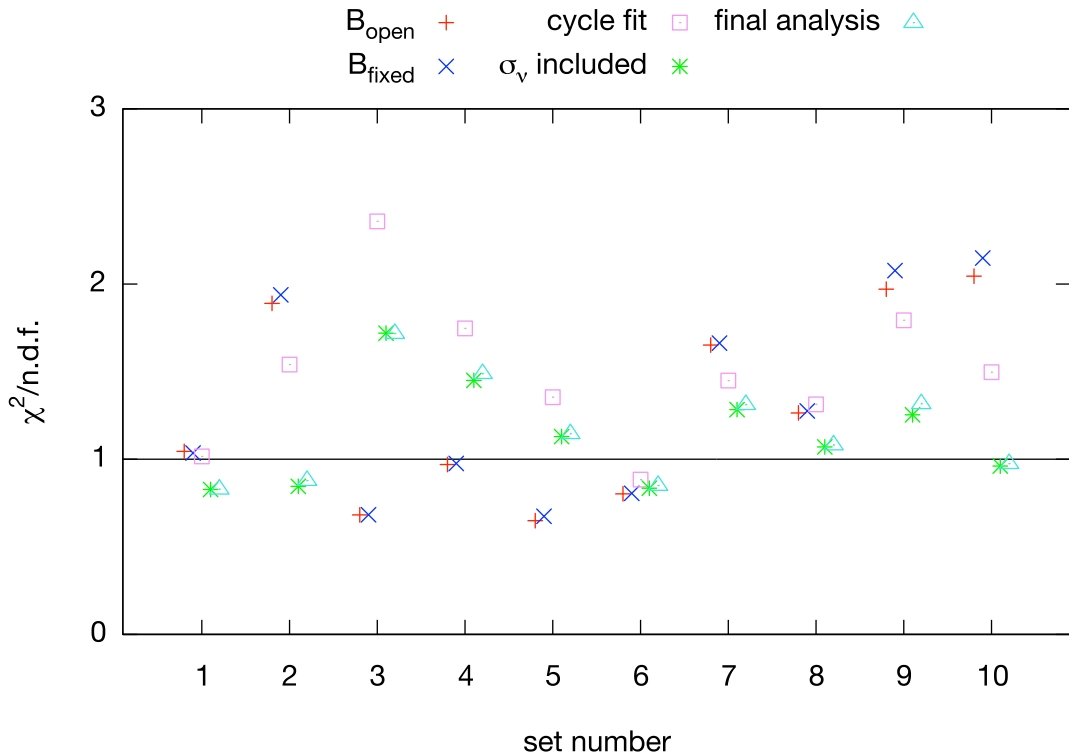


**Figure 5.33:** Reduced  $\chi^2$  comparison of the different methods/steps in the analysis.

The correction apparently improved for all *sets* the  $\chi^2$  (closer to 1) only for *sets* 3 and 4 the  $\chi^2$  got worse. Figure 5.34 shows the changes for these methods in the extracted zero

field values and error bars. In most cases the changes are rather small. The biggest changes are in the first three *sets*.

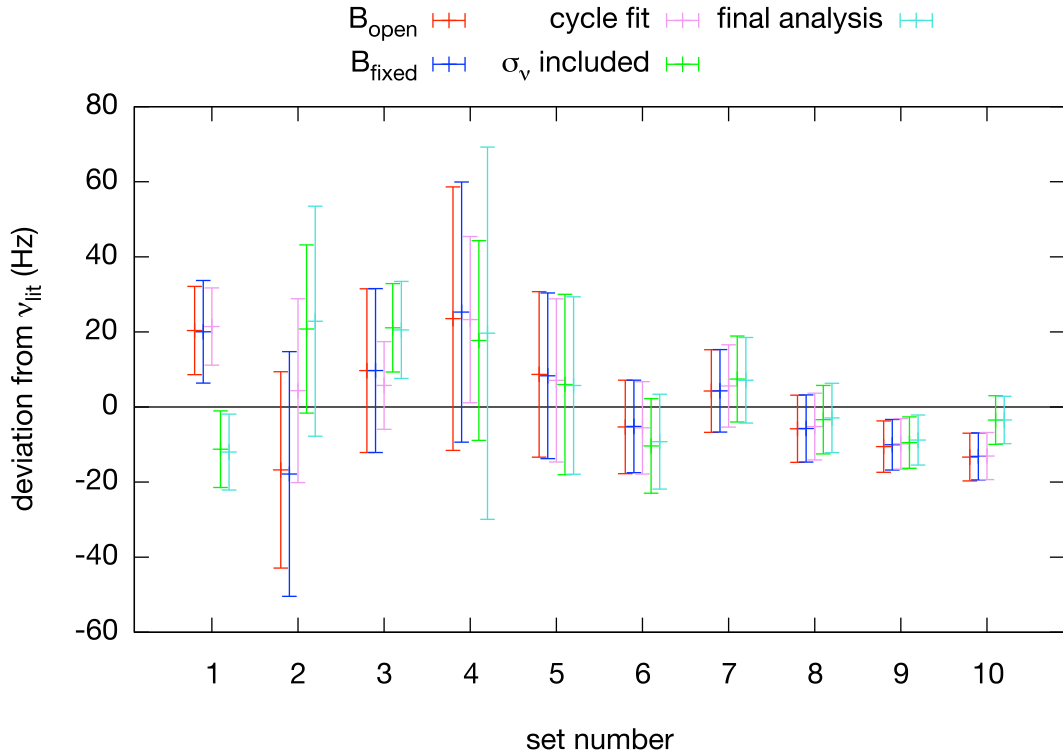


**Figure 5.34:** Extracted frequency for the hyperfine structure comparison for different methods/steps in the analysis.

## 5.4 Evaluation of potential systematic errors (step 9)

In this section systematical checks of the analysis are shown. The checks are divided into three groups, one dealing with the stability of  $I_{HC}$ , one dealing with the fitting parameters and the third where the parameters are grouped in a way representative for bigger changes in the settings of the setup.

### 5.4.1 Current stability

The current in the Helmholtz coils is one parameter, where the drifts as sources of potential systematical errors have to be checked. Figure 5.35 shows a typical measurement of

$I_{HC}$  over the time of a *scan*. The stability of the Heinzinger power supply is  $\leq 0.02\%$  of the nominal current over eight hours ( $I_{\text{nom}} = 1000 \text{ mA}$ , stability =  $0.2 \text{ mA}/8 \text{ hours}$ ). Therefore, as figure 5.35 shows, the current stability of the power supply is according to the specifications

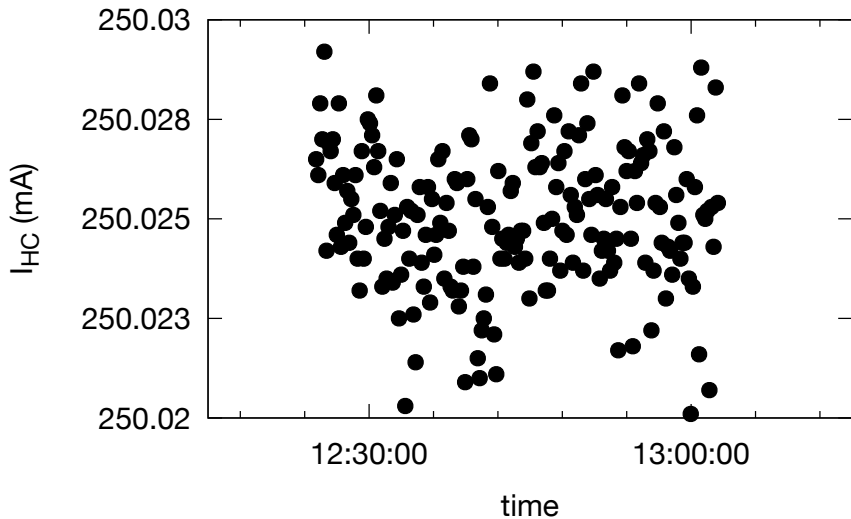


**Figure 5.35:** Typical stability of  $I_{HC}$  over the time of a *scan* measurement.

However,  $I_{HC}$  was recorded with the Keithley 7 $1/2$  digits resolution multimeter. The error of the current measurement is part of the extrapolation fits. Since for every *cycle* an error for the current (X-error) is taken into account, and since the power supply behaves according specifications, no systematical error has to be added.

## 5.4.2 Transition fitting function parameters

**Oscillating magnetic field:** The first fitting parameter that was checked is  $B_{\text{osc}}$ . This fitting parameter is extracted at the very beginning of the analysis where the conversion factor from  $\sqrt{P} \rightarrow B_{\text{osc}}$  is obtained. In principle  $B_{\text{osc}}$  has been already discussed and shown as free parameter in figure 5.11, but for completeness it should be displayed at this point once more for the fixed values.

The value that stands out from the others is for *set* number 3. Here the current in the superconducting sextupole magnet was *set* to 400 A instead of 350 for the others. The higher current in the sextupole has the effect that faster particles are focused onto the QMS which can also be seen in figure 5.37. Therefore, a higher amplitude of the oscillating magnetic field is needed to drive a spin flip. This effect can be inspected more

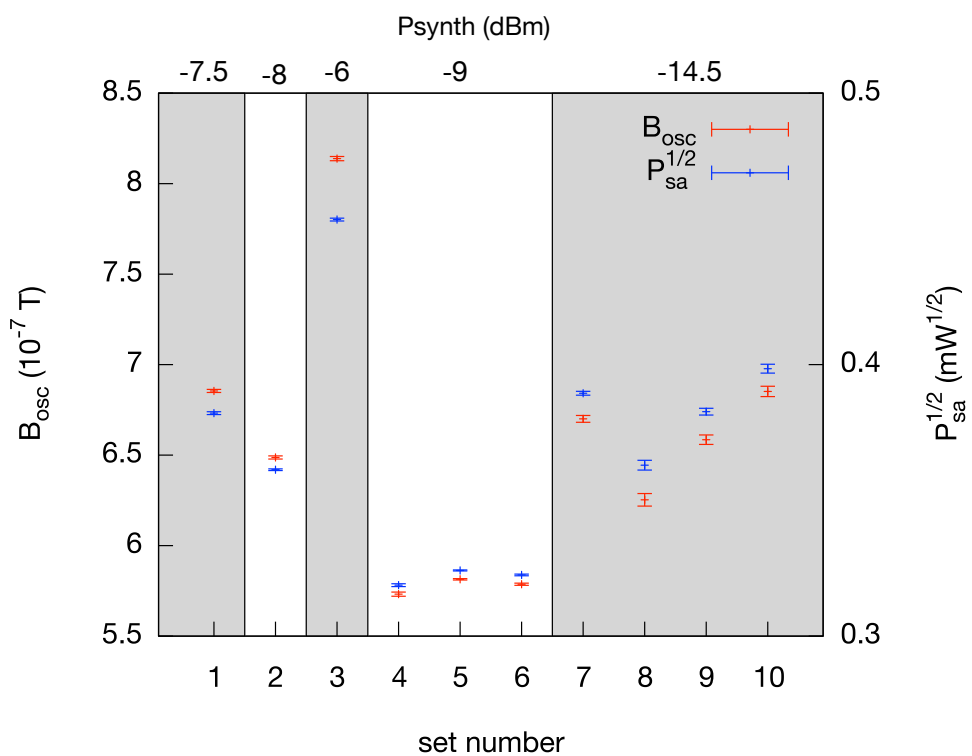


**Figure 5.36:**  $B_{\text{osc}}$ ,  $\sqrt{P_{\text{sa}}}$  and power at the synthesiser vs. set number.

quantitatively with figure 5.37 where *set 3* shows the higher velocity. For this graph the

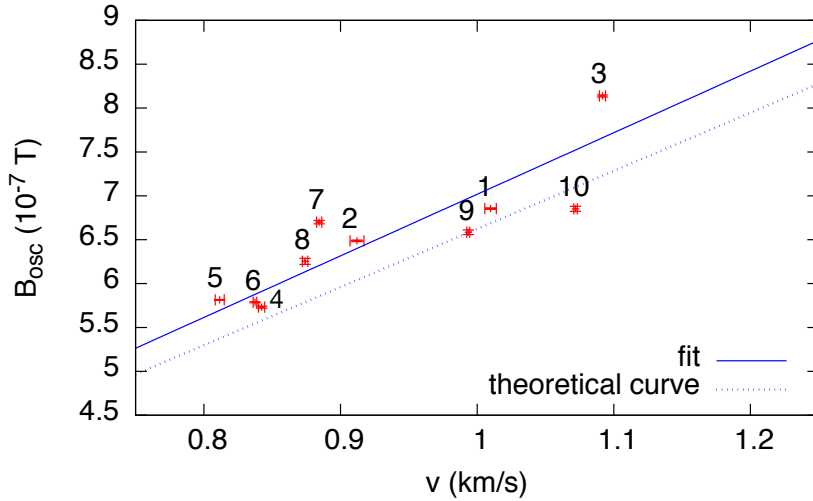


**Figure 5.37:** For a perfect  $\pi$ -pulse a linear relation between  $B_{\text{osc}}$  and velocity is present. However, the points deviate from the curve since not always the perfect  $\pi$ -pulse could be expected. The blue line shows a linear fit ( $y(x) = kx$ ) and the dashed line shows the theoretical line, taken from the theoretical map in figure 4.1. The numbers printed above the points correspond to the *set* number.

oscillating magnetic field was plotted vs. velocity. The velocity was extracted as discussed in section 5.3.5. The linear fit ( $y(x) = kx \rightarrow$  blue line) shows the average translation between oscillating magnetic field and the velocity of all points. The blue dotted line is the theoretical curve but without velocity smearing due to the velocity distribution. This graph shows qualitatively how far away from the perfect  $\pi$ -pulse the power was adjusted. The explanation for the linear relation between the oscillating magnetic field and the velocity is that for driving a  $\pi$ -pulse the product of interaction time and oscillating magnetic field amplitude has to be constant:

$$B_{\text{osc}} \cdot \tau_{\text{int}} = \frac{B_{\text{osc}}}{v} \cdot l_{\text{cav}} = \text{const.} \quad (5.7)$$

In figure 5.38 deviations for the hyperfine extrapolation values from the literature value vs. the oscillating magnetic field are shown.

**Velocity:** In figure 5.39 the extracted value  $\nu_0$  is displayed against the velocity. For none of the velocities a statistical relevant deviation can be derived.

Another interesting investigation is the comparison of velocities and the average reduced  $\chi^2$  of the transition measurements. In figure 5.40 it seems as if higher velocities yield a

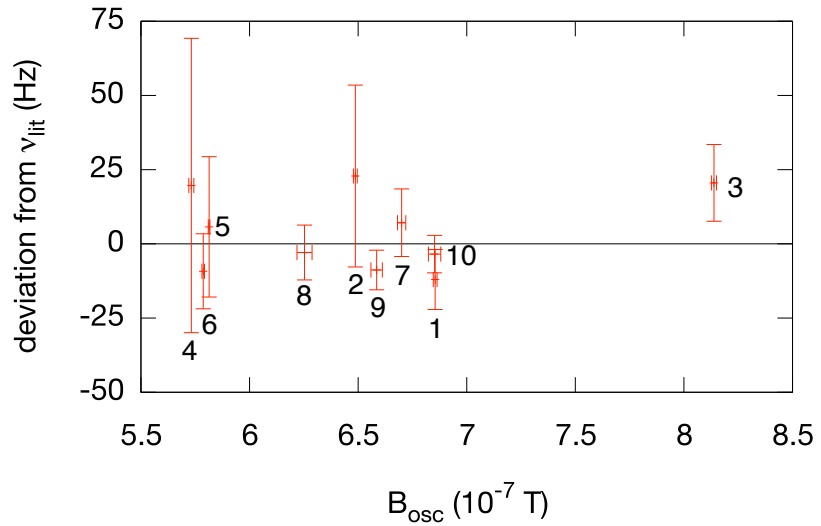


**Figure 5.38:** Frequency deviation from  $\nu_{\text{lit}}$  vs.  $B_{\text{osc}}$ . The numbers next to the points correspond to the *set* numbers. The black line at 0 Hz corresponds to  $\nu_{\text{lit}}$

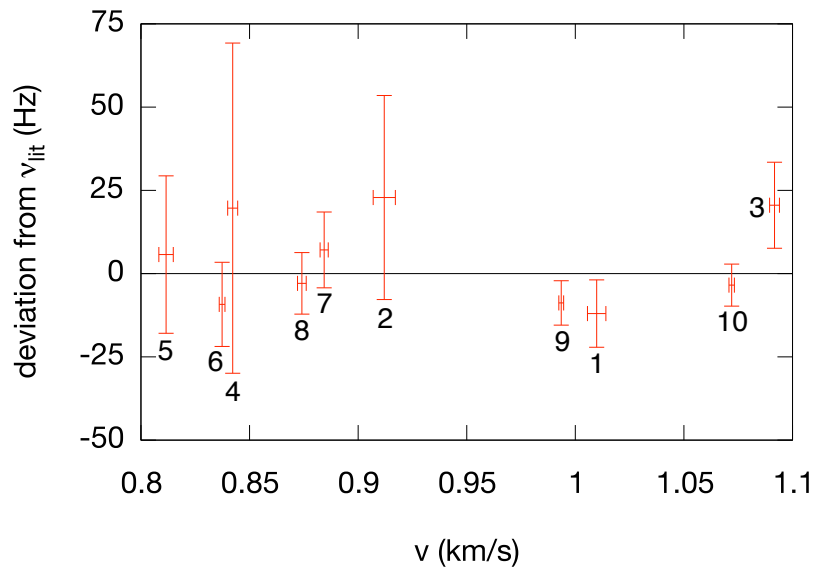


**Figure 5.39:** Frequency deviation from  $\nu_{\text{lit}}$  vs. velocity. The numbers around the points correspond to the *set* numbers.

higher  $\chi^2/n.d.f.$ , but it has to be mentioned that the *sets* with the higher  $\chi^2/n.d.f.$  are the *sets* 1-3 where the DAQ was not yet optimised and also the *sets* 9 and 10 where the oscillating magnetic had problems in the initial fits. Also since the errors are less than two standard deviations away from the other *sets* no systematics conclusions should be drawn.

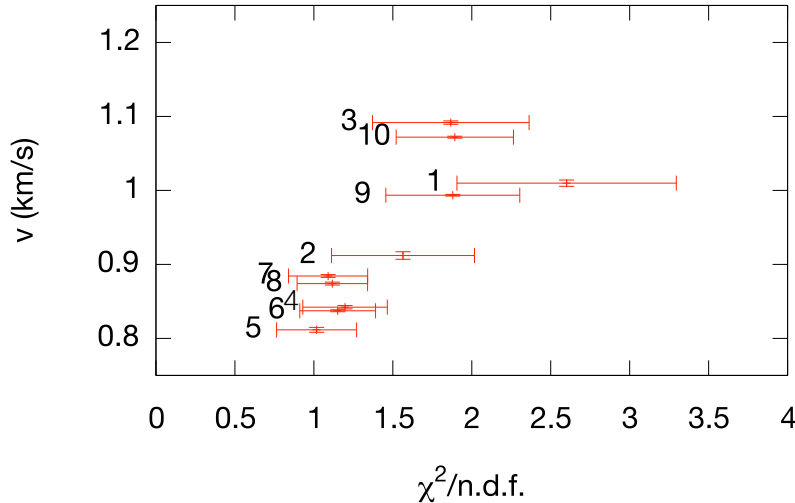


**Figure 5.40:** Velocity vs. reduced  $\chi^2$ . The trend for higher velocities could be an artefact since these *sets* are the data *sets* where the DAQ was not yet optimised (*sets* 1-3) or the  $B_{\text{osc}}$  had non physical values, respectively (*sets* 9 and 10).

**Velocity width:** When comparing the velocity width  $\sigma_v$  with  $\nu_0$  also no deviation from any of the *sets* can be seen (graph 5.41).

**Baseline of the resonance curves:** Next the baseline as obtained by equation 4.4 should be investigated. Plot 5.42 illustrates the baseline of the resonance curves as a function of the *set* number. For the *sets* 9 and 10 where the bigger aperture (last stage differential pumping) was installed the baseline is higher. This behaviour is obvious since more beam can pass the cavity and at the superconducting sextupole magnet the bigger beam is focused again onto the mass spectrometer. A plausible reason why in *set* number 9 the baseline is much higher than for *set* number 10 is not known. The change between the two settings is the distance between the two sextupole magnets ( $d_{\text{ss}}$ ). Different  $d_{\text{ss}}$  result in different velocities and since the superconducting sextupole magnet was always at 350 A, it could maybe explained that for *set* 10 due to the higher  $d_{\text{ss}}$  the beam could not be fully

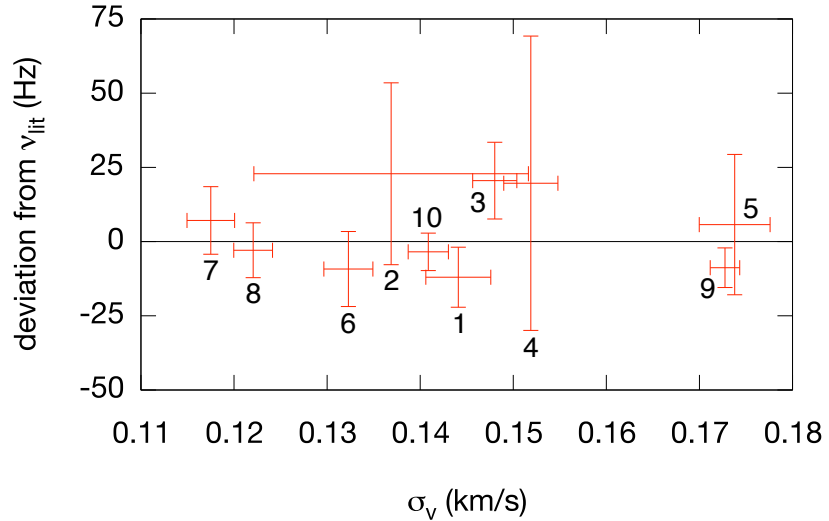


**Figure 5.41:** Frequency deviation from  $\nu_{lit}$  vs.  $\sigma_v$ . The numbers around the points correspond to the *set* numbers.

focused. Measurements as in figure 3.10 for *set* 9 and 10 probably could explain this, but unfortunately such measurements are not available.

**Amplitude:** Another interesting fitting parameter for *set* number 9 and 10 is the amplitude of the resonance curve obtained by equation 4.4. As for these two *sets* the beam was bigger it is clear that more particles would arrive at the detector. This consequence can be seen in figures 5.44 and 5.45.

#### Extrapolation fitting parameters:

So far the fitting parameters of function 4.4 were investigated and compared with the extrapolation values for the zero field hyperfine transition frequency. As already explained the extrapolation function 5.4 is depending also on two other parameters -  $C$  and  $B_0$

**Residual magnetic field inside the cavity:** One of the fitting parameters is a potential residual magnetic field inside the cavity. This magnetic field can be different for both cavities and thus, constant fits for the *sets* representative for both cavities were performed as shown in the plot 5.46. Obviously the residual magnetic field deviates slightly. This effect is not surprising since there are two different cavities which were exchanged

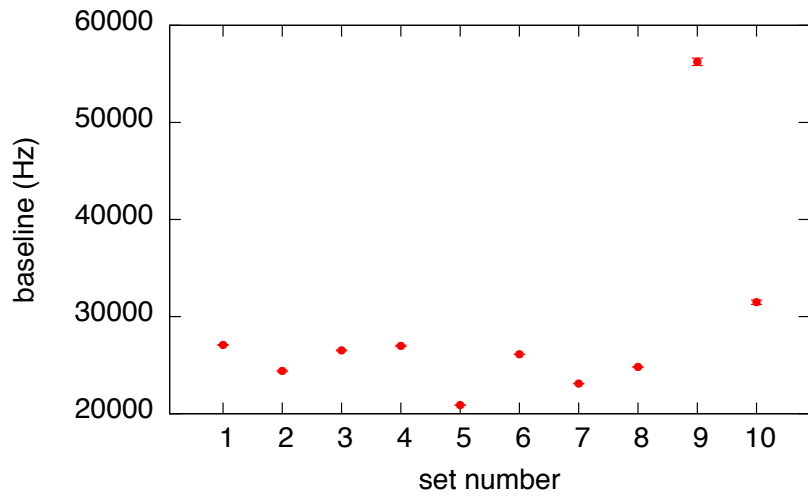


**Figure 5.42:** Baseline vs. *set* number. The jump at *set* 9 is due to the bigger aperture. *Set* number 10 is not as high which is probably due to rather (under)focusing effect by the superconducting sextupole magnet.

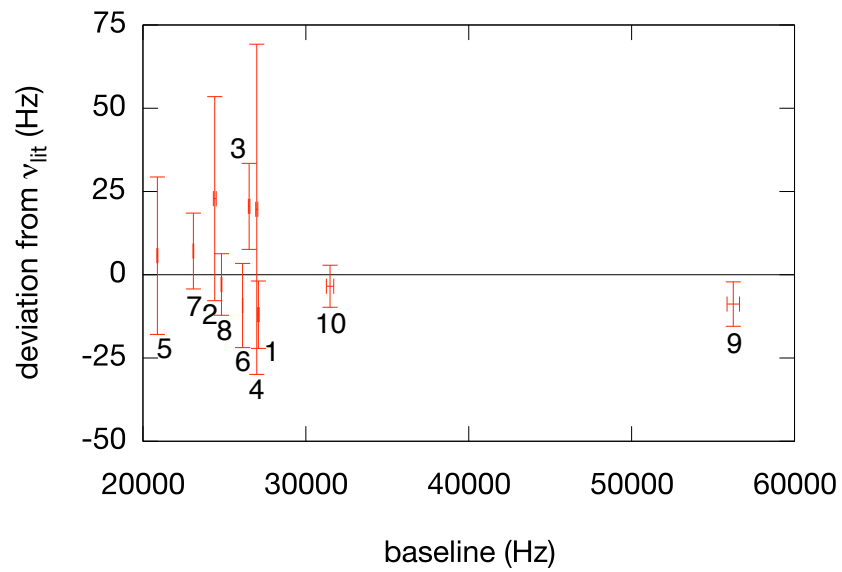


**Figure 5.43:** Frequency deviation from  $\nu_{\text{lit}}$  vs. baseline. The numbers around the points correspond to the *set* numbers.

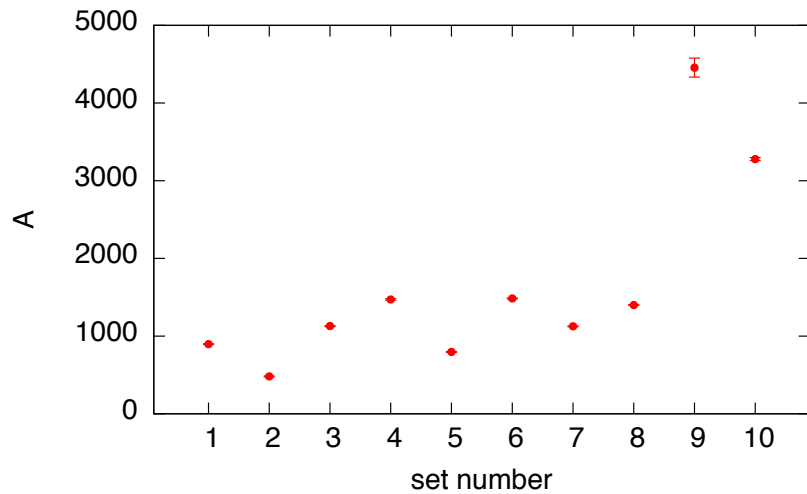


**Figure 5.44:** Amplitude of the fitting curve vs. the *set* number. For *set* number 9 and 10 the bigger aperture was used to test a bigger beam in the cavity.

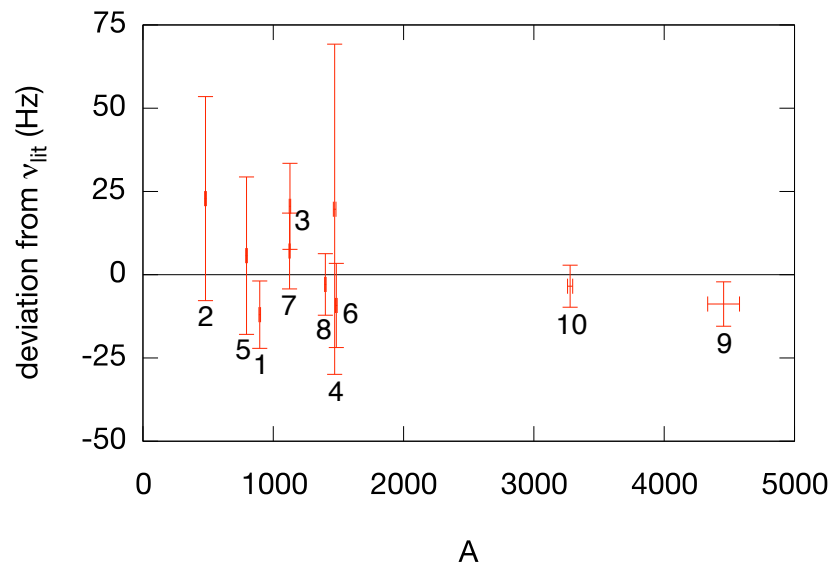


**Figure 5.45:** Frequency deviation from  $\nu_{\text{lit}}$  vs. amplitude of the fitting function. The numbers around the points correspond to the *set* numbers.

once and the Helmholtz coils had to be remounted after the cavity switch. All the fitting values are significantly different from zero. The only *set* which is not significant enough is *set 4*. Since there the polarity in Helmholtz coils was positive only, the fitting parameter has a very big error.

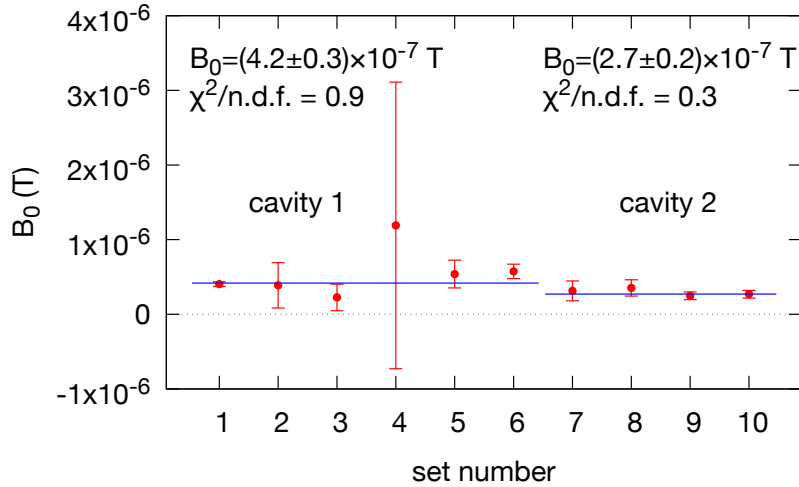


**Figure 5.46:** Residual magnetic field  $B_0$  in the microwave field vs. the *set* number for cavity 1 and cavity 2. The blue fitting lines correspond to the weighted mean values of the points.  $B_0$  is apparently slightly different for both cavities.

**Helmholtz current to static magnetic field conversion factor:** The same procedure as discussed above was applied to the factor that converts between  $I_{\text{HC}}$  and the static magnetic field. The result can be seen in figure 5.48. The factor under the two conditions also deviate slightly which can be explained once more with the realignment of the Helmholtz coils. Interestingly removing one layer of the shielding (*set 7*) had no effect on  $C$  and  $B_0$ .

As comparison the data shown in figure 3.7 has a value for the  $C$  factor of ( $C = 50 \pm 5$ )  $\times 10^{-5} \text{ T A}^{-1}$  for the fluxgate sensor one and ( $C = 49.4 \pm 3$ )  $\times 10^{-5} \text{ T A}^{-1}$  for the fluxgate sensor two. Given the fact that the fluxgate sensors have offsets in some of the components the values are agreeing quite well.

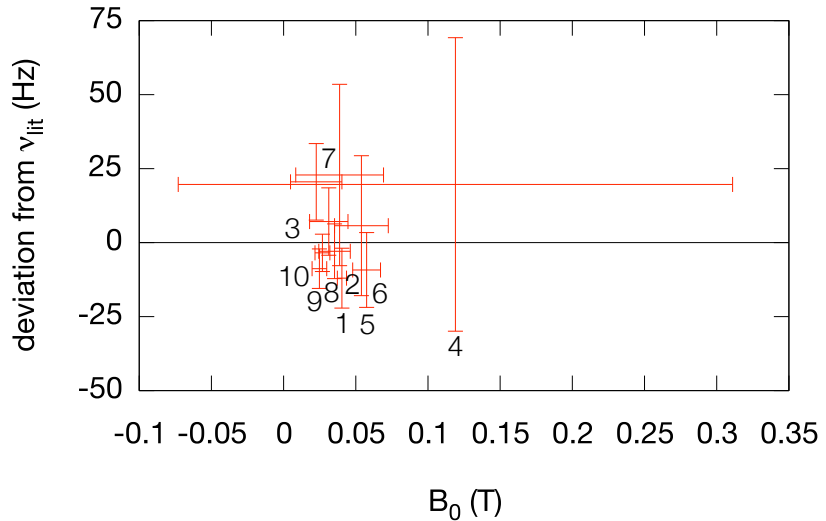


**Figure 5.47:** Frequency deviation from  $\nu_{\text{lit}}$  vs.  $B_0$  of the fitting function. The numbers around the points correspond to the *set* numbers.

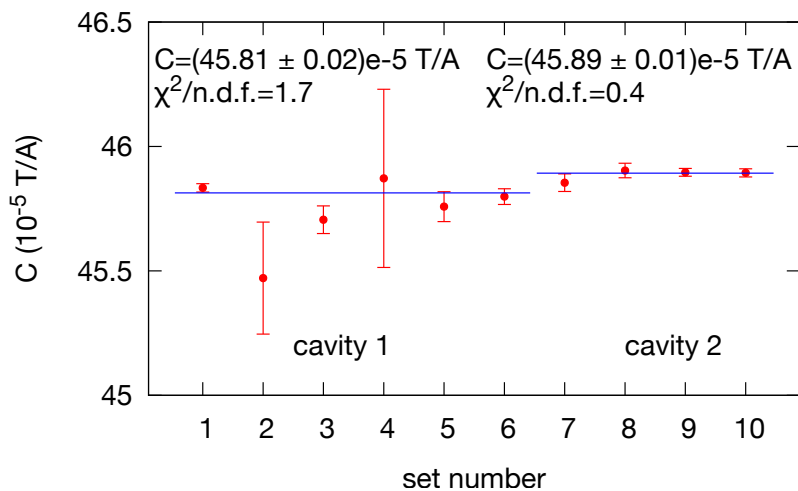


**Figure 5.48:** Conversion factor from  $I_{\text{HC}}$  to the static magnetic field inside the shielding vs. the *set* number for cavity 1 and cavity 2. The blue fitting lines correspond to the weighted mean values for each cavity.

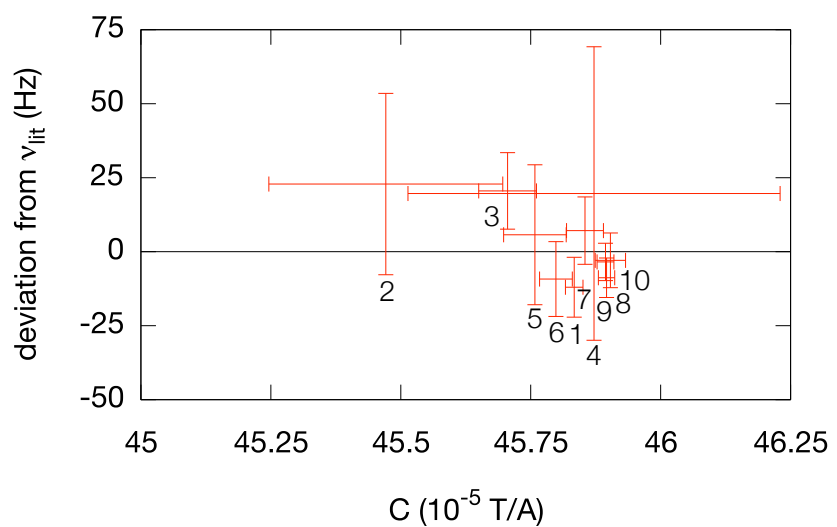


**Figure 5.49:** Frequency deviation from  $\nu_{\text{lit}}$  vs.  $C$  of the fitting function. The numbers around the points correspond to the *set* numbers.

### 5.4.3 Grouping of parameters

Next the parameters are grouped according the representation of the different settings of the setup to see whether a systematical discrepancy is present. For the measurements the weighted mean values were calculated for the individual groups.

**Hydrogen source alignment:** The *sets* 1-3 were performed with the atomic hydrogen source pointing straight in beam direction. In contrast *sets* 4-10 were performed with the hydrogen source perpendicular. As 5.50 shows the error bars overlap and thus, no deviation between the two groups can be observed.

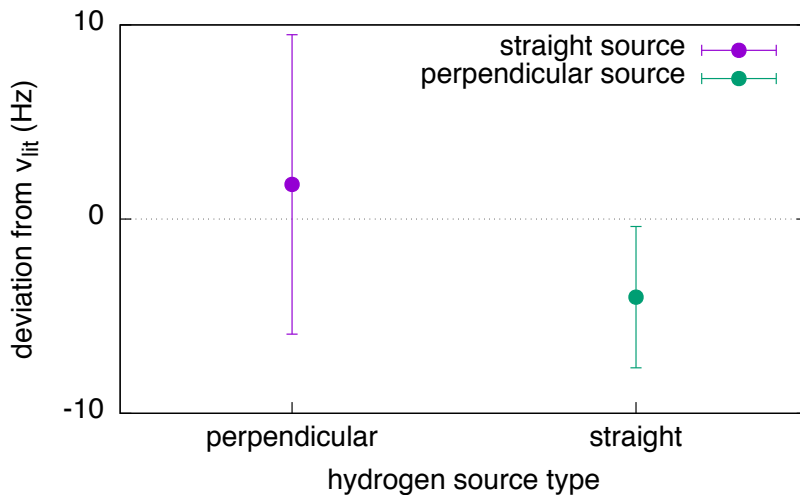


**Figure 5.50:** Comparison of the deviation from  $\nu_{\text{lit}}$  vs. the hydrogen source alignment.

**Cavities:** *Sets* 1-6 were performed with cavity 1 and cavity 2 was used in the *sets* 7-10. Grouping the *sets* accordingly yields no difference within the error bars (see figure 5.51).

**Distance between the permanent sextupole magnets:** The distance between the two permanent sextupole magnets was grouped into two types  $d_{ss} > 90$  mm consisting of the *sets* 1, 3, 10 and  $d_{ss} < 40$  mm consisting of the *sets* 2, 4, 5, 6, 7, 8, 9. In table 5.4 the distances are listed.

In the plot comparing the distances (fig. 5.52) no effect on the value for the hyperfine splitting can be seen.

As  $d_{ss}$  selects a velocity component, this way of grouping is related to plotting the results as a function of the fitted velocity (fig 5.39), where also no trend could be identified.

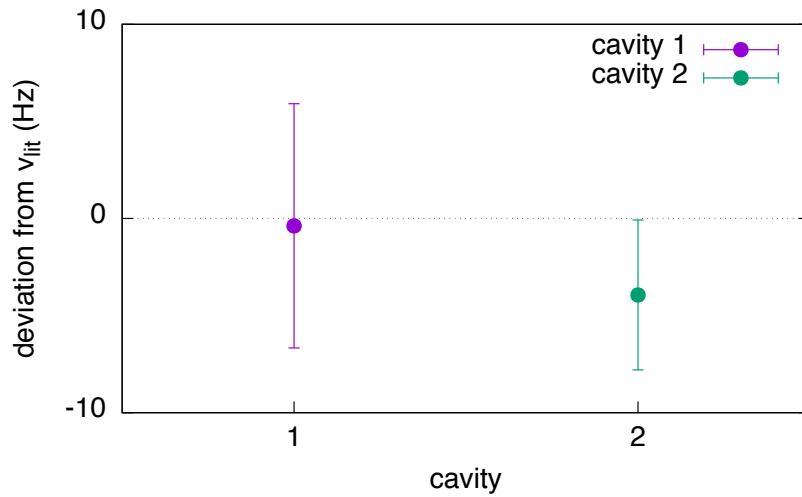


**Figure 5.51:** Comparison of the deviation from  $\nu_{\text{lit}}$  for the two cavities

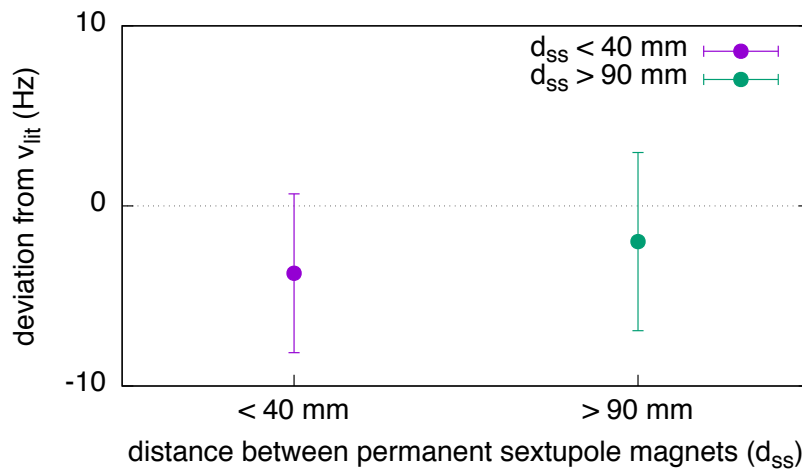


**Figure 5.52:** Comparison of the deviation from  $\nu_{\text{lit}}$  vs. grouped distances between the two permanent sextupole magnets.

set	1	2	3	4	5	6	7	8	9	10
$d_{ss}$ (mm)	115	35	91	25	25	16	16	16	16	115

**Table 5.4:** Distance between the two permanent sextupole magnets for all *sets*.

**Amount of  $\mu$ -metal shielding layers:** Most *sets* were recorded with 2 layers of  $\mu$ -metal shielding. The purpose of the shielding is to keep external magnetic fields away of the cavity and therefore, if the shielding does not perform well an impact on the hyperfine transition value could occur. Only one *set* (number 7) was performed with one layer to test the quality of the shielding. As graph 5.53 shows no effect is visible. This is probably due to the effect that in the experiment no external fields except the earth's magnetic field were present.

Additionally comparing to the discussions of  $B_0$  and  $C$ , where also *set* 7 didn't show significantly different values, insufficient shielding can be basically excluded as a source of error at the presented precision level.

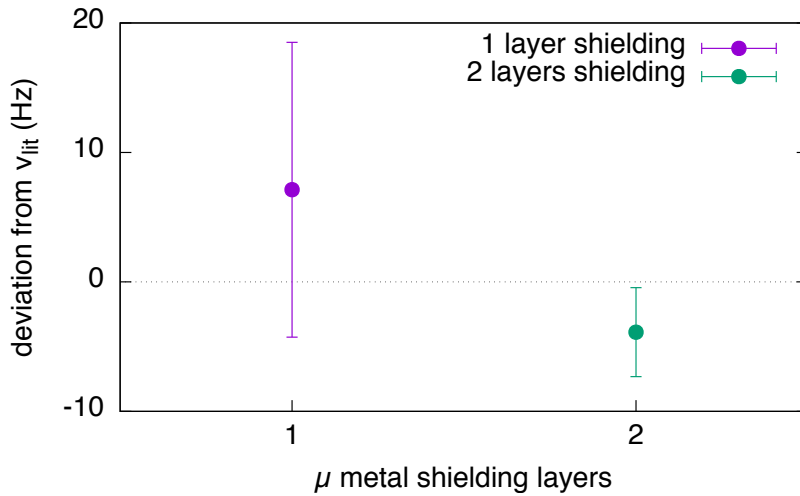


**Figure 5.53:** Comparison of the deviation from  $\nu_{lit}$  vs. the amount of  $\mu$ -metal shielding layers.

**Beam size:** One further test is by investigating the different beam sizes which were induced by the different aperture sizes. *Sets* 1-8 had a smaller aperture 2 and *sets* 9 and 10 a bigger aperture. Again by combining these *sets* no systematical effects regarding  $\nu_0$  can be constructed (see figure 5.54).

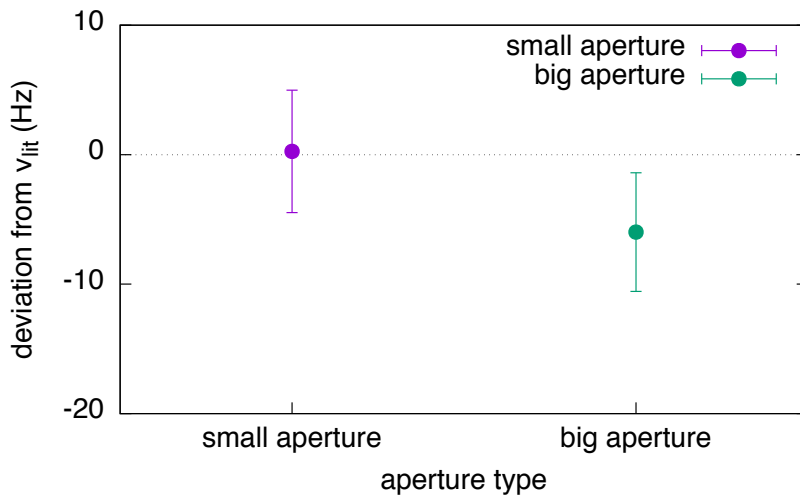


**Figure 5.54:** Comparison of the deviation from  $\nu_{\text{lit}}$  vs. the aperture type.

**Current in the superconducting sextupole magnet:** A final comparison with groupings of the extrapolation with 350 A and the 400 A (*set 3*) in the superconducting sextupole magnet showed a slight difference between the values and their extrapolated zero field hyperfine splitting. The result is displayed in figure 5.55.

By performing a student's  $\mathcal{T}$  test the probability of such an event can be estimated. The quantile of a Student  $\mathcal{T}$ -distribution for a 5 percent confidence interval with 8 degrees of freedom is  $t(0.975, 8) = 2.069$ . For this configuration the quantile is 1.938. Since the quantile  $1.938 < 2.069$  within a 95% confidence interval the two values are compatible. Or in other words the probability of such an event to happen  $P(1.938, 8) \cong 8.9\%$ . Additionally given the fact that the 400 A grouping was achieved with one *set* only there is no reason to interpret this result as a significant trend.

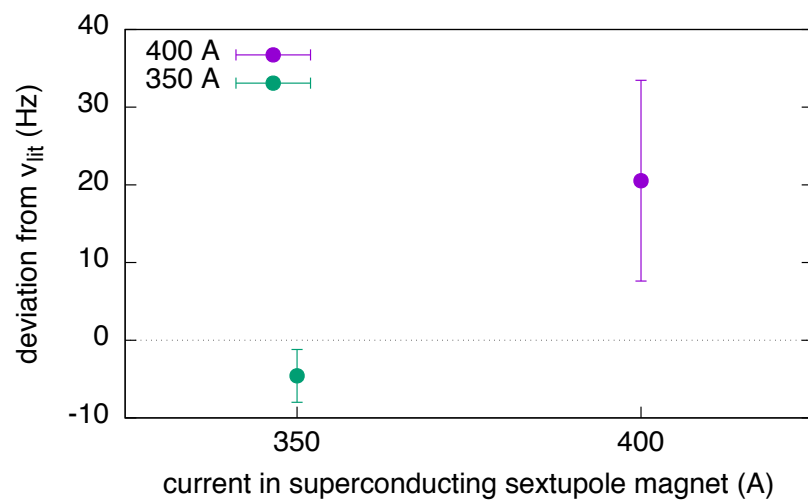


**Figure 5.55:** Comparison of the deviation from  $\nu_{\text{lit}}$  vs. current in the superconducting sextupole magnet. With a T test it can be shown that such an event to happen has a probability of about 9 percent.

## 5.5 Combined zero field hyperfine splitting (step 10)

A conclusion from the last section is that no noticeable systematical effects speak against combining all ten *sets* into a weighted mean value. Figure 5.56 shows the combined weighted mean from a fit of a constant ( $y = d$ ) to the values of the ten *sets*. The combined value for  $\nu_0 - \nu_{\text{lit}} = (-3.0 \pm 3.3) \text{ Hz}$ , which corresponds to a relative precision of  $2.3 \times 10^{-9}$ . The  $\chi^2/n.d.f. = 7.0/9$  and is less than 1. Thus, no significant indication for a systematical discrepancy can be seen.

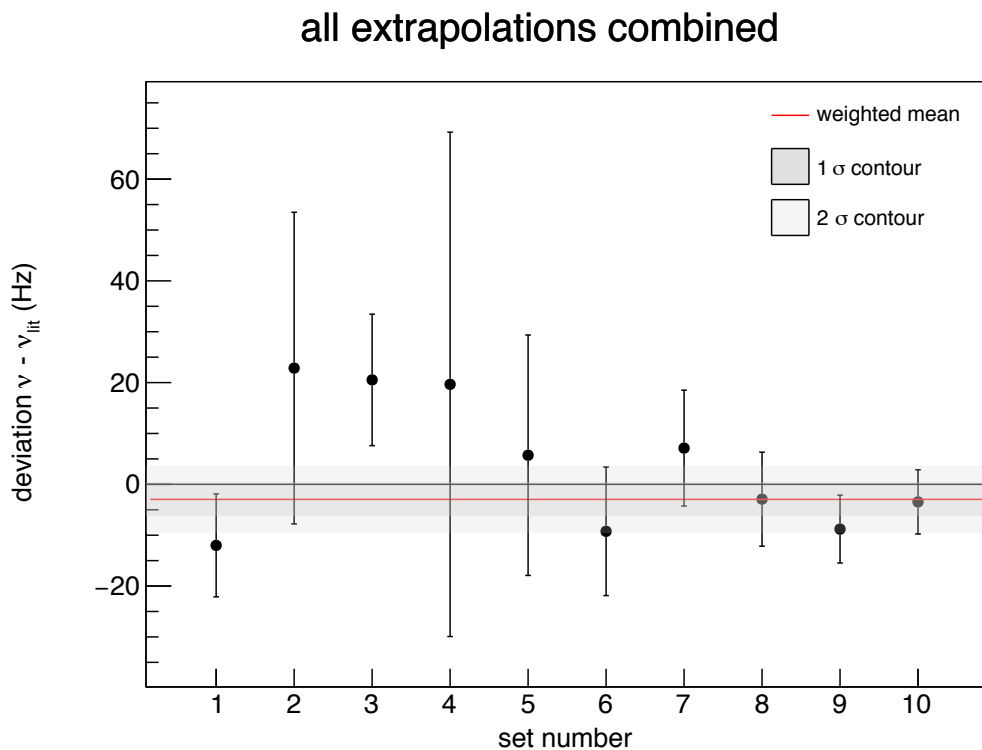


**Figure 5.56:** frequency deviation of the experimental fitting results vs. the *set* number. The red line shows the final value for the weighted mean hyperfine structure constant of the experiment. The two grey rectangles show the  $1\sigma$  and  $2\sigma$  (standard deviation) contour. The zero value is still inside the  $1\sigma$  contour.

However the error for this result is purely statistical and even if there are no indication for systematic effects, a potential systematic error has to be investigated and quantified. The systematical error was estimated by repeating the analysis, while changing the values of the fixed fitting parameters  $B_{\text{osc}}$ ,  $v$  and  $\sigma_v$ . For each of these variables the originally obtained value was changed by plus or minus one standard deviation multiplied by the Birge factor

**Table 5.5:** Table of the systematical shifts by changing the values for the fixed parameters. The sign in the setting column describes whether the variable was increased or decreased by a standard deviation. The second column shows the  $\chi^2/n.d.f.$  for the weighted mean of the 10 sets. The third column shows the deviation from the above presented hyperfine measurement and the fourth column shows the error for the third column. Below the systematical error for the synthesiser frequency caused by a drift of the Rb clock used for stabilisation is given.

setting	$\chi^2/n.d.f.$	$\nu_0 - \nu_{0\ sys}$ (Hz)	error (Hz)
$B_{\text{osc-}}$	5.4/9	0.5	0.12
$B_{\text{osc+}}$	8.9/9	1.4	0.03
$v_-$	6.2/9	0.1	0.03
$v_+$	8.6/9	0.7	0.04
$\sigma_{v-}$	8.3/9	1.0	0.02
$\sigma_{v+}$	9.5/9	1.1	0.02
other systematical errors			
synthesiser		1.6 Hz	

$R_B$  of the average of the velocity,  $\sigma_v$ , or  $B_{\text{osc}}$  per set, e.g.  $B_{\text{osc } i} \rightarrow B_{\text{osc } i} \pm \sigma_{B_{\text{osc } i}} R_B$  where  $R_B = (\chi^2/n.d.f.)^{1/2}$  is the Birge factor with  $n.d.f.$  the degrees of freedom [88]. By repeating this sequence for every setting a systematical shift of the frequency  $\nu_0$  was obtained. The larger value for the shift for each fitting parameter (plus or minus, respectively) was defined to be the systematical error for every parameter. The results are presented in table 5.5.

Additionally to the systematical errors due to the fitting procedure an error from the clock (Rb standard) should be considered. According to the manufacturer the maximum drift per year is 5 mHz. A calibration was done after three years by the manufacturer and the shift of the clock was 11.4 mHz. This shift has to be taken into account as a maximal systematic error in the synthesiser frequency. The 11.4 mHz error of the Rb standard is 1.14 ppb relative error to the 10 MHz signal used to stabilise our synthesiser. This relative error causes an error of 1.14 ppb of the driving signal of the synthesiser. Therefore, the systematical error of the synthesiser is 1.6 Hz.

Combining all systematical errors in quadrature the final result for the ground state zero field hyperfine splitting is:

$$\nu_0 = 1\,420\,405\,748.9 \pm 3.3^{\text{stat}} \pm 2.5^{\text{sys}} \text{ Hz} \quad (5.8)$$

This value is in agreement with the literature and deviates by  $-3.0$  Hz from the maser value which is within the error. The best measurement for the hyperfine splitting in a beam

with a Rabi like configuration was performed by Kusch et al. in 1955 which had a relative precision of 35.2 ppb. The value reported in this work has a relative error of 2.9 ppb which is a factor of 12 better in precision and therefore, is the best in-beam measurement for the hyperfine splitting of atomic hydrogen so far.



# 6 Summary & outlook

## 6.1 Summary

In this work a precise measurement of the ground-state hydrogen hyperfine structure in a Rabi-type beam setup has been presented. The results are of special relevance to the antihydrogen hyperfine structure project of the ASACUSA collaboration at the Antiproton Decelerator at CERN. Two key components of the antihydrogen hyperfine spectrometer beam line, namely the spin-flip driving microwave cavity and the spin-state analysing superconducting sextupole magnet, have been used. The final value obtained for the hydrogen hyperfine splitting is  $\nu_0 = 1\,420\,405\,748.9 \pm 3.3^{\text{stat}} \pm 2.5^{\text{sys}} \text{ Hz}$  and is in agreement with the results from maser experiments. The result corresponds to 2.9 ppb relative error and is the best result obtained in a beam so far. The measurement is 12 times better than Kusch et al. who achieved the best beam result before.

Besides these measurements resulting from extrapolations of the  $\sigma_1$  transitions, resonance spectra in the earth's magnetic field could be recorded. These results showed that the setup is capable of driving  $\pi_1$  transitions.

The hydrogen source and detector have been assembled and tested at SMI in Vienna before being transported to CERN. There, the spin-flip driving microwave cavity and the spin-state analysing superconducting sextupole of ASACUSA's antihydrogen experiment were added to form a complete Rabi-type setup. After characterisation of the components and a series of measurements, which lead to the aforementioned hyperfine splitting determination, the microwave cavity and sextupole magnet had to return to the antihydrogen setup for the experimental antiproton runs in 2014 and 2015.

The first part of the data analysis was the focused on the most appropriate fitting function. Analysis procedures for the resonance curves of the hyperfine spectra were investigated. One part was correction of the raw data due to systematical effects such as detector drifts and count rate memory shifts. Some fitting parameters were individual for each resonance curve but others could be fixed by measured quantities or commonly to values for complete sets respectively.

Important outcomes for the antihydrogen experiment are that the power dependence of the spin flip cavity could be obtained. The information necessary for the correct oscillating magnetic field in the antihydrogen experiment will be the velocity. If it is known, one can immediately start with transition measurements. Currently, the velocity of antihydrogen atoms in the experiment is not well known. Thus, the instrument was tested at many different experimental conditions such as the size of the hydrogen beam or the superconducting sextupole magnet properties. Additionally a calibration for the Helmholtz coils was gained which will help to set the correct frequency during antihydrogen hyperfine transition measurement.

Since the spectrometer worked with a hydrogen beam according the technical design parameters of the antihydrogen beam, it can be used in the antihydrogen experiment for measurements of hyperfine transitions.

## 6.2 Outlook

The next steps in the hydrogen beam investigations will be repeating the experiment in similar detail with the  $\pi_1$  transition. Some changes will be applied to the setup since parts of the beam line are needed in the antihydrogen experiment. Nevertheless, of the two cavities one will be available. Therefore, only an analysing magnet instead of the superconducting sextupole magnet will be needed. The main things left to investigate will be extending the beam to the full antihydrogen beam size and test the effects on the line shape of the fitting function.

Additionally by measuring with the  $\pi_1$  transitions with atomic hydrogen, first parameter bounds for some of the parameters of the minimal standard model extension could be measured (without the need of antihydrogen) [89]. Therefore, work is ongoing in designing new, more homogeneous Helmholtz coils and an appropriate  $\mu$ -metal shielding.

Improving the value of  $\nu_0$  will not be easy. Some improvements would be a cooler beam which would obviously yield a slower beam. A slower beam would reduce the line width of the resonance curves and therefore, improve the potential precision. A second option would be adding the second cavity into the beam line and perform the experiment in a Ramsey-type beam setup. This step would once more reduce the line width of the resonance curves. The third idea, if systematical errors would not yet be present, is to collect statistics by repeating the experiment many times and improve an average value. However, the maser value is  $10^{-12}$  relative precision, which seems hard to compete, but

SME parameters, which are not accessible to a maser, can be measured with the hydrogen beam line. Therefore, one focus will be the measurement of SME parameters.



# **Appendices**

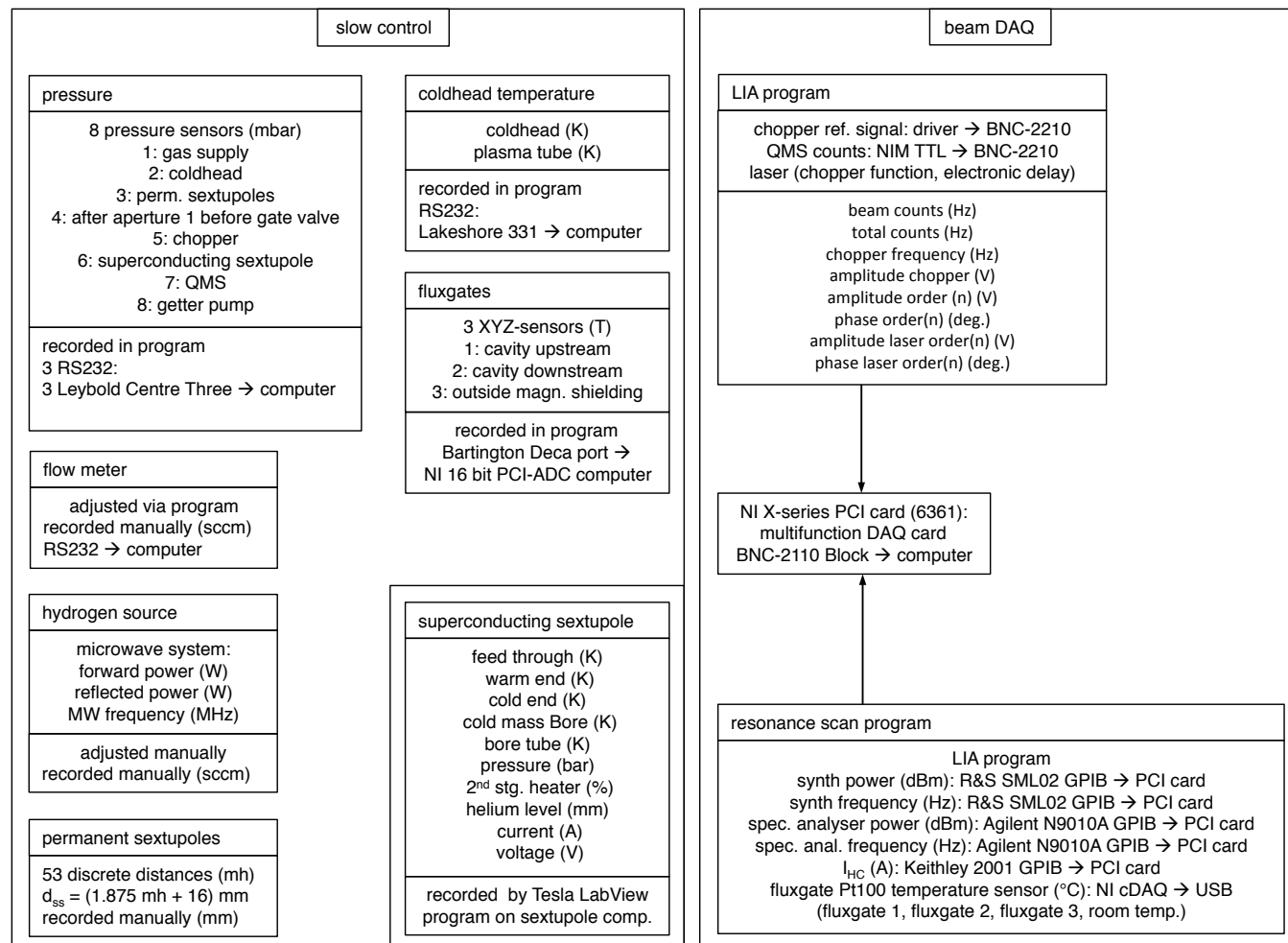


**Figure A.1** Full DAQ scheme of hydrogen beam parameters

**Table A.1** DAQ settings for  $\sigma_1$  data sets:  $I_{HC}$  - current in Helmholtz coils,  $n_{cycles}$  - number of cycles;  $n_f$  - number of frequency points per cycle; set 1: 60 seconds averaging; set 2-3: 40 seconds averaging; set 4-10: 5 seconds averaging;

set 1			set 2			set 3			set 4			set 5		
$I_{HC}$ (mA)	$n_{cycles}$	$n_f$												
-100	3	41	-100	5	21	-100	3	26	50	5	39	-50	5	39
-205	3	41	-200	5	21	-200	6	26	100	5	39	-150	5	39
-410	3	41	-300	5	21	-300	6	26	150	5	39	-250	5	39
-615	3	41	100	6	21	100	3	26	200	5	39	-350	5	39
100	3	41	200	20	21	200	5	26	250	5	39	-450	5	39
205	3	41	300	5	21	300	3	26	300	5	39	-550	5	39
410	3	41							350	5	39	50	5	39
615	3	41							400	5	39	150	5	39
									450	5	39	250	5	39
									500	5	39	350	5	39
												450	5	39
												550	5	39
set 6			set 7			set 8			set 9			set 10		
$I_{HC}$ (mA)	$n_{cycles}$	$n_f$												
-50	5	39	-20	5	39	-20	5	39	-50	5	39	-50	5	39
-150	5	39	-50	5	39	-50	5	39	-100	5	39	-100	5	39
-250	5	39	-80	5	39	-80	5	39	-250	5	39	-250	5	39
-350	5	39	-130	5	39	-130	5	39	-350	5	39	-350	5	39
-450	5	39	-180	5	39	-180	5	39	-400	5	39	-400	5	39
-550	5	39	-250	5	39	-250	5	39	-550	5	39	-550	5	39
50	5	39	-400	5	39	-400	5	39	50	5	39	50	5	39
150	5	39	-550	5	39	-550	5	39	100	5	39	100	5	39
250	5	39	20	5	39	20	5	39	250	5	39	250	5	39
350	5	39	50	5	39	50	5	39	350	5	39	350	5	39
450	5	39	80	5	39	80	5	39	400	5	39	400	5	39
550	5	39	130	5	39	130	5	39	550	5	39	550	5	39
			180	5	39	180	5	39						
			250	5	39	250	5	39						
			400	5	39	400	5	39						
			550	5	39	550	5	39						

**Table A.2** Justification to fix velocity and dv by constant fit. Since for a linear fit ( $y = kx + d$ ) the errors for  $k$  were greater than 100%, a constant fit (weighted mean) could be used to fix the value.

set	v fitted with kx+d (v vs. time)			v fitted with constant		dv fitted with kx+d (v vs. time)			dv fitted with constant	
	$\chi^2$	k error (%)	d error (%)	$\chi^2$	d error (%)	$\chi^2$	k error (%)	d error (%)	$\chi^2$	d error (%)
1	12.9	110.3	0.63	12.57	0.42	4	100.4	3.41	4	2.42
2	5.67	424.3	1.33	4.6	0.56	2.51	14.72	13.5	25.21	10.78
3	1.36	70.77	0.43	1.63	0.21	1.32	361.1	3.96	1.08	1.6
4	1.21	125.4	0.65	1.16	0.27	1.72	144.2	5.17	1.62	1.92
5	1.27	424.9	1.04	1.16	0.41	3.69	280.7	5.58	3.4	2.19
6	0.5	58.92	0.33	0.58	0.16	1.31	66.17	3.84	1.46	1.99
7	1.31	128.5	0.5	1.27	0.21	1.71	237.7	4.65	1.61	2.18
8	2.11	105	0.36	2.1	0.23	1.24	77.37	2.42	1.29	1.71
9	1.33	374.9	0.26	1.22	0.11	1.14	51.79	1.98	1.43	0.92
10	3.15	66.23	0.19	3.51	0.12	2.12	50.67	2.22	2.68	1.53

**Table A.3** Justification of the systematical effects analysis. Since the count rate memory shift, when fitted with a linear function ( $y = kx + d$ ) had errors greater than 100% for  $d$ ,  $k$  was combined to a weighted mean. Additionally the drift correction fit results are displayed.

set	count rate memory shift fitted with $kx+d$			count rate memory shift fitted with constant		drift correction	
	average $\chi^2$	k error (%)	d error (%)	average $\chi^2$	k error (%)	average $\chi^2$	k error (%)
1	$4.46 \pm 1.01$	24.39	3372.22	0.52	51.8	$2.79 \pm 1.07$	51.64
2	$2.41 \pm 0.97$	28.22	977.39	0.34	41.39	$1.55 \pm 0.45$	12.63
3	$2.48 \pm 0.46$	30.71	977.25	0.27	48.34	$1.92 \pm 0.53$	29.8
4	$1.27 \pm 0.09$	22.07	3277.18	0.5	24.2	$1.21 \pm 0.26$	78.17
5	$1.11 \pm 0.1$	8.55	1964.22	0.93	8.99	$1.11 \pm 0.26$	107.75
6	$1.19 \pm 0.08$	16	6006.81	0.3	17.35	$1.16 \pm 0.24$	47.99
7	$1.16 \pm 0.12$	10.21	650.69	0.68	10.92	$1.14 \pm 0.26$	25.75
8	$1.17 \pm 0.09$	13.57	1575.81	0.64	14.78	$1.14 \pm 0.22$	74.2
9	$2 \pm 0.27$	17.59	1011.75	0.64	24.2	$1.88 \pm 0.41$	19.01
10	$2.3 \pm 0.26$	19.9	640.39	0.64	29.38	$1.89 \pm 0.37$	4.28

**Table A.4**  $\sigma_1$  transition measurement - zero field extrapolation settings, data acquisition, and extrapolation results.

set	1	2	3	4	5	6	7	8	9	10
<b>source alignment</b>	straight	straight	straight	90 deg.						
<b>T<sub>c</sub> (K)</b>	23	16	100	50	50	50	50	50	50	50
<b>d<sub>ss</sub> (mm)</b>	115	35	91	21	21	16	16	16	16	115
<b>cavity</b>	1	1	1	1	1	1	2	2	2	2
<b>I<sub>HC</sub> measured with Keithley DMM</b>	no	no	no	yes						
<b>supercond. sextupole (A)</b>	350	350	400	350	350	350	350	350	350	350
<b>beam diameter (mm)</b>	8	8	8	8	8	8	8	8	22	22
<b>shielding layers</b>	2	2	2	2	2	2	1	2	2	2
<b>I<sub>HC</sub> polarity</b>	+-	+-	+-	+	+-	+-	+-	+-	+-	+-
<b>scans</b>	8	6	6	10	12	12	16	16	12	12
<b>cycles</b>	23	46	26	50	60	60	80	80	60	60
<b>frequency points</b>	41	21	26	39	39	39	39	39	39	39
<b>time of data taking for count rate acquisition (s)</b>	60	40	40	5	5	5	5	5	5	5
$\nu_{\text{HF}} - \nu_{\text{HF}}^{\text{fit}} (\text{Hz})$	$-12.0 \pm 10.1$	$22.9 \pm 30.6$	$20.5 \pm 12.9$	$19.7 \pm 49.6$	$5.7 \pm 23.6$	$-9.2 \pm 12.6$	$7.1 \pm 11.4$	$-2.9 \pm 9.2$	$-8.8 \pm 6.7$	$-3.5 \pm 6.3$
$\chi^2/\text{n.d.f. of extrapol.}$	17.4/21	38.7/44	41.2/24	70.0/47	65.3/57	48.5/57	101.0/77	83.2/77	75.0/57	55.6/57
<b>av. red. <math>\chi^2</math> of resonances</b>	$2.6 \pm 0.7$	$1.6 \pm 0.5$	$1.9 \pm 0.5$	$1.2 \pm 0.3$	$1.0 \pm 0.3$	$1.2 \pm 0.2$	$1.1 \pm 0.3$	$1.1 \pm 0.3$	$1.9 \pm 0.4$	$1.9 \pm 0.4$
<b>v (m/s)</b>	$1010 \pm 4$	$912 \pm 5$	$1092 \pm 2$	$842 \pm 2$	$812 \pm 3$	$837 \pm 1$	$884 \pm 2$	$874 \pm 2$	$994 \pm 1$	$1072 \pm 1$
$\sigma_v (\text{m/s})$	$144 \pm 3$	$137 \pm 15$	$148 \pm 2$	$152 \pm 3$	$174 \pm 4$	$132 \pm 3$	$118 \pm 3$	$122 \pm 2$	$173 \pm 2$	$141 \pm 2$
$\hat{B}_{\text{osc}} (10^{-7} \text{ T})$	$6.85 \pm 0.01$	$6.49 \pm 0.01$	$8.14 \pm 0.01$	$5.73 \pm 0.01$	$5.81 \pm 0.00$	$5.79 \pm 0.01$	$6.70 \pm 0.02$	$6.25 \pm 0.03$	$6.59 \pm 0.03$	$6.85 \pm 0.03$
<b>baseline (Hz)</b>	$27088 \pm 1$	$24409 \pm 1$	$26519 \pm 2$	$26989 \pm 3$	$20886 \pm 2$	$26117 \pm 2$	$23097 \pm 2$	$24820 \pm 2$	$56241 \pm 4$	$31486 \pm 3$
<b>amplitude (Hz)</b>	$896 \pm 2$	$480 \pm 3$	$1128 \pm 4$	$1471 \pm 6$	$795 \pm 6$	$1484 \pm 5$	$1125 \pm 5$	$1400 \pm 5$	$4456 \pm 8$	$3278 \pm 5$
$B_{\text{res}} (10^{-7} \text{ T})$	$4.0 \pm 0.3$	$3.9 \pm 3.0$	$2.3 \pm 1.8$	$11.9 \pm 19.2$	$5.4 \pm 1.9$	$5.7 \pm 1.0$	$-3.1 \pm 1.3$	$-3.5 \pm 1.1$	$-2.5 \pm 0.5$	$-2.7 \pm 0.5$
$C (10^{-5} \text{ T/mA})$	$45.83 \pm 0.02$	$45.47 \pm 0.22$	$45.71 \pm 0.06$	$45.87 \pm 0.36$	$45.76 \pm 0.06$	$45.80 \pm 0.03$	$45.85 \pm 0.04$	$45.90 \pm 0.03$	$45.90 \pm 0.02$	$45.89 \pm 0.02$

---

## Fit results for all the resonance cycles of all sets

set	$I_{HC}$ (mA)	error (mA)	$\nu_c$ (Hz)	error (Hz)	$\chi^2$	d.o.f.
1	-100	1	610.5	31.3	70.8	38
1	-100	1	546.1	32.9	83.8	38
1	-100	1	585.8	32.4	106.6	38
1	-205	1	2442.4	33.4	135.3	38
1	-205	1	2497.6	33.6	102.7	38
1	-205	1	2414.8	32.8	102.6	38
1	-410	1	9818.7	32.8	128.9	38
1	-410	1	9837.0	33.7	129.7	38
1	-410	1	9813.1	32.1	86.1	38
1	-615	1	22072.4	35.5	133.6	38
1	-615	1	22120.3	35.1	87.6	38
1	-615	1	22092.3	35.0	161.6	38
1	100	1	578.5	33.7	95.9	38
1	100	1	606.5	34.5	84.3	38
1	100	1	456.4	34.4	102.9	38
1	205	1	2440.4	33.4	75.3	38
1	205	1	2442.1	33.1	103.7	38
1	205	1	2432.5	32.8	82.0	38
1	410	1	9691.9	32.1	94.0	38
1	410	1	9786.3	34.6	56.8	38
1	615	1	21964.7	34.1	87.1	38
1	615	1	21892.8	33.1	111.7	38
1	615	1	21964.3	33.2	49.8	38

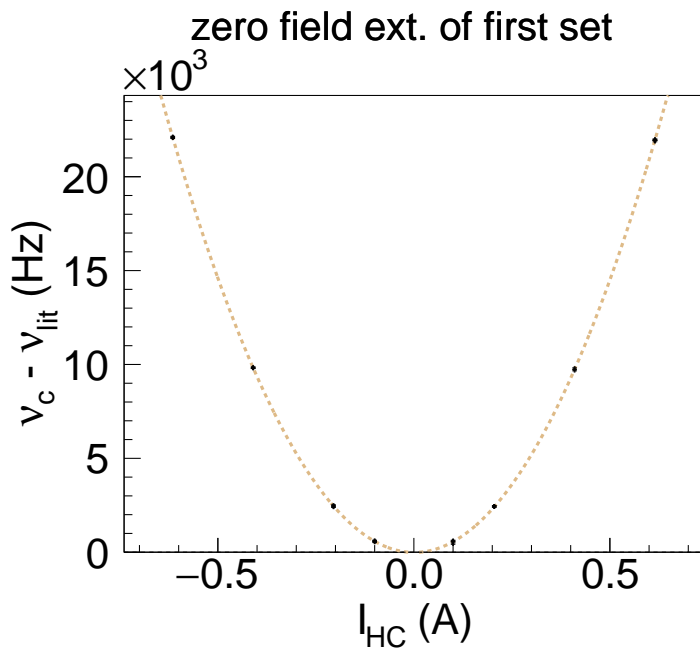


**Figure A.2** Zero field extrapolation; set number 1.

---

<b>set</b>	<b><math>I_{\text{HC}}</math> (mA)</b>	<b>error (mA)</b>	<b><math>\nu_c</math> (Hz)</b>	<b>error (Hz)</b>	<b><math>\chi^2</math></b>	<b><i>d.o.f.</i></b>
2	-100	1	477.3	109.6	15.0	18
2	-100	1	473.7	107.3	34.3	18
2	-100	1	503.6	100.9	26.7	18
2	-100	1	625.7	98.1	38.7	18
2	-100	1	619.0	114.9	38.7	18
2	-200	1	2288.2	97.6	20.3	18
2	-200	1	2495.2	122.5	23.5	18
2	-200	1	2304.2	98.9	18.2	18
2	-200	1	2280.4	100.6	11.9	18
2	-200	1	2374.5	95.1	20.9	18
2	-300	1	5281.1	105.3	37.0	18
2	-300	1	5218.8	98.9	26.7	18
2	-300	1	5205.6	101.2	37.9	18
2	-300	1	5368.4	98.8	25.8	18
2	-300	1	5110.3	98.3	35.4	18
2	100	1	655.4	135.4	24.0	18
2	100	1	453.1	118.2	36.5	18
2	100	1	828.3	117.9	16.8	18
2	100	1	589.4	111.4	30.2	18
2	100	1	584.1	115.7	32.4	18
2	100	1	490.9	127.6	31.6	18
2	200	1	2193.3	107.1	17.4	18
2	200	1	2243.4	105.6	21.9	18
2	200	1	2226.9	95.4	46.8	18
2	200	1	2299.9	104.1	22.6	18
2	200	1	2512.6	96.6	16.9	18
2	200	1	2282.8	93.8	21.4	18
2	200	1	2211.7	97.8	39.0	18
2	200	1	2220.3	99.9	29.8	18
2	200	1	2227.3	95.8	27.6	18
2	200	1	2280.3	97.7	27.7	18
2	200	1	2298.4	101.0	29.0	18
2	200	1	2375.4	102.1	23.8	18
2	200	1	2352.2	105.5	25.8	18
2	200	1	2343.4	91.8	27.8	18
2	200	1	2263.2	101.7	29.2	18
2	200	1	2456.8	101.1	37.3	18
2	200	1	2340.0	92.2	24.4	18
2	200	1	2361.6	92.9	24.9	18
2	200	1	2501.4	89.0	19.5	18
2	200	1	2256.5	94.1	27.2	18
2	300	1	4962.6	105.0	46.2	18
2	300	1	5154.3	97.9	28.5	18
2	300	1	5241.9	105.5	24.1	18
2	300	1	5149.6	94.6	41.0	18
2	300	1	5072.0	95.2	33.2	18

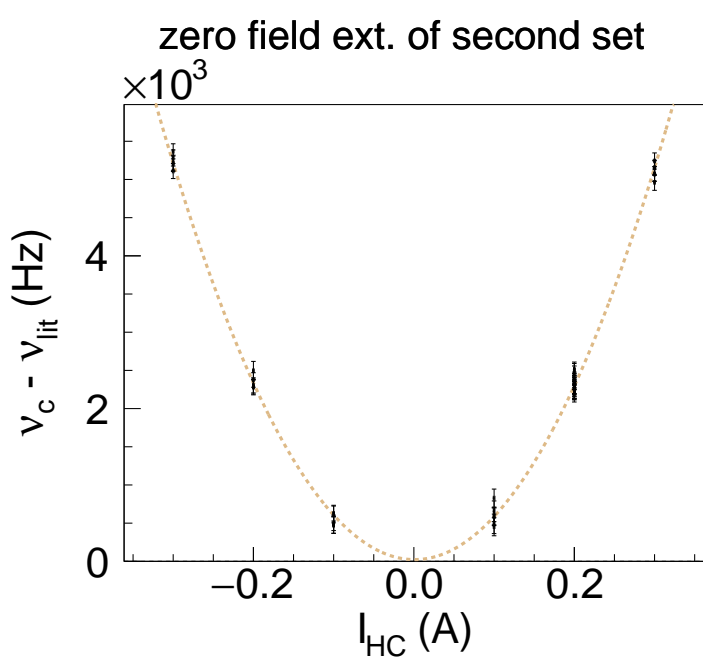


**Figure A.3** Zero field extrapolation; set number 2.

set	$I_{HC}$ (mA)	error (mA)	$\nu_c$ (Hz)	error (Hz)	$\chi^2$	<i>d.o.f.</i>
3	-100	1	680.1	48.6	47.9	23
3	-100	1	501.9	49.9	73.0	23
3	-100	1	568.8	48.7	34.2	23
3	-200	1	2358.2	49.5	50.6	23
3	-200	1	2360.2	49.6	38.1	23
3	-200	1	2297.7	49.4	31.9	23
3	-200	1	2344.4	48.3	48.1	23
3	-200	1	2297.3	49.7	42.8	23
3	-200	1	2378.9	50.0	44.8	23
3	-300	1	5238.1	48.7	25.2	23
3	-300	1	5252.1	48.3	43.9	23
3	-300	1	5324.2	45.6	28.3	23
3	-300	1	5257.3	48.1	42.6	23
3	-300	1	5215.2	48.0	43.1	23
3	-300	1	5295.1	50.8	33.0	23
3	100	1	500.2	49.6	51.6	23
3	100	1	598.4	48.0	36.1	23
3	100	1	721.7	48.0	76.9	23
3	200	1	2399.6	47.7	40.7	23
3	200	1	2408.3	50.1	42.2	23
3	200	1	2312.0	48.7	42.0	23
3	200	1	2209.2	51.7	38.3	23
3	200	1	2389.3	50.1	37.5	23
3	300	1	5291.9	51.2	37.3	23
3	300	1	5045.0	48.5	46.3	23
3	300	1	5218.9	49.4	40.4	23

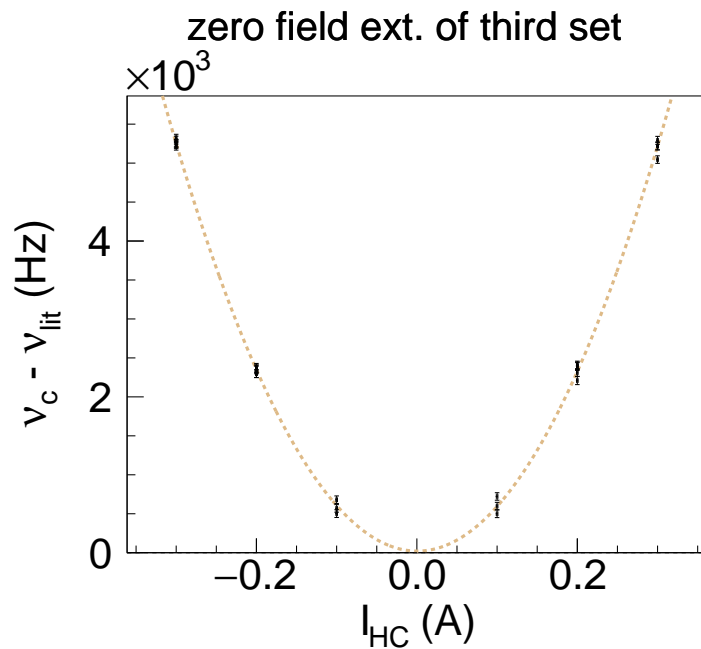


**Figure A.4** Zero field extrapolation; set number 3.

---

set	$I_{\text{HC}}$ (mA)	error (mA)	$\nu_c$ (Hz)	error (Hz)	$\chi^2$	d.o.f.
4	50.0397	0.0017	156.2	72.3	26.4	36
4	50.0389	0.0012	177.6	71.0	50.4	36
4	50.0387	0.0015	77.4	67.4	47.0	36
4	50.0399	0.0012	171.9	72.3	29.0	36
4	50.0394	0.0016	46.3	70.0	48.5	36
4	100.3351	0.0016	744.6	65.3	48.6	36
4	100.3353	0.0016	560.6	62.9	45.7	36
4	100.3358	0.0017	448.3	62.8	50.7	36
4	100.3366	0.0024	550.4	63.0	44.9	36
4	100.3376	0.0012	693.7	63.0	46.2	36
4	150.0028	0.0017	1309.4	73.1	57.7	36
4	150.0041	0.0012	1248.3	71.0	36.4	36
4	150.0039	0.0017	1366.7	74.3	43.7	36
4	150.0040	0.0018	1307.5	73.5	38.1	36
4	150.0062	0.0014	1380.3	73.8	32.6	36
4	200.0743	0.0015	2306.8	66.7	49.1	36
4	200.0736	0.0011	2333.0	65.4	39.9	36
4	200.0740	0.0019	2076.2	68.0	44.8	36
4	200.0746	0.0017	2327.8	67.5	30.5	36
4	200.0740	0.0012	2346.5	68.0	38.3	36
4	250.0090	0.0017	3613.2	67.0	52.8	36
4	250.0082	0.0017	3652.4	74.3	38.3	36
4	250.0088	0.0014	3600.5	69.7	32.3	36
4	250.0079	0.0018	3526.8	72.0	46.3	36
4	250.0080	0.0016	3584.1	70.0	23.3	36
4	299.9915	0.0020	5262.2	68.6	33.3	36
4	299.9921	0.0015	5181.8	75.8	29.2	36
4	299.9896	0.0020	5255.4	71.5	62.8	36
4	299.9902	0.0016	5094.8	75.4	41.7	36
4	299.9890	0.0016	5061.3	66.9	51.2	36
4	350.7493	0.0015	7057.4	69.8	52.2	36
4	350.7498	0.0018	7095.4	67.4	42.5	36
4	350.7492	0.0017	6952.7	68.7	44.5	36
4	350.7488	0.0013	7105.7	66.6	41.5	36
4	350.7483	0.0016	7076.0	68.9	58.3	36
4	400.0517	0.0026	9302.7	69.2	62.0	36
4	400.0390	0.0066	9336.3	71.4	48.6	36
4	400.0259	0.0022	9354.9	69.1	42.8	36
4	400.0186	0.0038	9134.7	70.7	47.7	36
4	400.0082	0.0045	9168.9	69.9	46.7	36
4	450.0036	0.0016	11802.2	75.1	31.6	36
4	450.0031	0.0014	11510.3	75.8	46.0	36
4	450.0016	0.0014	11737.6	72.3	35.7	36
4	450.0001	0.0021	11763.3	73.4	47.6	36
4	449.9996	0.0013	11768.7	75.6	55.4	36
4	500.0257	0.0020	14512.6	71.2	34.6	36
4	500.0240	0.0022	14556.7	73.5	21.6	36
4	500.0237	0.0017	14386.2	75.1	55.0	36
4	500.0218	0.0015	14356.9	74.0	46.1	36
4	500.0217	0.0015	14425.7	73.8	35.6	36

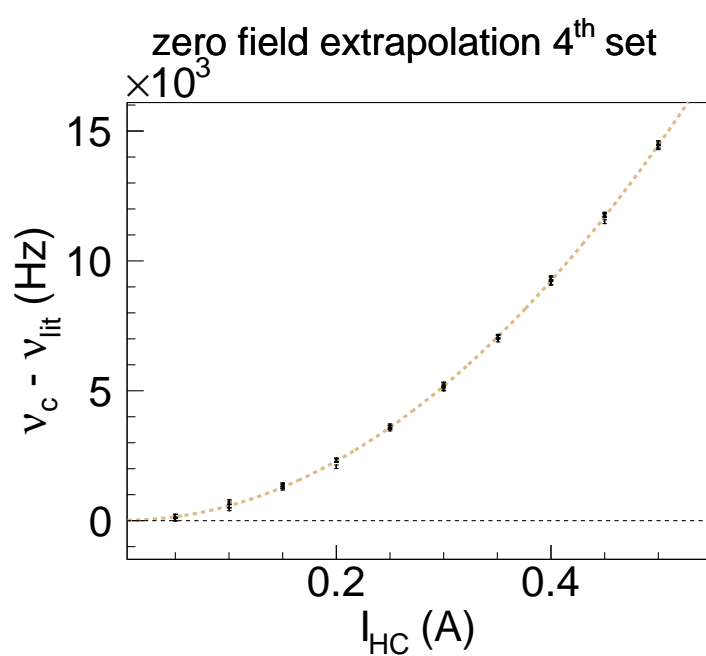


**Figure A.5** Zero field extrapolation; set number 4.

---

<b>set</b>	<b><math>I_{\text{HC}}</math> (mA)</b>	<b>error (mA)</b>	<b><math>\nu_c</math> (Hz)</b>	<b>error (Hz)</b>	<b><math>\chi^2</math></b>	<b><i>d.o.f.</i></b>
5	50.0068	0.0015	-75.1	123.3	32.2	36
5	50.0065	0.0014	249.9	127.2	46.1	36
5	50.0070	0.0012	206.5	122.1	24.3	36
5	50.0068	0.0017	14.2	120.1	33.8	36
5	50.0087	0.0014	401.0	131.2	23.9	36
5	150.0183	0.0016	1361.9	123.3	25.0	36
5	150.0172	0.0015	1186.7	112.6	42.9	36
5	150.0170	0.0015	1345.7	124.9	48.1	36
5	150.0161	0.0016	1536.6	116.5	37.5	36
5	150.0171	0.0015	1566.5	137.9	28.1	36
5	250.0219	0.0014	3871.5	116.3	43.4	36
5	250.0218	0.0015	3867.6	120.4	37.8	36
5	250.0217	0.0017	3574.2	129.7	43.4	36
5	250.0221	0.0019	3625.2	121.6	25.2	36
5	250.0239	0.0016	3510.5	126.4	35.2	36
5	350.0658	0.0021	7326.6	119.7	31.4	36
5	350.0648	0.0017	7094.8	113.7	23.0	36
5	350.0652	0.0014	7168.5	150.4	20.8	36
5	350.0638	0.0013	7132.4	113.8	40.6	36
5	350.0632	0.0013	6962.4	126.9	45.9	36
5	450.2111	0.0295	11636.0	130.5	23.9	36
5	450.2605	0.0116	11704.4	136.4	47.9	36
5	450.2798	0.0028	12062.9	121.7	43.8	36
5	450.2828	0.0018	11951.9	126.2	38.0	36
5	450.2821	0.0019	11803.2	125.2	27.5	36
5	549.8793	0.0154	17688.2	132.7	52.0	36
5	549.8390	0.0142	17574.2	124.3	34.2	36
5	549.7701	0.0199	17582.0	137.2	47.6	36
5	549.6992	0.0238	17621.3	134.3	49.2	36
5	549.6437	0.0115	17588.4	130.2	33.9	36
5	50.0056	0.0017	68.3	106.1	56.3	36
5	50.0071	0.0015	123.9	118.3	35.7	36
5	50.0064	0.0014	273.3	120.1	41.3	36
5	50.0066	0.0016	86.2	117.1	53.0	36
5	50.0057	0.0015	361.0	118.4	31.3	36
5	150.0669	0.0015	1152.3	133.0	30.8	36
5	150.0671	0.0012	1514.2	122.8	35.7	36
5	150.0666	0.0016	1212.9	109.3	39.6	36
5	150.0680	0.0015	1131.9	116.0	30.1	36
5	150.0669	0.0017	1345.6	115.8	35.4	36
5	250.0092	0.0016	3547.3	127.2	44.6	36
5	250.0091	0.0016	3612.7	123.2	25.4	36
5	250.0088	0.0020	3493.6	131.5	18.8	36
5	250.0095	0.0014	3560.8	122.2	35.4	36
5	250.0104	0.0017	3599.5	116.9	34.2	36
5	350.0392	0.0013	6863.3	114.4	53.6	36
5	350.0386	0.0017	7012.6	131.3	38.6	36
5	350.0392	0.0016	7020.5	119.5	37.6	36
5	350.0378	0.0018	7145.8	126.2	30.7	36
5	350.0377	0.0018	7255.0	124.3	46.5	36
5	450.0558	0.0016	11728.1	128.4	34.8	36
5	450.0551	0.0017	11557.7	129.4	32.0	36

---

5	450.0542	0.0016	11636.7	134.7	48.9	36
5	450.0538	0.0016	11524.8	140.0	32.3	36
5	450.0532	0.0015	11621.3	134.0	42.4	36
5	550.0275	0.0018	17612.9	121.5	47.8	36
5	550.0282	0.0017	17604.2	126.1	23.6	36
5	550.0290	0.0016	17509.7	119.6	32.5	36
5	550.0277	0.0017	17482.4	128.3	28.4	36
5	550.0281	0.0016	17691.1	119.4	33.3	36

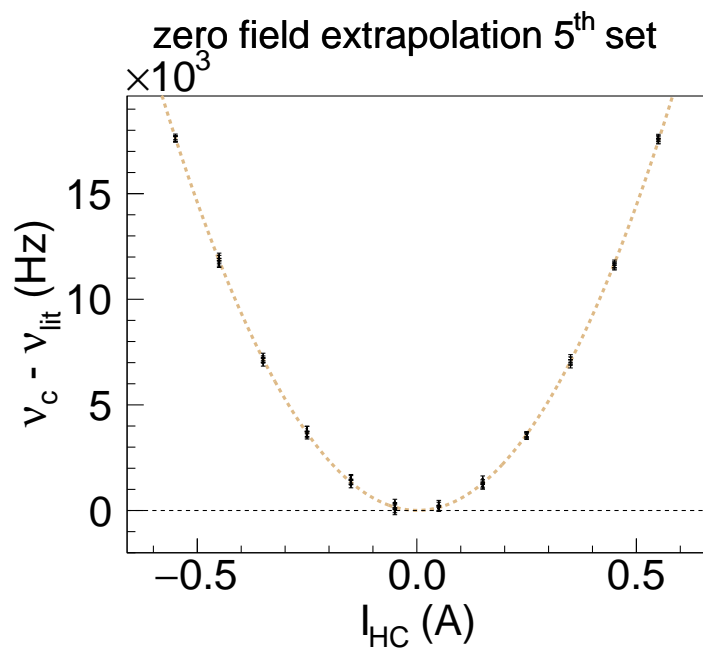


**Figure A.6** Zero field extrapolation; set number 5.

---

set	$I_{\text{HC}}$ (mA)	error (mA)	$\nu_c$ (Hz)	error (Hz)	$\chi^2$	d.o.f.
6	50.0002	0.0020	135.0	66.3	32.0	36
6	49.9989	0.0016	194.7	65.9	41.1	36
6	49.9994	0.0014	73.3	67.7	45.7	36
6	49.9990	0.0015	240.3	67.9	49.6	36
6	49.9996	0.0016	185.0	69.0	47.1	36
6	150.0568	0.0018	1271.0	62.9	50.7	36
6	150.0560	0.0016	1287.5	63.7	57.7	36
6	150.0548	0.0017	1219.3	62.9	34.8	36
6	150.0544	0.0018	1364.2	63.6	37.3	36
6	150.0545	0.0013	1306.6	65.9	30.9	36
6	250.0212	0.0022	3594.5	64.8	33.1	36
6	250.0217	0.0018	3736.2	63.1	41.7	36
6	250.0225	0.0016	3733.5	65.4	32.0	36
6	250.0234	0.0018	3708.2	66.0	31.1	36
6	250.0235	0.0017	3644.1	65.1	37.4	36
6	350.0197	0.0012	7140.3	66.3	49.7	36
6	350.0198	0.0013	7157.4	62.8	34.4	36
6	350.0184	0.0015	7230.2	61.8	40.2	36
6	350.0178	0.0016	7205.1	64.8	45.2	36
6	350.0174	0.0015	7125.2	63.1	39.1	36
6	450.0175	0.0030	11865.4	65.2	30.0	36
6	450.0219	0.0018	11789.1	64.1	56.2	36
6	450.0253	0.0018	11802.4	68.4	33.6	36
6	450.0266	0.0017	11801.6	63.6	50.7	36
6	450.0292	0.0014	11782.9	67.5	29.3	36
6	549.9989	0.0015	17687.2	63.3	59.5	36
6	549.9976	0.0015	17700.6	65.7	42.2	36
6	549.9972	0.0016	17734.0	65.2	30.6	36
6	549.9990	0.0018	17723.1	62.2	34.0	36
6	549.9992	0.0018	17588.5	62.6	34.7	36
6	50.0112	0.0021	116.9	65.0	34.4	36
6	50.0083	0.0017	155.6	66.1	35.0	36
6	50.0073	0.0015	78.6	61.6	43.7	36
6	50.0070	0.0013	106.7	66.6	51.6	36
6	50.0064	0.0016	72.7	67.4	37.3	36
6	150.0298	0.0014	1249.6	61.1	38.0	36
6	150.0301	0.0016	1233.1	63.4	37.6	36
6	150.0296	0.0017	1157.1	63.6	48.0	36
6	150.0302	0.0016	1367.4	65.2	49.2	36
6	150.0305	0.0017	1319.6	61.6	42.1	36
6	250.0429	0.0014	3596.9	66.0	44.6	36
6	250.0424	0.0013	3650.3	65.1	45.5	36
6	250.0440	0.0019	3579.1	65.1	40.5	36
6	250.0447	0.0017	3648.3	65.3	48.9	36
6	250.0436	0.0014	3671.3	62.1	41.9	36
6	349.9984	0.0013	7113.9	65.4	55.7	36
6	349.9979	0.0016	7075.4	64.7	43.3	36
6	349.9972	0.0014	7062.5	61.5	37.3	36
6	349.9962	0.0014	7041.9	64.8	42.5	36
6	349.9959	0.0015	6993.9	69.1	36.7	36
6	449.9895	0.0042	11777.7	65.4	48.4	36
6	449.9816	0.0016	11713.2	69.6	62.1	36

---

6	449.9778	0.0018	11718.4	67.7	36.0	36
6	449.9754	0.0017	11689.0	67.9	20.1	36
6	449.9726	0.0017	11783.4	68.6	46.7	36
6	550.0163	0.0020	17434.6	67.6	36.7	36
6	550.0141	0.0016	17551.0	68.0	58.1	36
6	550.0128	0.0016	17494.6	65.0	32.3	36
6	550.0137	0.0019	17297.1	68.7	38.1	36
6	550.0149	0.0017	17576.5	65.9	41.7	36

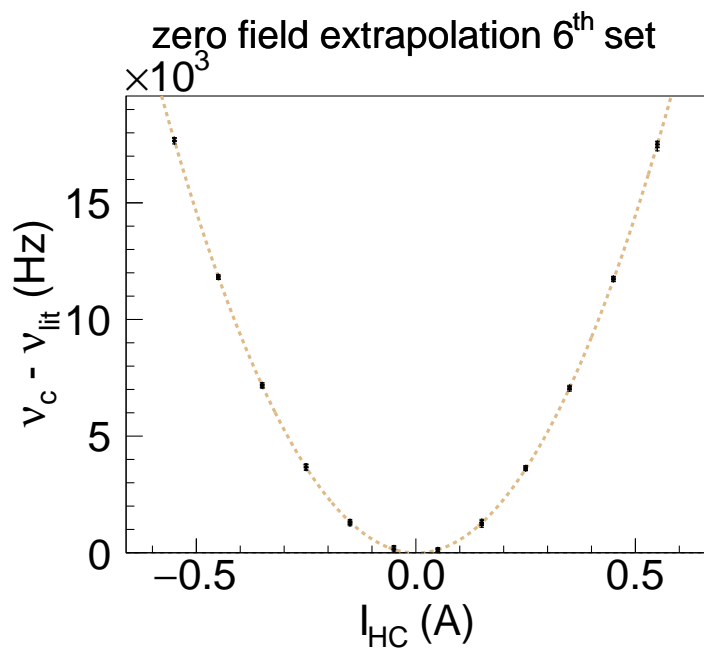


**Figure A.7** Zero field extrapolation; set number 6.

---

set	$I_{\text{HC}}$ (mA)	error (mA)	$\nu_c$ (Hz)	error (Hz)	$\chi^2$	<i>d.o.f.</i>
7	20.0138	0.0016	71.6	79.2	43.1	36
7	20.0123	0.0017	41.3	79.3	36.2	36
7	20.0121	0.0013	104.2	84.6	44.3	36
7	20.0126	0.0014	-6.2	79.2	29.4	36
7	20.0137	0.0016	141.2	78.0	35.2	36
7	50.0015	0.0011	91.2	81.4	39.3	36
7	50.0023	0.0016	199.5	89.6	44.2	36
7	50.0031	0.0016	51.8	84.0	40.5	36
7	50.0032	0.0019	111.1	79.8	33.2	36
7	50.0022	0.0015	83.7	79.1	52.6	36
7	80.0162	0.0017	357.7	79.8	44.1	36
7	80.0158	0.0015	459.6	80.5	24.1	36
7	80.0154	0.0017	353.4	80.4	30.3	36
7	80.0176	0.0017	505.7	83.3	28.8	36
7	80.0173	0.0019	389.7	92.8	34.1	36
7	130.0248	0.0019	936.6	86.1	44.1	36
7	130.0262	0.0013	1017.5	82.1	35.6	36
7	130.0256	0.0015	915.5	82.8	27.2	36
7	130.0253	0.0015	1075.8	81.8	35.0	36
7	130.0260	0.0020	1039.5	79.2	35.7	36
7	180.0233	0.0019	1887.4	81.0	36.7	36
7	180.0230	0.0014	1800.9	84.4	31.1	36
7	180.0220	0.0011	1804.9	81.9	40.1	36
7	180.0225	0.0012	1881.7	89.4	29.9	36
7	180.0216	0.0016	1824.7	82.7	66.1	36
7	250.0126	0.0016	3563.0	82.4	37.6	36
7	250.0151	0.0024	3594.2	87.3	44.9	36
7	250.0124	0.0015	3546.1	86.7	32.2	36
7	250.0099	0.0020	3711.9	87.1	24.6	36
7	250.0100	0.0019	3557.9	85.3	26.8	36
7	400.0270	0.0016	9211.6	82.7	40.9	36
7	400.0269	0.0019	9312.3	84.1	46.4	36
7	400.0269	0.0015	9184.8	80.9	46.7	36
7	400.0266	0.0015	9451.1	86.0	51.5	36
7	400.0260	0.0019	9197.9	82.0	38.6	36
7	550.0323	0.0019	17569.6	76.3	34.7	36
7	550.0320	0.0015	17675.4	81.5	43.8	36
7	550.0323	0.0021	17787.4	82.5	52.2	36
7	550.0328	0.0021	17602.9	81.6	53.1	36
7	550.0325	0.0018	17642.1	79.4	46.4	36
7	20.0162	0.0012	-48.9	84.1	45.9	36
7	20.0150	0.0014	65.8	75.8	33.5	36
7	20.0145	0.0014	-38.9	81.8	43.5	36
7	20.0143	0.0013	-27.3	85.3	49.1	36
7	20.0131	0.0013	-23.8	77.4	30.7	36
7	50.0153	0.0014	195.7	82.1	57.2	36
7	50.0155	0.0016	145.8	80.6	29.4	36
7	50.0129	0.0025	45.7	87.2	44.9	36
7	50.0149	0.0016	62.3	84.1	46.9	36
7	50.0138	0.0013	94.1	86.4	46.7	36
7	80.0297	0.0016	334.1	88.1	39.1	36
7	80.0293	0.0016	272.6	82.6	37.2	36

---

7	80.0300	0.0017	591.6	86.0	69.7	36
7	80.0305	0.0016	336.5	83.0	35.1	36
7	80.0303	0.0023	492.8	80.9	32.5	36
7	130.0078	0.0019	1046.7	81.1	27.6	36
7	130.0078	0.0016	1117.1	82.0	36.9	36
7	130.0072	0.0016	999.9	85.6	33.6	36
7	130.0089	0.0015	1034.2	80.9	52.2	36
7	130.0072	0.0018	1221.3	83.5	41.4	36
7	180.0230	0.0017	2120.3	85.1	46.2	36
7	180.0235	0.0016	1680.3	87.8	38.8	36
7	180.0240	0.0015	1900.8	86.6	42.8	36
7	180.0250	0.0012	2030.9	81.9	35.4	36
7	180.0240	0.0025	1797.7	84.8	24.5	36
7	250.0494	0.0019	3591.8	82.3	28.9	36
7	250.0495	0.0015	3800.5	83.1	36.1	36
7	250.0494	0.0019	3805.1	81.9	26.7	36
7	250.0501	0.0018	3699.0	79.8	51.1	36
7	250.0496	0.0016	3457.3	84.5	40.5	36
7	400.0047	0.0014	9388.2	80.6	30.8	36
7	400.0044	0.0015	9455.5	80.2	27.7	36
7	400.0047	0.0019	9440.6	83.7	43.7	36
7	400.0046	0.0018	9471.1	84.5	30.1	36
7	400.0043	0.0015	9372.4	81.0	42.5	36
7	550.0257	0.0024	17684.4	84.9	40.1	36
7	550.0207	0.0017	17804.8	85.5	47.1	36
7	550.0204	0.0019	17581.6	86.9	34.7	36
7	550.0199	0.0020	17542.1	77.8	36.3	36
7	550.0204	0.0018	17569.3	84.3	41.4	36

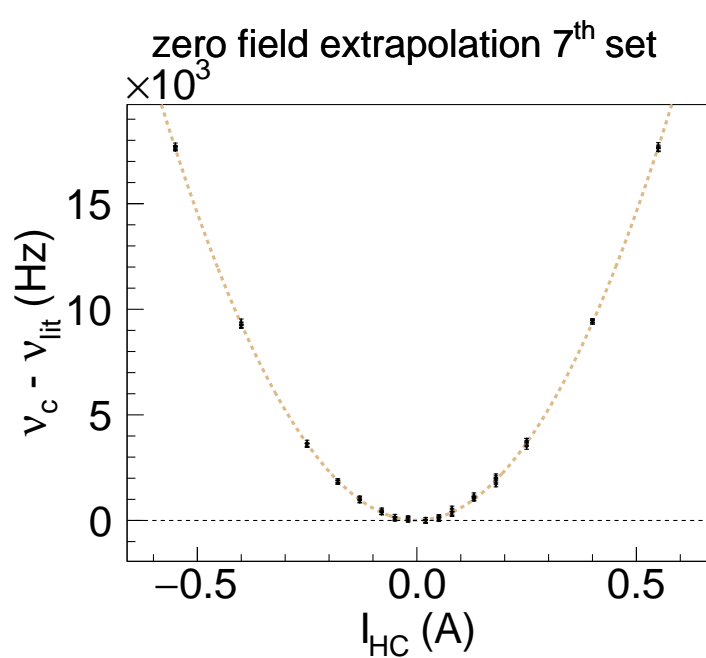


**Figure A.8** Zero field extrapolation; set number 7.

---

set	$I_{\text{HC}}$ (mA)	error (mA)	$\nu_c$ (Hz)	error (Hz)	$\chi^2$	d.o.f.
8	20.0137	0.0013	28.3	65.4	31.8	36
8	20.0117	0.0017	-40.8	67.0	49.8	36
8	20.0095	0.0026	-81.5	69.9	25.7	36
8	20.0102	0.0021	11.5	68.6	57.7	36
8	20.0086	0.0024	-11.8	68.7	56.7	36
8	50.0293	0.0015	133.5	64.9	23.0	36
8	50.0279	0.0010	164.9	64.3	37.6	36
8	50.0270	0.0014	104.5	63.2	59.6	36
8	50.0276	0.0013	159.2	64.8	35.2	36
8	50.0265	0.0016	164.3	70.6	23.3	36
8	80.0116	0.0014	389.5	68.2	54.4	36
8	80.0115	0.0014	353.1	65.7	37.9	36
8	80.0117	0.0018	362.1	63.1	31.1	36
8	80.0131	0.0017	461.8	65.6	54.0	36
8	80.0135	0.0016	442.7	66.9	43.7	36
8	130.0153	0.0012	978.6	66.8	52.1	36
8	130.0158	0.0014	1091.6	73.1	32.9	36
8	130.0158	0.0018	837.9	70.3	35.7	36
8	130.0154	0.0014	982.0	65.1	41.9	36
8	130.0147	0.0013	1162.9	69.0	42.7	36
8	180.0158	0.0015	1954.7	65.4	43.1	36
8	180.0154	0.0014	1722.4	71.4	43.1	36
8	180.0141	0.0015	1889.3	64.9	49.9	36
8	180.0147	0.0017	1981.1	63.1	37.4	36
8	180.0147	0.0015	1798.9	67.9	40.6	36
8	250.0237	0.0016	3809.0	67.0	40.7	36
8	250.0219	0.0016	3560.2	66.6	42.9	36
8	250.0232	0.0018	3771.9	67.3	38.6	36
8	250.0223	0.0014	3656.5	66.3	37.3	36
8	250.0224	0.0015	3632.8	66.3	58.7	36
8	400.4124	0.2370	9306.0	69.9	31.3	36
8	400.9439	0.0524	9326.0	69.0	40.5	36
8	401.0396	0.0153	9290.6	64.0	35.9	36
8	401.0721	0.0049	9337.1	68.5	33.4	36
8	401.0845	0.0025	9413.4	67.1	38.8	36
8	550.0420	0.0022	17622.6	69.9	41.4	36
8	550.0401	0.0017	17573.5	65.0	46.1	36
8	550.0381	0.0018	17506.9	68.0	33.8	36
8	550.0371	0.0018	17746.4	64.0	37.2	36
8	550.0374	0.0017	17577.9	63.9	51.4	36
8	20.0100	0.0014	-57.4	66.6	36.3	36
8	20.0090	0.0011	-36.4	62.5	49.5	36
8	20.0078	0.0014	64.0	63.3	40.7	36
8	20.0063	0.0012	3.7	66.3	43.3	36
8	20.0056	0.0015	96.9	68.9	30.2	36
8	50.0058	0.0015	122.6	66.3	30.2	36
8	50.0057	0.0013	61.4	66.5	34.6	36
8	50.0054	0.0015	157.3	66.0	31.2	36
8	50.0056	0.0016	135.0	69.0	43.6	36
8	50.0058	0.0018	87.3	64.8	32.0	36
8	80.0310	0.0015	295.7	67.7	44.3	36
8	80.0316	0.0015	453.6	64.2	34.0	36

---

8	80.0320	0.0016	389.5	66.4	34.6	36
8	80.0305	0.0018	322.6	68.3	38.0	36
8	80.0307	0.0019	360.9	66.1	37.3	36
8	130.0271	0.0022	936.8	61.4	33.0	36
8	130.0271	0.0015	941.4	67.2	45.6	36
8	130.0263	0.0015	887.0	71.8	37.3	36
8	130.0268	0.0015	1037.3	64.8	47.2	36
8	130.0275	0.0015	961.2	63.5	41.9	36
8	180.0196	0.0013	1879.2	66.1	44.9	36
8	180.0208	0.0012	1900.1	66.1	29.4	36
8	180.0201	0.0012	1875.4	70.8	46.0	36
8	180.0209	0.0014	1825.1	63.8	47.1	36
8	180.0216	0.0014	2010.8	69.8	32.3	36
8	250.0257	0.0015	3609.0	65.5	36.7	36
8	250.0244	0.0016	3686.5	69.4	28.4	36
8	250.0247	0.0019	3736.2	69.3	40.8	36
8	250.0254	0.0016	3706.4	67.5	52.3	36
8	250.0250	0.0020	3789.7	69.5	40.9	36
8	400.0091	0.0020	9341.8	67.6	43.5	36
8	400.0089	0.0015	9350.7	63.8	40.9	36
8	400.0101	0.0014	9441.5	64.4	37.9	36
8	400.0090	0.0016	9424.8	61.3	32.4	36
8	400.0092	0.0014	9401.8	66.8	46.7	36
8	549.9786	0.0080	17699.1	66.0	38.4	36
8	549.9630	0.0038	17757.8	64.6	38.9	36
8	549.9561	0.0018	17755.5	66.1	50.5	36
8	549.9522	0.0016	17760.8	66.2	41.7	36
8	549.9507	0.0011	17652.2	65.2	33.3	36

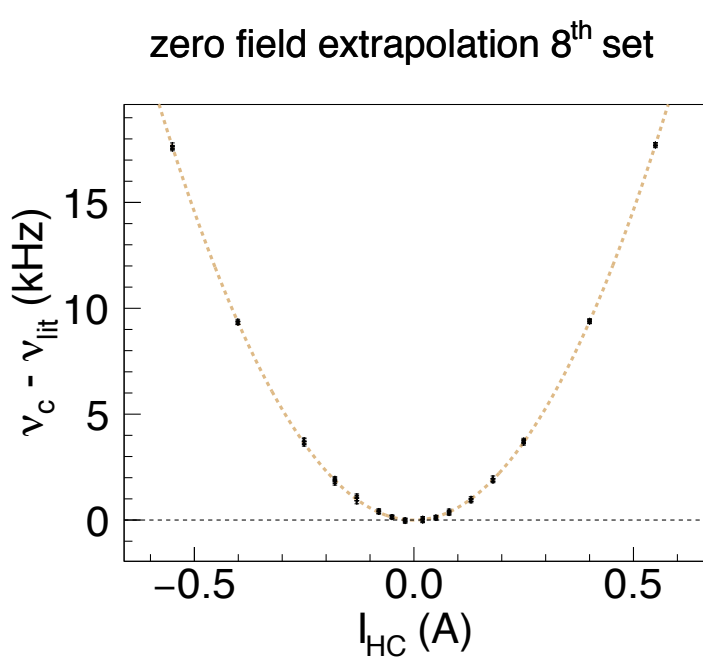


**Figure A.9** Zero field extrapolation; set number 8.

---

set	$I_{\text{HC}}$ (mA)	error (mA)	$\nu_{\text{c}}$ (Hz)	error (Hz)	$\chi^2$	d.o.f.
9	49.9556	0.0017	117.5	32.1	86.5	36
9	49.9547	0.0013	141.1	33.4	85.6	36
9	49.9532	0.0011	151.2	34.2	57.7	36
9	49.9533	0.0013	147.1	33.6	74.1	36
9	49.9544	0.0015	108.0	32.8	65.7	36
9	100.0596	0.0019	610.0	29.7	90.6	36
9	100.0584	0.0014	588.0	29.4	77.3	36
9	100.0585	0.0018	595.7	29.8	69.1	36
9	100.0586	0.0014	554.9	30.2	93.1	36
9	100.0587	0.0015	558.5	30.0	82.1	36
9	250.0353	0.0015	3620.3	34.9	69.9	36
9	250.0351	0.0012	3686.5	34.6	58.3	36
9	250.0359	0.0014	3614.3	35.6	74.5	36
9	250.0353	0.0019	3623.1	35.4	71.0	36
9	250.0355	0.0016	3651.7	35.1	66.6	36
9	350.0079	0.0017	7076.8	32.0	82.0	36
9	350.0063	0.0015	7181.6	31.7	49.1	36
9	350.0060	0.0021	7164.0	31.7	111.9	36
9	350.0067	0.0015	7185.4	31.3	63.6	36
9	350.0070	0.0015	7120.5	31.2	77.7	36
9	400.0376	0.0040	9327.5	34.2	89.6	36
9	400.0334	0.0013	9276.2	34.4	81.7	36
9	400.0324	0.0018	9349.8	33.3	66.2	36
9	400.0308	0.0016	9288.8	33.5	61.4	36
9	400.0288	0.0018	9316.5	33.8	48.9	36
9	550.0142	0.0084	17639.3	30.5	90.4	36
9	550.0114	0.0016	17564.6	29.9	67.7	36
9	550.0119	0.0017	17607.4	30.2	92.7	36
9	550.0121	0.0012	17624.9	29.5	68.0	36
9	550.0104	0.0021	17612.8	30.1	74.4	36
9	50.0423	0.0015	177.2	38.0	63.9	36
9	50.0434	0.0014	125.3	38.6	61.6	36
9	50.0435	0.0015	120.0	38.4	74.1	36
9	50.0431	0.0019	173.9	39.0	56.8	36
9	50.0426	0.0015	102.8	37.2	44.9	36
9	100.0736	0.0018	521.9	75.0	45.4	36
9	100.0740	0.0017	424.6	80.7	50.5	36
9	100.0735	0.0014	555.7	74.5	55.2	36
9	100.0750	0.0017	652.5	83.6	67.2	36
9	100.0748	0.0016	619.1	79.1	48.0	36
9	250.0229	0.0016	3638.1	39.0	60.8	36
9	250.0221	0.0014	3612.2	38.2	85.7	36
9	250.0214	0.0014	3538.8	39.8	55.6	36
9	250.0217	0.0014	3616.4	38.4	46.6	36
9	250.0209	0.0014	3703.9	38.4	80.0	36
9	350.0024	0.0020	7177.4	33.0	71.7	36
9	350.0026	0.0016	7168.7	33.1	69.3	36
9	350.0036	0.0016	7213.9	33.2	59.8	36
9	350.0033	0.0014	7092.0	33.5	51.4	36
9	350.0042	0.0016	7138.3	33.6	88.0	36
9	400.0120	0.0017	9384.4	37.5	41.0	36
9	400.0108	0.0013	9303.6	37.4	72.0	36

---

9	400.0106	0.0015	9346.8	37.3	57.4	36
9	400.0105	0.0017	9423.6	37.8	50.1	36
9	400.0107	0.0014	9335.7	37.9	47.9	36
9	550.0420	0.0015	17780.2	33.1	53.6	36
9	550.0414	0.0015	17680.5	32.3	59.3	36
9	550.0408	0.0014	17729.6	32.6	57.6	36
9	550.0396	0.0015	17753.9	33.2	85.7	36
9	550.0394	0.0016	17659.5	32.5	51.7	36

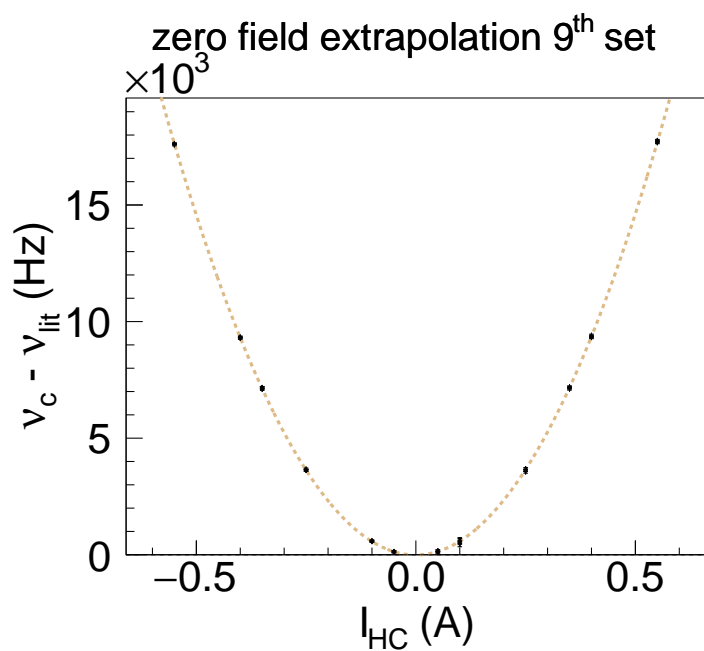


**Figure A.10** Zero field extrapolation; set number 9.

---

set	$I_{HC}$ (mA)	error (mA)	$\nu_c$ (Hz)	error (Hz)	$\chi^2$	d.o.f.
10	49.9929	0.0020	151.5	35.8	62.4	36
10	49.9917	0.0015	142.6	35.1	79.2	36
10	49.9910	0.0015	178.6	34.0	78.8	36
10	49.9910	0.0014	105.6	34.0	59.2	36
10	49.9906	0.0012	39.1	34.0	59.5	36
10	100.0218	0.0017	581.8	35.6	56.6	36
10	100.0220	0.0014	538.0	36.0	78.9	36
10	100.0213	0.0017	580.5	35.1	63.0	36
10	100.0205	0.0016	630.3	35.3	52.3	36
10	100.0201	0.0018	591.6	34.4	65.6	36
10	250.0753	0.0016	3697.1	35.3	64.6	36
10	250.0746	0.0013	3647.7	34.5	61.3	36
10	250.0753	0.0017	3650.3	35.5	74.6	36
10	250.0755	0.0018	3666.6	34.6	62.7	36
10	250.0755	0.0015	3618.0	35.7	78.2	36
10	349.9681	0.0015	7134.4	34.7	105.0	36
10	349.9681	0.0014	7119.9	35.0	78.2	36
10	349.9680	0.0014	7148.2	35.8	64.9	36
10	349.9681	0.0019	7110.7	34.2	46.5	36
10	349.9687	0.0014	7066.7	35.2	48.1	36
10	400.0009	0.0019	9292.6	34.9	36.4	36
10	399.9976	0.0018	9341.9	35.0	63.8	36
10	399.9975	0.0020	9302.5	35.0	60.5	36
10	399.9974	0.0016	9257.1	35.2	87.5	36
10	399.9977	0.0018	9314.5	35.4	84.8	36
10	551.8833	0.0015	17727.5	34.8	88.0	36
10	551.8813	0.0015	17753.1	34.4	76.5	36
10	551.8803	0.0018	17741.3	34.9	66.9	36
10	551.8799	0.0016	17779.1	35.9	70.6	36
10	551.8802	0.0015	17771.3	35.2	76.3	36
10	50.0491	0.0013	158.7	33.2	61.0	36
10	50.0495	0.0013	154.6	33.2	57.3	36
10	50.0498	0.0013	85.3	33.0	67.1	36
10	50.0505	0.0015	93.9	34.3	51.7	36
10	50.0507	0.0014	129.9	32.3	67.5	36
10	100.0137	0.0018	562.6	33.3	62.2	36
10	100.0148	0.0015	634.2	33.0	59.6	36
10	100.0158	0.0015	582.0	32.9	62.7	36
10	100.0156	0.0017	643.5	32.5	67.4	36
10	100.0160	0.0015	612.1	32.9	58.4	36
10	249.9944	0.0021	3663.8	31.9	87.3	36
10	249.9947	0.0012	3699.5	32.1	85.7	36
10	249.9952	0.0017	3668.4	31.3	70.6	36
10	249.9951	0.0018	3642.9	32.3	81.1	36
10	249.9929	0.0016	3687.6	32.0	66.7	36
10	350.0706	0.0021	7130.4	32.8	63.6	36
10	350.0681	0.0014	7181.1	32.3	52.3	36
10	350.0666	0.0016	7196.1	33.1	51.0	36
10	350.0656	0.0016	7185.9	33.6	86.0	36
10	350.0661	0.0019	7185.5	33.1	68.5	36
10	400.0122	0.0015	9347.8	32.7	71.7	36
10	400.0105	0.0024	9401.4	32.9	62.3	36

---

10	400.0102	0.0020	9339.0	32.3	45.8	36
10	400.0081	0.0019	9326.6	33.3	74.0	36
10	400.0070	0.0017	9396.0	33.3	57.8	36
10	550.0378	0.0037	17681.4	33.3	99.2	36
10	550.0357	0.0016	17762.8	33.0	87.2	36
10	550.0346	0.0018	17691.4	31.9	56.1	36
10	550.0354	0.0014	17728.0	32.2	76.7	36
10	550.0345	0.0019	17676.3	32.2	78.5	36

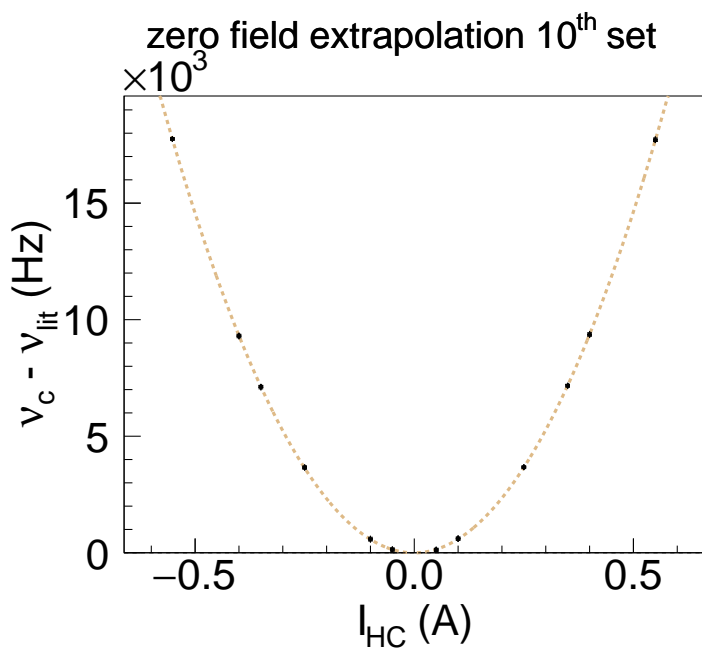


**Figure A.11** Zero field extrapolation; set number 10.

# Bibliography

- [1] Lüders, G. Proof of the TCP theorem. *Annals of Physics* **2**, 1 – 15 (1957). URL <http://www.sciencedirect.com/science/article/pii/0003491657900325>.
- [2] Sakharov, A. D. Violation of CP invariance, C asymmetry, and baryon asymmetry of the universe. *Soviet Physics Uspekhi* **34**, 392 (1991). URL <http://stacks.iop.org/0038-5670/34/i=5/a=A08>.
- [3] Colladay, D. & Kostelecký, V. A. CPT violation and the standard model. *Phys. Rev. D* **55**, 6760–6774 (1997). URL <http://link.aps.org/doi/10.1103/PhysRevD.55.6760>.
- [4] Colladay, D. & Kostelecký, V. A. Lorentz-violating extension of the standard model. *Phys. Rev. D* **58**, 116002 (1998). URL <http://link.aps.org/doi/10.1103/PhysRevD.58.116002>.
- [5] Widmann, E. *et al.* *The Hydrogen Atom: Precision Physics of Simple Atomic Systems*, chap. Hyperfine Structure Measurements of Antiprotonic Helium and Antihydrogen, 528–542 (Springer Berlin Heidelberg, Berlin, Heidelberg, 2001). URL [http://dx.doi.org/10.1007/3-540-45395-4\\_36](http://dx.doi.org/10.1007/3-540-45395-4_36).
- [6] Eades, J. *et al.* Measurement of the Antihydrogen Hyperfine Structure. Tech. Rep. CERN-SPSC-2003-009. SPSC-I-226, CERN, Geneva (2003). URL <http://cds.cern.ch/record/606343>.
- [7] ASACUSA collaboration. Atomic spectroscopy and collisions using slow antiprotons. *CERN-SPSC* **2005-002** (2005).
- [8] Widmann, E. *et al.* Measurement of the hyperfine structure of antihydrogen in a beam. *Hyperfine Interactions* **215**, 1–8 (2013). URL <http://dx.doi.org/10.1007/s10751-013-0809-6>.

## Bibliography

---

- [9] Lee, T. D. & Yang, C. N. Question of parity conservation in weak interactions. *Phys. Rev.* **104**, 254–258 (1956). URL <http://link.aps.org/doi/10.1103/PhysRev.104.254>.
- [10] Wu, C. S., Ambler, E., Hayward, R. W., Hoppes, D. D. & Hudson, R. P. Experimental test of parity conservation in beta decay. *Phys. Rev.* **105**, 1413–1415 (1957). URL <http://link.aps.org/doi/10.1103/PhysRev.105.1413>.
- [11] Christenson, J. H., Cronin, J. W., Fitch, V. L. & Turlay, R. Evidence for the  $2\pi$  decay of the  $k_2^0$  meson. *Phys. Rev. Lett.* **13**, 138–140 (1964). URL <http://link.aps.org/doi/10.1103/PhysRevLett.13.138>.
- [12] Cronin, J. W. *Nishina Memorial Lectures: Creators of Modern Physics*, chap. The Experimental Discovery of CP Violation, 261–280 (Springer Japan, Tokyo, 2008). URL [http://dx.doi.org/10.1007/978-4-431-77056-5\\_12](http://dx.doi.org/10.1007/978-4-431-77056-5_12).
- [13] Kostelecký, V. A. & Samuel, S. Spontaneous breaking of lorentz symmetry in string theory. *Phys. Rev. D* **39**, 683–685 (1989). URL <http://link.aps.org/doi/10.1103/PhysRevD.39.683>.
- [14] Alan Kostelecký, V. & Potting, R. CPT and strings. *Nuclear Physics B* **359**, 545–570 (1991). URL <http://www.sciencedirect.com/science/article/pii/0550321391900715>.
- [15] Bertolami, O., Colladay, D., Kostelecký, V. A. & Potting, R. Cpt violation and baryogenesis. *Physics Letters B* **395**, 178–183 (1997). URL <http://www.sciencedirect.com/science/article/pii/S0370269397000622>.
- [16] Greenberg, O. W. *cpt* violation implies violation of lorentz invariance. *Phys. Rev. Lett.* **89**, 231602 (2002). URL <http://link.aps.org/doi/10.1103/PhysRevLett.89.231602>.
- [17] Olive, K. A. *et al.* Review of Particle Physics. *Chin. Phys.* **C38**, 090001 (2014).
- [18] Fee, M. S. *et al.* Measurement of the positronium  $1\ ^3s_1$ – $2\ ^3s_1$  interval by continuous-wave two-photon excitation. *Phys. Rev. A* **48**, 192–219 (1993). URL <http://link.aps.org/doi/10.1103/PhysRevA.48.192>.
- [19] Cresti, M., Pasquali, P., Peruzzo, L., Pinori, C. & Sartori, G. Measurement of the antineutron mass. *Physics Letters B* **177**, 206 (1986).

[20] Bressani, T. & Filippi, A. Antineutron physics. *Physics Reports* **383**, 213 – 297 (2003). URL <http://www.sciencedirect.com/science/article/pii/S0370157303002333>.

[21] Hori, M. *et al.* Two-photon laser spectroscopy of antiprotonic helium and the antiproton-to-electron mass ratio. *Nature* **475**, 484–488 (2011). URL <http://dx.doi.org/10.1038/nature10260>.

[22] Schwingenheuer, B. *et al.* *CPT* tests in the neutral kaon system. *Phys. Rev. Lett.* **74**, 4376–4379 (1995). URL <http://link.aps.org/doi/10.1103/PhysRevLett.74.4376>.

[23] Parthey, C. G. *et al.* Improved measurement of the hydrogen  $1s - 2s$  transition frequency. *Phys. Rev. Lett.* **107**, 203001 (2011). URL <http://link.aps.org/doi/10.1103/PhysRevLett.107.203001>.

[24] Hellwig, H. *et al.* Measurement of the unperturbed hydrogen hyperfine transition frequency. *IEEE Transactions on Instrumentation and Measurement* **19**, 200–209 (1970).

[25] Essen, L., Donaldson, R., Bangham, M. & Hope, E. Frequency of the hydrogen maser. *Nature* **229**, 110 (1971).

[26] Karshenboim, S. G. Some possibilities for laboratory searches for variations of fundamental constants. *Canadian Journal of Physics* **78**, 639–678 (2000). URL <http://www.nrcresearchpress.com/doi/abs/10.1139/p00-045>.

[27] Hertel, I. V. & Schulz, C.-P. *Atome, Moleküle und optische Physik*, vol. 1 (Springer, Berlin Heidelberg, 2008).

[28] Bluhm, R., Kostelecký, V. A. & Russell, N. *CPT* and lorentz tests in hydrogen and antihydrogen. *Phys. Rev. Lett.* **82**, 2254–2257 (1999). URL <http://link.aps.org/doi/10.1103/PhysRevLett.82.2254>.

[29] Kostelecký, V. A. & Vargas, A. J. Lorentz and *cpt* tests with hydrogen, antihydrogen, and related systems. *Phys. Rev. D* **92**, 056002 (2015). URL <http://link.aps.org/doi/10.1103/PhysRevD.92.056002>.

[30] Volotka, V. A., Shabaev, M. V., Plunien, G. & Soff, G. Zemach and magnetic radius of the proton from the hyperfine splitting in hydrogen. *The European Physical*

## Bibliography

---

*Journal D - Atomic, Molecular, Optical and Plasma Physics* **33**, 23–27 (2005). URL <http://dx.doi.org/10.1140/epjd/e2005-00025-9>.

[31] Carlson, C. E., Nazaryan, V. & Griffioen, K. Proton structure corrections to electronic and muonic hydrogen hyperfine splitting. *Phys. Rev. A* **78**, 022517 (2008). URL <http://link.aps.org/doi/10.1103/PhysRevA.78.022517>.

[32] Sapirstein, J. R. & Yennie, D. R. *THEORY OF HYDROGENIC BOUND STATES*, vol. 7, 560–672 (WORLD SCIENTIFIC, 1990). URL [http://dx.doi.org/10.1142/9789814503273\\_0012](http://dx.doi.org/10.1142/9789814503273_0012).

[33] I. Eides, M., Grotch, H. & Shelyuto, V. A. Theory of light hydrogenlike atoms. *Physics Reports* **342**, 63–261 (2001). URL <http://www.sciencedirect.com/science/article/pii/S0370157300000776>.

[34] Rabi, I. I., Millman, S., Kusch, P. & Zacharias, J. R. The molecular beam resonance method for measuring nuclear magnetic moments. the magnetic moments of  ${}_3\text{Li}^6$ ,  ${}_3\text{Li}^7$  and  ${}_9\text{F}^{19}$ . *Phys. Rev.* **55**, 526–535 (1939). URL <http://link.aps.org/doi/10.1103/PhysRev.55.526>.

[35] Kusch, P. Redetermination of the hyperfine splittings of hydrogen and deuterium in the ground state. *Phys. Rev.* **100**, 1188–1190 (1955). URL <http://link.aps.org/doi/10.1103/PhysRev.100.1188>.

[36] Wittke, J. P. & Dicke, R. H. Redetermination of the hyperfine splitting in the ground state of atomic hydrogen. *Phys. Rev.* **103**, 620–631 (1956). URL <http://link.aps.org/doi/10.1103/PhysRev.103.620>.

[37] Kolbinger, B. *Numerical Simulations of Hyperfine Transitions in Antihydrogen*. Master’s thesis, University of Vienna (2014).

[38] Breit, G. & Rabi, I. I. Measurement of nuclear spin. *Phys. Rev.* **38**, 2082–2083 (1931). URL <http://link.aps.org/doi/10.1103/PhysRev.38.2082.2>.

[39] Kolbinger, B. *et al.* Numerical simulations of hyperfine transitions of antihydrogen. *Hyperfine Interactions* **233**, 47–51 (2015). URL <http://dx.doi.org/10.1007/s10751-015-1130-3>.

[40] Mohr, P. J., Taylor, B. N. & Newell, D. B. Codata recommended values of the fundamental physical constants: 2006. *Rev. Mod. Phys.* **80**, 633–730 (2008). URL <http://link.aps.org/doi/10.1103/RevModPhys.80.633>.

- [41] Bethe, H. A. & Salpeter, E. E. *Quantum Mechanics of One- and Two-Electron Atoms* (Springer-Verlag, 1957).
- [42] Foot, C. J. *Atomic Physics* (Oxford University Press, 2005), oxford master series in atomic, optical and laser physics edn.
- [43] Ramsey, N. F. Experiments with separated oscillatory fields and hydrogen masers. *Rev. Mod. Phys.* **62**, 541–552 (1990). URL <http://link.aps.org/doi/10.1103/RevModPhys.62.541>.
- [44] Hayano, R. S., Hori, M., Horváth, D. & Widmann, E. Antiprotonic helium and cpt invariance. *Reports on Progress in Physics* **70**, 1995 (2007). URL <http://stacks.iop.org/0034-4885/70/i=12/a=R01>.
- [45] Belochitskii, P., Eriksson, T. & Maury. The CERN antiproton decelerator (AD) in 2002: status, progress and machine development results. *Nuclear Instruments and Methods in Physics Research B* **214**, 176–180 (2004).
- [46] Baird, S. *et al.* Status of the antiproton decelerator: AD. *Nuclear Physics B - Proceedings Supplements* **56**, 349 – 357 (1997). URL <http://www.sciencedirect.com/science/article/pii/S0920563297002971>. Proceedings of the Fourth Biennial Conference on Low Energy Antiproton Physics.
- [47] Bylinsky, Y., Lombardi, A. M. & Pirkl, W. RFQD: A 'Decelerating' radio frequency quadrupole for the CERN anti-proton facility. *eConf* **C000821**, TUD05 (2000). [,554(2000)], [hep-ex/0008030](https://arxiv.org/abs/hep-ex/0008030).
- [48] Kuroda, N. *et al.* Development of a monoenergetic ultraslow antiproton beam source for high-precision investigation. *Phys. Rev. ST Accel. Beams* **15**, 024702 (2012). URL <http://link.aps.org/doi/10.1103/PhysRevSTAB.15.024702>.
- [49] Bartmann, W. *et al.* Past, present and future low energy antiproton facilities at CERN. *International Journal of Modern Physics: Conference Series* **30**, 1460261 (2014). URL <http://dx.doi.org/10.1142/S2010194514602610>.
- [50] Enomoto, Y. *et al.* Synthesis of cold antihydrogen in a cusp trap. *Phys. Rev. Lett.* **105**, 243401 (2010). URL <http://link.aps.org/doi/10.1103/PhysRevLett.105.243401>.

[51] Imao, H. *et al.* Positron accumulation and manipulation for antihydrogen synthesis. *Journal of Physics: Conference Series* **225**, 012018 (2010). URL <http://stacks.iop.org/1742-6596/225/i=1/a=012018>.

[52] Mohri, A. & Yamazaki, Y. A possible new scheme to synthesize antihydrogen and to prepare a polarised antihydrogen beam. *EPL (Europhysics Letters)* **63**, 207 (2003). URL <http://stacks.iop.org/0295-5075/63/i=2/a=207>.

[53] Kuroda, N. *et al.* A source of antihydrogen for in-flight hyperfine spectroscopy. *Nat Commun* **5**, 1–6 (2014). URL <http://dx.doi.org/10.1038/ncomms4089>.

[54] Kuroda, N. *et al.* Towards a spin polarized antihydrogen beam. *Hyperfine Interactions* **228**, 67–76 (2014). URL <http://dx.doi.org/10.1007/s10751-014-1016-9>.

[55] Nagata, Y. & Yamazaki, Y. A novel property of anti-helmholz coils for in-coil syntheses of antihydrogen atoms: formation of a focused spin-polarized beam. *New Journal of Physics* **16**, 083026 (2014). URL <http://stacks.iop.org/1367-2630/16/i=8/a=083026>.

[56] Juhász, B., Widmann, E. & Federmann, S. Measurement of the ground-state hyperfine splitting of antihydrogen. *Journal of Physics: Conference Series* **335**, 12059–12066 (2011-12-28T00:00:00). URL <http://www.ingentaconnect.com/content/iop/jpcs/2011/00000335/00000001/art012059>.

[57] Diermaier, M. *Design and construction of a monoatomic hydrogen beam*. Master's thesis, Universität Wien (2012).

[58] McCullough, R. W. *et al.* A new microwave discharge source for reactive atom beams. *Measurement Science and Technology* **4**, 79 (1993). URL <http://stacks.iop.org/0957-0233/4/i=1/a=013>.

[59] McCullough, R. W., Geddes, J., Donnelly, A., Liehr, M. & Gilbody, H. B. A new reactive atom beam source for accelerator target studies. *Nuclear Instruments and Methods in Physics Research B* **79**, 708–710 (1993).

[60] McCullough, R. W. Characterisation and applications of a new reactive atom beam source. In *American Institute of Physics Conference Series*, vol. 392 of *American Institute of Physics Conference Series*, 275–278 (1997).

- [61] Goebel, D. M. & Katz, I. *Fundamentals of Electric Propulsion: Ion and Hall Thrusters*, vol. 1 of *JPL Space Science and Technology Book* (John Wiley and Sons Sons, 2008).
- [62] Wolf, M. *Lock-in based detection scheme for a hydrogen beam*. Master's thesis, Vienna University (2013).
- [63] Tawara, H., Itikawa, Y., Nishimura, H. & Yoshino, M. Cross sections and related data for electron collisions with hydrogen molecules and molecular ions. *Journal of Physical and Chemical Reference Data* **19**, 617–636 (1990). URL <http://scitation.aip.org/content/aip/journal/jpcrd/19/3/10.1063/1.555856>.
- [64] MKS instruments. Quadrupole mass spectrometer theory - ion source, mass filter, detector, control unit. URL <http://www.mksinst.com>.
- [65] Pfeiffer Vacuum GmbH. Fundamentals of vacuum technology. URL <https://www.pfeiffer-vacuum.com/en/know-how/>.
- [66] Lotz, W. An empirical formula for the electron-impact ionization cross-section. *Zeitschrift fur Physik* **206**, 205–211 (1967).
- [67] Lotz, W. Electron-impact ionization cross-sections and ionization rate coefficients for atoms and ions from hydrogen to calcium. *Zeitschrift für Physik* **216**, 241–247 (1968). URL <http://dx.doi.org/10.1007/BF01392963>.
- [68] Dr. Sjuts Optotechnik GmbH. Cem - channeltron. URL [www.sjuts.com](http://www.sjuts.com).
- [69] Koch, N. & Steffens, E. High intensity source for cold atomic hydrogen and deuterium beams. *Review of Scientific Instruments* **70**, 1631–1639 (1999). URL <http://scitation.aip.org/content/aip/journal/rsi/70/3/10.1063/1.1149644>.
- [70] Walraven, J. T. M. & Silvera, I. F. Helium-temperature beam source of atomic hydrogen. *Review of Scientific Instruments* **53**, 1167–1181 (1982). URL <http://scitation.aip.org/content/aip/journal/rsi/53/8/10.1063/1.1137152>.
- [71] Thonet, P. A. Use of permanent magnets in multiple projects at CERN. *IEEE Transactions on Applied Superconductivity* **26**, 1–4 (2016).
- [72] Wünschek, B. Technical report for permanent sextupole magnets, unpublished.

## Bibliography

---

- [73] Federmann, S. *A Spin-Flip Cavity for Microwave Spectroscopy of Antihydrogen*. Ph.D. thesis, University of Vienna (2012).
- [74] Federmann, S., Caspers, F., Mahner, E., Juhasz, B. & Widmann, E. Design of a 1.42 GHz Spin-Flip Cavity for Antihydrogen Atoms. *Conf. Proc. C100523*, MOPE054 (2010).
- [75] Juhász, B. & Widmann, E. Planned measurement of the ground-state hyperfine splitting of antihydrogen. *Hyperfine Interactions* **193**, 305–311 (2009). URL <http://dx.doi.org/10.1007/s10751-009-0016-7>.
- [76] Sauerzopf, C. *The ASACUSA Antihydrogen Detector: Development and Data Analysis*. Ph.D. thesis, Technische Universität Wien (2016).
- [77] Sauerzopf, C. Private communication.
- [78] Majorana, E. & Inguscio, M. *Ettore Majorana Scientific Papers: On occasion of the centenary of his birth*, chap. Oriented atoms in a variable magnetic field, 113–136 (Springer Berlin Heidelberg, Berlin, Heidelberg, 2006). URL [http://dx.doi.org/10.1007/978-3-540-48095-2\\_7](http://dx.doi.org/10.1007/978-3-540-48095-2_7).
- [79] Winkler, P. F., Kleppner, D., Myint, T. & Walther, F. G. Magnetic moment of the proton in bohr magnetons. *Phys. Rev. A* **5**, 83–114 (1972). URL <http://link.aps.org/doi/10.1103/PhysRevA.5.83>.
- [80] Jepsen, C. B. Cern summer student work project report: Data taking and simulation-based data analysis at the asacusa experiment. Tech. Rep., CERN (2014).
- [81] Gentile, T. R., Hughey, B. J., Kleppner, D. & Ducas, T. W. Experimental study of one- and two-photon rabi oscillations. *Phys. Rev. A* **40**, 5103–5115 (1989). URL <http://link.aps.org/doi/10.1103/PhysRevA.40.5103>.
- [82] Shore, B. *The Theory of Coherent Atomic Excitation*, vol. 1 Simple Atoms and Fields (Wiley Interscience, 1990).
- [83] Loudon, R. *The Quantum Theory of Light* (Oxford University Press, 2000).
- [84] Nafe, J. E. & Nelson, E. B. The hyperfine structure of hydrogen and deuterium. *Phys. Rev.* **73**, 718–728 (1948). URL <http://link.aps.org/doi/10.1103/PhysRev.73.718>.

- [85] Diermaier, M. *et al.* An atomic hydrogen beam to test asacusa's apparatus for antihydrogen spectroscopy. *Hyperfine Interactions* **233**, 35–40 (2015). URL <http://dx.doi.org/10.1007/s10751-015-1151-y>.
- [86] Drosig, M. *Dealing with Uncertainties* (Springer, 2009), second edn.
- [87] Schlittgen, R. *Einfuerung in die Statistik* (Oldenbourg, 2008), 11. auflage edn.
- [88] Mohr, P. J. & Taylor, B. N. Codata recommended values of the fundamental physical constants: 2002. *Rev. Mod. Phys.* **77**, 1–107 (2005). URL <http://link.aps.org/doi/10.1103/RevModPhys.77.1>.
- [89] Kostelecky, V. A. & Vargas, A. J. Notes on studying lorentz and CPT violation in hydrogen with *asacusa* (2015). Unpublished.

# Curriculum Vitae

## Mag. Martin Diermaier

Leystraße 165/3/20 Wien, 1020  
Tel.: +436604950846  
E: martin.diermaier@gmail.com

**Info** Place of birth: Ried im Innkreis, Upper Austria  
Citizenship: Austrian  
Date of birth: Nov 15<sup>th</sup>, 1984

### Education

#### 2012-2016 PHD THESIS

Stefan Meyer Institute for Subatomic Physics (Austrian Academy of Sciences)

- ⊕ Determination of the Hydrogen Ground-State Hyperfine Splitting in a Beam and Perspectives for Antihydrogen  
(supervisor: Prof. Dr. Eberhard Widmann)

#### 2011-2012 DIPLOMA THESIS

Stefan Meyer Institute for Subatomic Physics

- ⊕ Design and Construction of a Monoatomic Hydrogen Beam  
(supervisor: Privatdoz. Dr. Johann Zmeskal)

#### 2006-2012 DIPLOMA PROGRAMME IN PHYSICS, University of Vienna

#### 2004-2006 DIPLOMA PROGRAMME IN METEOROLOGIE AND GEOPHYSICS, University of Vienna

#### 2003-2004 CIVIL SERVICE, Institut Hartheim, Upper Austria

1999-2003 UPPER HIGH SCHOOL WITH EMPHASIS ON NATURAL SCIENCES,  
Oberstufenrealgymnasium Ried im Innkreis, Upper Austria, Matura

1995-1999 GRAMMER SCHOOL, Gymnasium Schärding, Upper Austria



## Skills

**Languages:** German (native), English, French, Latin

**Software skills:** C++, LabView, Matlab, R, Java, Bash, Latex

**Platforms:** Linux, Mac, Windows, ROOT

**Hardware:** Microwave technologies, detector development, data acquisition, signal processing, plasma technologies, vacuum technologies, mass spectrometry, superconducting magnet technologies, beam technologies, radioactive materials, cryogenics

**Project management:** Technical design, purchasing, construction, and, analysis within the PhD project

## Conferences

**2016 LEAP Conference** – Kanazawa, Japan, Invited talk

**2015 ÖPG/SPS Jahrestagung** – Vienna, Austria, Talk

**2014 EXA Conference** – Vienna, Austria, Invited Talk

**2014 FLAIR Workshop** – Heidelberg, Germany, Poster presentation

**2013 ÖPG Jahrestagung** – Pöllau, Austria, Talk

**2013 LEAP Conference** – Uppsala, Sweden, Poster presentation

**2012 ÖPG/SPS Jahrestagung** – Linz, Austria, Poster presentation

## Scientific papers

N. Kuroda, S. Ulmer, D. J. Murtagh, S. Van Gorp, Y. Nagata, M. Diermaier, S. Federmann, M. Leali, C. Malbrunot, V. Mascagna, O. Massiczek, K. Michishio, T. Mizutani, A. Mohri, H. Nagahama, M. Ohtsuka, B. Radics, S. Sakurai, C. Sauerzopf, K. Suzuki, M. Tajima, H. A. Torii, L. Venturelli, B. Wünschek, J. Zmeskal, N. Zurlo, H. Higaki, Y. Kanai, E. Lodi Rizzini, Y. Nagashima, Y. Matsuda, E. Widmann, Y. Yamazaki  
*The ASACUSA CUSP: an antihydrogen experiment*  
**Hyperfine Interactions** 11/2015  
DOI: 10.1007/s10751-015-1205-1

Y Nagata, C Sauerzopf, A Capon, N Kuroda, Y Abo, M Diermaier, P Dupre, Y Higashi, S Ishikawa, C Kaga, M Leali, C Malbrunot, V Mascagna, D Murtagh, B Radics, M C Simon, M Tajima, H A Torii, S Van Gorp, J Zmeskal, H Breuker, H Higaki, Y Kanai, Y Matsuda, S Ulmer, L Venturelli, E Widmann, Y Yamazaki

*The development of the antihydrogen beam detector and the detection of the antihydrogen atoms for in-flight hyperfine spectroscopy*

**Journal of Physics Conference Series** 09/2015; 635(2):022061  
DOI: 10.1088/1742-6596/635/2/022061

D. Grzonka, K. Kilian, J. Ritman, T. Sefzick, W. Oelert, M. Diermaier, E. Widmann, J. Zmeskal, B. Glowacz, P. Moskal, M. Zielinski, M. Wolke, P. Nadel-Turonski, M. Carmignotto, T. Horn, H. Mkrtchyan, A. Asaturyan, A. Mkrtchyan, V. Tadevosyan, S. Zhamkochyan, S. Malbrunot-Ettenauer, W. Eyrich, F. Hauenstein, A. Zink  
*Search for Polarization Effects in the Antiproton Production Process*  
**Acta Physica Polonica Series B** 01/2015; 46(1)  
DOI: 10.5506/APhysPolB.46.191



Martin Diermaier, Peter Caradonna, Bernadette Kolbinger, Chloe Malbrunot, Oswald Massiczek, Clemens Sauerzopf, Martin C. Simon, Michael Wolf, Johann Zmeskal, Eberhard Widmann  
*An atomic hydrogen beam to test ASACUSA's apparatus for antihydrogen spectroscopy*  
**Hyperfine Interactions** 01/2015; 233(1)  
DOI: 10.1007/s10751-015-1151-y

B. Kolbinger, A. Capon, M. Diermaier, S. Lehner, C. Malbrunot, O. Massiczek, C. Sauerzopf, M. C. Simon, E. Widmann:  
*Numerical Simulations of Hyperfine Transitions of Antihydrogen*  
**Hyperfine Interactions** 01/2015; 233(1)  
DOI: 10.1007/s10751-015-1130-3

N. Kuroda, S. Ulmer, D. J. Murtagh, S. Van Gorp, Y. Nagata, M. Diermaier, S. Federmann, M. Leali, C. Malbrunot, V. Mascagna, O. Massiczek, K. Michishio, T. Mizutani, A. Mohri, H. Nagahama, M. Ohtsuka, B. Radics, S. Sakurai, C. Sauerzopf, K. Suzuki, M. Tajima, H. A. Torii, L. Venturelli, B. Wünschek, J. Zmeskal, N. Zurlo, H. Higaki, Y. Kanai, E. Lodi-Rizzini, Y. Nagashima, Y. Matsuda, E. Widmann, Y. Yamazaki  
*Towards a spin polarized antihydrogen beam*  
**Hyperfine Interactions** 10/2014; 228(1-3):67-76  
DOI:10.1007/s10751-014-1016-9

C. Malbrunot, P. Caradonna, M. Diermaier, N. Dilaver, S. Friedreich, B. Kolbinger, S. Lehner, R. Lundmark, O. Massiczek, B. Radics, C. Sauerzopf, M. Simon, E. Widmann, M. Wolf, B. Wünschek, J. Zmeskal  
*Spectroscopy Apparatus for the Measurement of The Hyperfine Structure of Antihydrogen*  
**Hyperfine Interactions** 02/2014; 228(1-3)  
DOI:10.1007/s10751-014-1013-z

N Kuroda, S Ulmer, D J Murtagh, S Van Gorp, Y Nagata, M Diermaier, S Federmann, M Leali, C Malbrunot, V Mascagna, O Massiczek, K Michishio, T Mizutani, A Mohri, H Nagahama, M Ohtsuka, B Radics, S Sakurai, C Sauerzopf, K Suzuki, M Tajima, H A Torii, L Venturelli, B Wünschek, J Zmeskal, N Zurlo, H Higaki, Y Kanai, E Lodi Rizzini, Y Nagashima, Y Matsuda, E Widmann, Y Yamazaki  
*A source of antihydrogen for in-flight hyperfine spectroscopy*  
**Nature Communications** 01/2014; 5:3089  
DOI:10.1038/ncomms4089

E. Widmann, M. Diermaier, B. Juhasz, C. Malbrunot, O. Massiczek, C. Sauerzopf, K. Suzuki, B. Wünschek, J. Zmeskal, S. Federmann, N. Kuroda, S. Ulmer, Y. Yamazaki  
*Measurement of the hyperfine structure of antihydrogen in a beam*  
**Hyperfine Interactions** 01/2013  
DOI: 10.1007/s10751-013-0809-6